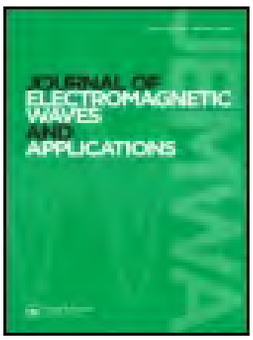

Journal of Electromagnetic Waves and Applications

ISSN: 0920-5071 (Print) 1569-3937 (Online) Journal homepage: https://www.tandfonline.com/loi/tewa20

A review of the recent advances in dielectric resonator antennas

Biswajeet Mukherjee, Pragati Patel & Jayanta Mukherjee

To cite this article: Biswajeet Mukherjee, Pragati Patel & Jayanta Mukherjee (2020): A review of the recent advances in dielectric resonator antennas, Journal of Electromagnetic Waves and Applications, DOI: 10.1080/09205071.2020.1744484

To link to this article: https://doi.org/10.1080/09205071.2020.1744484

Published online: 08 Apr 2020.

JOURNAL OF ELECTROMAGNETIC WAVES AND APPLICATIONS
https://doi.org/10.1080/09205071.2020.1744484

Taylor & Francis
Taylor & Francis Group

INVITED REVIEW ARTICLE

A review of the recent advances in dielectric resonator antennas

Biswajeet Mukherjee[a], Pragati Patel[b] and Jayanta Mukherjee[c]

[a]Department of Electronics & Communication Engineering, IIITDM, Jabalpur, India; [b]Department of Electronics & Communication Engineering, NIT, Goa, India; [c]Department of Electrical Engineering, IIT Bombay, India

ABSTRACT

This paper presents a comprehensive review of the state of art techniques and geometries which have been explored in the areas of Dielectric Resonator Antennas (DRA). With the evolution of first rectangular geometry to the current investigations, the basic aims of research in this field of electrical size miniaturization, retrofitting bandwidth as per commercial needs and radiation pattern stability by controlling the modes in the DRA still persist. Various techniques to miniaturize the physical and electrical size, mode excitation through varied mechanisms like probe, microstrip, slot, etc., improving bandwidth and radiation characteristics by various researchers have been included. The novel geometries and concept of fractals as introduced to the DRAs have also been addressed in this paper.

ARTICLE HISTORY
Received 5 November 2019
Accepted 4 March 2020

KEYWORDS
Bandwidth; dielectric resonator antennas; gain; modes; probe; radiation pattern

1. Introduction

The need for faster communication and high data rates has escalated the frequency of operation in the domain of wireless communication. In surge to meet the everlasting demands, the antenna system has evolved from wired structures to planar nature. The evolution of the microstrip patch antennas led to miniaturization of the circuits which helped evolve various novel devices, though so, at extreme high frequencies, the conductor losses increase thus, making them inefficient to be used.

The Dielectric Resonator Antennas (DRAs) evolved with a repeated effort of Prof. S A Long, et al. in the 1980s. The first investigation was done on rectangular geometry and it was established as an efficient radiator. DRAs offered promising features like low loss, high efficiency and wide impedance bandwidth [1–3]. This led to the genesis of various research activities in the field of DRAs. The reason for wide impedance bandwidth is the low-quality factor of the antenna which increases the radiations which is attributed to the sudden change of the permittivity at the dielectric air interface.

Many other techniques and geometries have been investigated so as to propose compact and electrically small radiators. Since the radiation mechanism is not due to the conducting elements and the lack of conductors in the DRAs, lead to high efficiency

CONTACT Biswajeet Mukherjee biswajeet.26@gmail.com Department of Electronics & Communication Engineering, IIITDM, Jabalpur-482005, India

at higher frequencies. Investigations on re-configurability with microstrip patch using various switches like PIN diodes, etc. also reveal its capability of integration with other active/passive circuit components on the same chip itself. It is also of interest to note that the wide impedance bandwidth of a DRA can be achieved using finite and full ground plane, unlike printed monopoles with partial ground planes.

Integration of patch with DRAs has also demonstrated its tuning capabilities for various frequencies of operation. The application of DRAs has also been explored for MIMO systems and various diversity techniques. This has been discussed in details in later subsections from references [4–48]. The MIMO systems are based on use of multiple antennas at the transmitter and receiver side. This improves the channel capacity and solves fading problem. The applications such as 5G communication prefers higher data rate without increasing power level. The challenge lies in reducing the overall size of MIMO system while maintaining good isolation between different antenna elements forming MIMO system. The techniques available for improvement of isolation by reducing mutual coupling between MIMO antenna systems are; orthogonal feed networks, defected ground structures, electromagnetic bandgap structures, decoupling networks, neutralizing lines, and etched parasitic elements [27].

Further, a prospect of using DRAs for arrays towards beam forming and phased array is under active investigation. DRA arrays with Rectangular DRA as the basic element have shown competitive results in this field.

Further, Techniques are investigated to achieve wide bandwidth, compact design, and circular polarization on rectangular DRAs based on perforations, air gap, fractal, edge grounding, etc. Improvement in the bandwidth is achieved by lowering of quality factor and merging of resonant modes. The ability to excite orthogonal field components within the DRAs has resulted in tuning Linear and Circular Polarization in the DRAs using slots and various geometries.

A fundamental understanding of the DRA is to identify the various resonant modes. There are two types of modes in a DRA namely confined and non-confined modes. The resonant modes help identify the possible radiation mechanism and the farfield radiation pattern. However, the nomenclature of the near fields for Electric and Magnetic Field are dependent on the co-ordinates axis under consideration. The review article encompasses a comprehensive study of all the details pertaining to the latest trends in research of the DRAs. A review on the DRAs was done in [3], however, the current article associates the references of the past and correlates with the current & future trends of research in DRAs.

2. Electromagnetic modes in a DRA: basic geometries

Being three-dimensional structures, the DRAs offer various resonant modes which can be tuned for various applications. The resonant modes satisfy two important conditions as given in the equations below:

$$\overrightarrow{E} \cdot \hat{n} = 0 \tag{1}$$

$$\hat{n} \times \vec{H} = 0 \tag{2}$$

where $\hat{n}$ is the normal to surface of the resonator, $\vec{H}$ is the magnetic field intensity and $\vec{E}$ is the electric field intensity. The modes which satisfy the conditions (1) and (2) are called *confined*

mode, whereas those which satisfy only (1) are called *non-confined modes* [49]. It has been shown by Van Bladel in [50] that *confined modes* can be satisfied by only the geometries which support the body of revolution, i.e. Cylindrical and Hemispherical geometries, whereas the *non-confined* modes are satisfied by only rectangular geometries.

2.1. Modes in rectangular DRA (RDRA)

The mode nomenclature in rectangular DRA is stated as TE_{mnp} and TM_{mnp}, where *m, n, p* represent the half-cycle sinusoidal variations of the transverse field component under consideration along the *x, y, z* axes respectively of the rectilinear coordinate system. In [51], the *H modes* are referred as *TM modes* and *E modes* are referred to as *TE modes.* It has been observed that TM_{mnp} modes don't satisfy Equation (1) on using the Dielectric Waveguide model (DWM) after applying the magnetic wall condition and so the *TM* modes have not been observed. By using the DWM and presuming *z* to be the direction of propagation, the fields in RDRA [2,52,53] are as follows:

$$H_x = \frac{(k_x k_z)}{j\omega\mu_o}\begin{Bmatrix} sin(k_x x)\cos(k_y y) \\ cos(k_x x)\cos(k_y y) \end{Bmatrix} \sin(k_z z) \tag{3}$$

$$H_y = \frac{(k_y k_z)}{j\omega\mu_o}\begin{Bmatrix} cos(k_x x)\sin(k_y y) \\ sin(k_x x)\sin(k_y y) \end{Bmatrix} \sin(k_z z) \tag{4}$$

$$H_z = \frac{(k_x^2 + k_y^2)}{j\omega\mu_o}\begin{Bmatrix} cos(k_x x)\cos(k_y y) \\ sin(k_x x)\cos(k_y y) \end{Bmatrix} \cos(k_z z) \tag{5}$$

$$E_x = k_y\begin{Bmatrix} cos(k_x x)\sin(k_y y) \\ sin(k_x x)\sin(k_y y) \end{Bmatrix} \cos(k_z z) \tag{6}$$

$$E_y = -k_x\begin{Bmatrix} sin(k_x x)\cos(k_y y) \\ cos(k_x x)\cos(k_y y) \end{Bmatrix} \cos(k_z z) \tag{7}$$

$$E_z = 0 \tag{8}$$

While *l, w, d* are the length, width and depth of the RDRA (dimensions), *c* is the velocity of light in free space and the wave numbers are defined as follows:

$$k_z \tan\left(\frac{k_x d}{2}\right) = \sqrt{(\varepsilon_0 - 1)k_{mn}^2 - k_z^2} \tag{9}$$

$$k_{mn} = \frac{2\pi f_m}{c}, k_x = m\frac{\pi}{w}, k_y = n\frac{\pi}{d}, \tag{10}$$

$$k_c^2 = k_x^2 + k_y^2 = \varepsilon_0 k_{mn}^2 - k_z^2 \tag{11}$$

From equations (3) to (8), upper functions in the bracket are chosen when *m* and *n* are both odd whereas the lower functions are chosen when *m* is even and *n* is odd. The modes in RDRA are often represented by $TE^z_{mn\delta}$. Here δ instead of *p* shows that the while direction of propagation is *z*, the half cycle of sinusoidal rotation is incomplete along the *z*-axis. The RDRA offers two degrees of freedom where the antenna engineer can alter the ratio of *w/l*

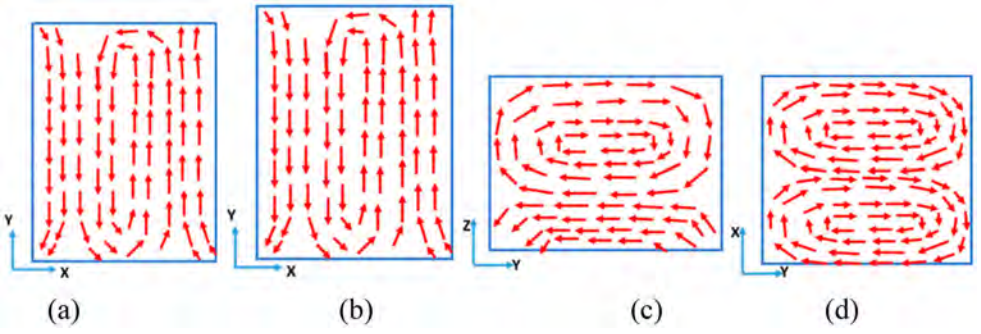

Figure 1. The TE modes of the RDRA using H field variations. (a) x-y plot for TE^{x}_{121} mode. (b) x-y plot for TE^{y}_{211} mode. Both the plots are taken from [53]. (c) y-z plot for TE^{x}_{212} mode. (d) x-y plot for TE^{x}_{212} mode.

and *w/d*. The H field orientation for various TE modes is as shown below in Figure 1. The TE^{x}_{121} plot is shown in Figure 1(a), TE^{y}_{211} plot is shown in Figure 1(b), whereas TE^{x}_{212} plots are shown in Figure 1(c) and (d) respectively. These are referred from [53].

2.2. Modes in cylindrical DRA (CDRA)

The modes of a CDRA are classified in three groups namely TE_{mnp}, TM_{mnp} and HEM_{mnp}, where *m, n, p* represent the half-cycle sinusoidal variation along the azimuth (Φ), radial (*r*) and axial (*z*) axes respectively. In some cases the *p* is represented by δ, to signify an incomplete half-cycle sinusoidal rotation along the axial axis, if *z* is the direction of propagation. It is interesting to observe that the *TE* and *TM* modes are axially symmetric, i.e. the variation is independent of the azimuth plane whereas the *HEM* modes show dependence along the azimuth plane [1–3].

The *HEM* mode is called *HE* mode if E_z is dominant or *EH* if H_z is dominant based on the reference [2]. The first set of dominant modes in the CDRA is classified as $TM_{01\delta}$, $TE_{01\delta}$ and $HE_{11\delta}$. For an isolated CDRA, the dominant mode resonant frequencies can be arranged as $TE_{01\delta} < TM_{01\delta} < HE_{11\delta}$.

The *TM* mode can be excited in CDRA whenever the direction of excitation current coincides with the axis of the CDRA. This can be easily achieved by a probe fed at the center of the CDRA. This leads to a radiation pattern that resembles a short electric monopole. Similarly, if the probe is at an offset from the center of an isolated CDRA or displaced from the axis of the cylinder, the $HE_{11\delta}$ dominant mode can be excited which radiates like a short horizontal magnetic dipole.

In case the configuration of the CDRA has an axis parallel to the ground plane example, a half-split CDRA, a slot feed may excite the $TE_{01\delta}$ mode which radiates like a short magnetic monopole. This has been discussed in details in [1–3].

The various excitation strategies are utilized to suitably excite the different modes of the CDRA for various applications. The CDRA offers one degree of freedom to an antenna engineer to facilitate the variation in radius to height *r/h* ratio, for achieving a suitable resonant frequency and bandwidth of operation.

The approximate fields for a $TE_{01\delta}$ mode of CDRA is estimated as follows [2,54–56]:

$$H_Z \propto J_0(\beta r)\cos\left(\frac{\pi z}{2h}\right) \tag{12}$$

$$H_r \propto J_1(\beta r)\sin\left(\frac{\pi z}{2h}\right) \tag{13}$$

$$E_\phi \propto J_1(\beta r)\cos\left(\frac{\pi z}{2h}\right) \tag{14}$$

$$E_Z = E_r = H_\phi = 0 \tag{15}$$

where $J_0(\beta r)$ and $J_1(\beta r)$ are the zeroth and first-order Bessel's functions of the first kind respectively. β is the solution to $J_0(\beta a) = 0$ with a as the radius of the CDRA. The $TM_{01\delta}$ are similar to Equations (12)–(15) with magnetic and electric filed components interchanged.

On a similar note the field components of $HE_{11\delta}$ mode of CDRA are estimated as follows [2,54–56]:

$$E_Z \propto J_1(\alpha r)\cos\left(\frac{\pi z}{2h}\right)\begin{Bmatrix} cos\phi \\ sin\phi \end{Bmatrix} \tag{16}$$

$$E_r \propto \frac{\partial J_1(\alpha r)}{\partial(\alpha r)}\sin\left(\frac{\pi z}{2h}\right)\begin{Bmatrix} cos\phi \\ sin\phi \end{Bmatrix} \tag{17}$$

$$E_\phi \propto J_1(\alpha r)\sin\left(\frac{\pi z}{2h}\right)\begin{Bmatrix} sin\phi \\ cos\phi \end{Bmatrix} \tag{18}$$

$$H_r \propto J_1(\alpha r)\cos\left(\frac{\pi z}{2h}\right)\begin{Bmatrix} sin\phi \\ cos\phi \end{Bmatrix} \tag{19}$$

$$H_\phi \propto \frac{\partial J_1(\alpha r)}{\partial(\alpha r)}\cos\left(\frac{\pi z}{2h}\right)\begin{Bmatrix} cos\phi \\ sin\phi \end{Bmatrix} \tag{20}$$

$$H_Z \approx 0 \tag{21}$$

where α is the solution to $J_1(\alpha a) = 0$, a is the radius of the CDRA. The choice of $cos\phi$ and $sin\phi$ depends on the location of the feed. The various E field orientations for TE modes in a CDRA and sectored CDRA are as shown below in Figure 2. Figure 2(a) and (b) depict the field plots for $TE_{011+\delta}$ mode, whereas Figure 2(c) and (d) depict the plots for $TE_{01\delta}$ mode for sectored CDRA. Both are referred from [57]. Similarly, the various E field orientations for TM modes in a CDRA are as shown below in Figure 3. Figure 3(a) and (b) represent the $TM_{01\delta}$ mode, Figure 3(c) and (d) represent the $TM_{11\delta}$ mode and Figure 3(e) and (f) represent the $TM_{21\delta}$ mode respectively as referred from [58]. Further, the various E field orientations for HE modes in a CDRA are as shown in Figure 4. Figure 4(a) and (b) shows the plot for $HE_{11\delta}$ mode, Figure 4(c) and (d) shows the plot for $HE_{12\delta}$ mode and Figure 4(e) shows the plot for $HEM_{21\delta}$ mode as referred from [59,60].

2.3. Modes in hemispherical DRA (HDRA)

The hemispherical geometry supports both the conditions of *confined modes*. The modes in HDRA can be classified as TE_{mnp} and TM_{mnp}, where *m, n, p* represent the field variations along the radial (r), azimuth (Φ) and the elevation (θ) directions respectively. Since the dielectric air interface for an HDRA is simpler and has a smoother transition, a closed form expression in terms of Green's function synthesis is possible.

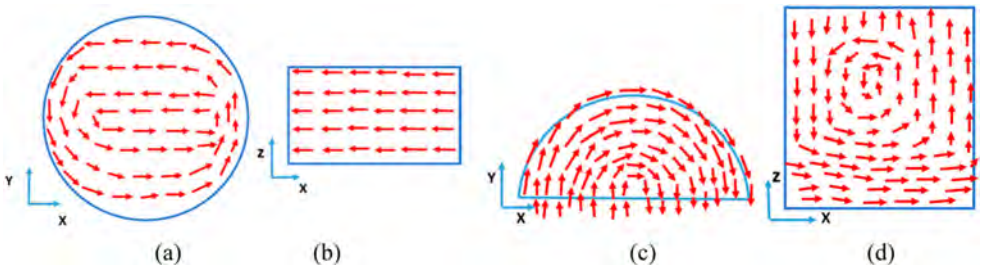

Figure 2. The TE modes observed in a CDRA. (a) x-y plot for $TE_{011+\delta}$ mode. (b) x-z plot for the $TE_{011+\delta}$ mode. Both are taken from [58]. (c) x-y plot for $TE_{01\delta}$ plot for sectored CDRA. (d) x-z plot for the $TE_{01\delta}$ plot for sectored CDRA. Both are taken from [57].

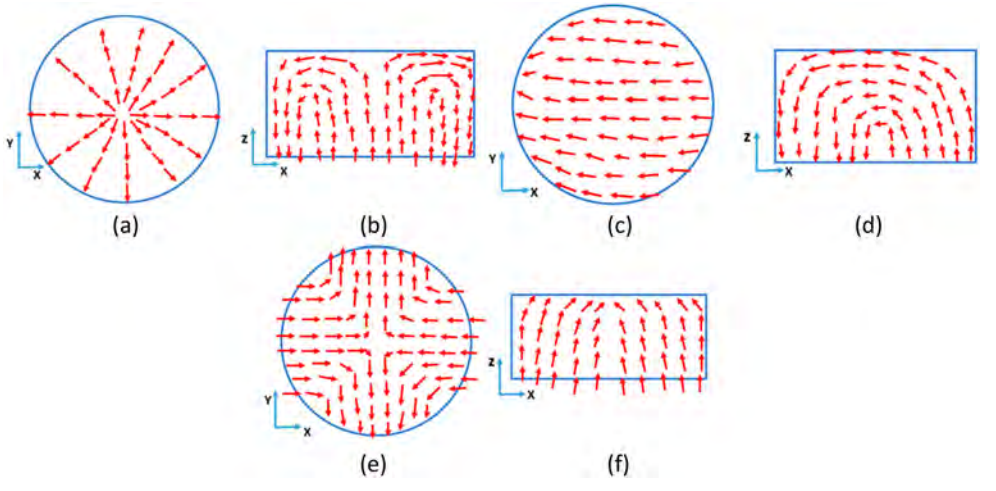

Figure 3. The TM modes observed in a CDRA. (a) x-y plot for $TM_{01\delta}$ mode. (b) x-z plot for $TM_{01\delta}$ mode. (c) x-y plot for $TM_{11\delta}$ mode. (d) x-z plot for $TM_{11\delta}$mode. (e) x-y plot for $TM_{21\delta}$ mode. (f) x-z plot for $TM_{21\delta}$ mode. All modes are taken from reference [58].

The Green's function synthesis for an HDRA is divided as follows:

$$G_{TM/TE}^{Ar/Fr} = G_P + G_H \tag{22}$$

where *Ar* is the electric potential corresponding to the generation of *TM* modes, F_r is the magnetic potential corresponding to the generation of *TE* modes, G_p is the particular solution which represents the source radiating in an unbounded dielectric medium and G_H is the homogeneous solution which encapsulates the dielectric boundary discontinuities at the dielectric/air interface. This is strictly in conjecture to the notations employed by K. M. Luk in [1] and Ghosh et al. in [61–63].

Each potential function is denoted by an infinite series of modal functions and the modal coefficients are then obtained by matching boundary conditions at source point and on DRA surface [1,61–63]. This means that if an HDRA is excited by a probe feed which gives a $\hat{z}$ directed current, then the particular solution, G_P, involves solving the probe (conductor) and dielectric boundary condition where the dielectric is considered as an unbounded medium and the homogeneous solution, G_H, is the solution to boundary condition over

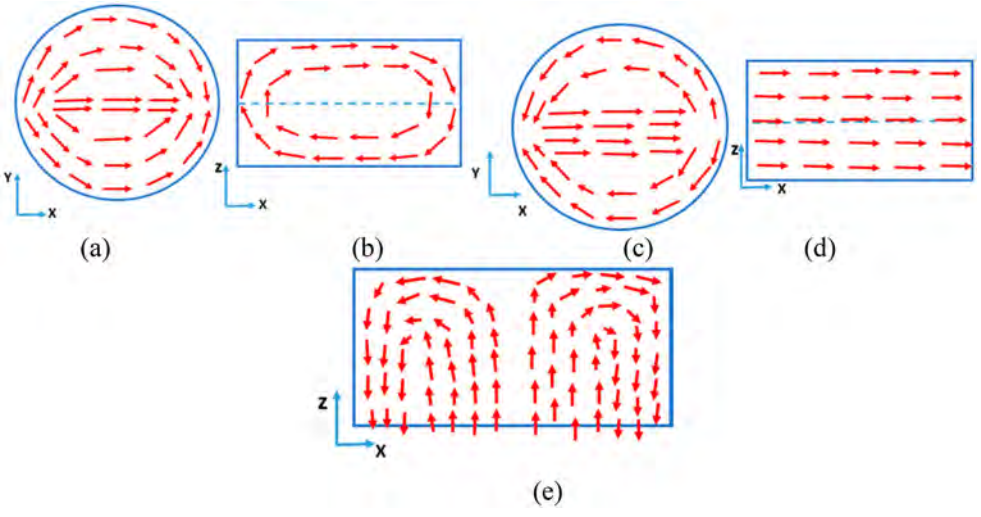

Figure 4. The HEM (Hybrid EM modes) of the CDRA. (a) x-y plot for $HE_{11\delta}$mode. (b) x-z plot for $HE_{11\delta}$ mode. (c) x-y plot for $HE_{12\delta}$ mode. (d) x-z plot for the $HE_{12\delta}$ mode. All are taken from [59]. (e) x-z plot for $HEM_{21\delta}$ mode as referred from [60].

the dielectric-air interface. Image theory is adopted to find the equivalent currents and thus calculate the Green's function.

If $\vec{r}(r,\theta,\emptyset)$ and $\overrightarrow{r'}(r,\theta,\emptyset)$ represent the field and source points respectively, then the equivalent Green's function for lowest order *TE* mode, i.e. TE_{111} mode is given by the following equations (r < a):

$$G_{TE_{111}} = \frac{-3k}{8\pi\omega\varepsilon rr'} sin\theta sin\theta' \cos(\emptyset - \emptyset')[\emptyset(kr')\Psi(kr) + \alpha_{TE}\widehat{J_1}(kr')\widehat{J_1}(kr)] \tag{23}$$

$$\text{Where } \phi(kr) = \begin{cases} \widehat{J_1}(kr'), r > r' \\ \widehat{H_1^{(2)}}, r < r' \end{cases} \tag{24}$$

$$\Psi(kr) = \begin{cases} \widehat{H_1^{(2)}}, r > r' \\ \widehat{J_1}(kr'), r < r' \end{cases} \tag{25}$$

$$\alpha_{TE} = \frac{-1}{\Delta_{TE}}\left[\widehat{H_1^{(2)}}(ka)\widehat{H_1^{(2)'}}(k_0a) - \sqrt{\varepsilon_r}\widehat{H_1^{(2)'}}(ka)\widehat{H_1^{(2)}}(k_0a)\right] \tag{26}$$

$$\Delta_{TE} = \widehat{J_1}(ka)\widehat{H_1^{(2)'}}(k_0a) - \sqrt{\varepsilon_r}\widehat{J_1}'(ka)\widehat{H_1^{(2)}}(k_0a) \tag{27}$$

In the above equations, $k_0 = \omega\sqrt{\mu_0\varepsilon_0}, k = \sqrt{\varepsilon_r}k_0, \widehat{J_1}(x)$ is the first order spherical Bessel's function of the first kind and $\widehat{H_1^{(2)}}(x)$ is the spherical Hankel function of the second kind. The Electric field E_z due to the probe current J_z can be estimated by the following equations:

$$E_z(\vec{r}) = \iint G_{TE_{111}}(\vec{r}, \overrightarrow{r'})J_Z(z')dS' \tag{28}$$

$$J_Z(z') = J_0 sink(l - |z'|), \quad -l \le z \le l \tag{29}$$

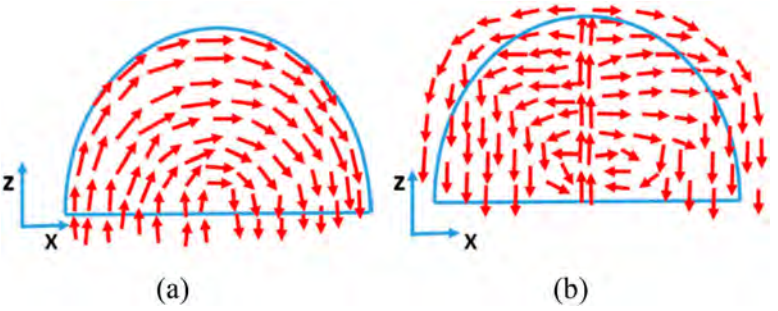

Figure 5. The EM modes observed in HDRA. (a) x-z plot for TE $_{111}$ mode as referred from [65]. (b) x-z plot for the TM_{101} mode as referred from [66].

Equation (28) is calculated for surface current flowing on the imaged probe surface of S_0. a is the radius of the hemisphere under consideration.

Referring to the input plots of the HDRA excited by a probe shows that as the probe is displaced from the center of the circular base of the HDRA, input impedance of HDRA increases. This is accounted to the reason that at the center the probe current is *r-directed* and so it excites *TM* modes whereas when displaced the probe excites the fundamental TE_{111} mode [1,64].

For a generalized solution for *TM* mode excited by probe feed, the G_p and G_H in Equation (22), are given as follows [2]:

$$G_P(z,z') = \frac{-j}{\omega\varepsilon}\left(\frac{\partial^2}{\partial z^2} + k^2\right)\frac{e^{-jkR}}{4\pi R} \tag{30}$$

$$G_H(z,z') = \frac{-1}{4\pi\omega\varepsilon kz'z^2}\sum_{n=1}^{\infty} n(n+1)(2n+1)\alpha_n^{TM}\widehat{J_n}(kz')\widehat{J_n}(kz) \tag{31}$$

$$\alpha_n^{TM} = \frac{-\left[\widehat{H_n^{(2)'}}(ka)\widehat{H_n^{(2)}}(k_0a) - \sqrt{\varepsilon_r}\widehat{H_n^{(2)}}(ka)\widehat{H_1^{(2)'}}(k_0a)\right]}{\widehat{J_n'}(ka)\widehat{H_n^{(2)}}(k_0a) - \sqrt{\varepsilon_r}\widehat{J_n}(ka)\widehat{H_n^{(2)'}}(k_0a)} \tag{32}$$

where α_n^{TM} is the *TM*-mode reflection coefficient at the DRA boundary and $R = \sqrt{r_1^2 + (z-z')^2}$. The Electric field can be calculated by substituting the total Green's function as suggested in Equation (28) for obtaining the fields for the *TM* modes.

The TE_{111} mode is the lowest order and hence the dominant mode of the HDRA. This mode radiates like a short magnetic dipole. Though the radiation pattern has a broadside nature, but the beamwidth is low. Contrary, the TM_{101} mode radiates like a short electric monopole antenna and has a null along the broadside direction of the radiation pattern.

The HDRA offers zero degree of freedom and so for a fixed frequency, the radius of the hemisphere is also fixed which cannot be altered. The various E field orientations for TE & TM modes in an HDRA are as shown in Figure 5(a) for TE_{111} mode [65] and Figure 5(b) for TM_{101} mode [66] respectively.

2.4. Feeding techniques in a DRA

Feeding techniques play an important role in exciting the suitable mode in a DRA. The DRAs can be excited by various methods as stated below:

1. Probe feed – The most commonly used feeding method is the coaxial feeding due to its simplicity of extending the central conductor as probe inside or at a suitable location around the DRA [67]. This feeding method has been exploited to achieve broadband operation for the DRAs. However, the major drawback of this method is to locate the specific position where sometimes a hole needs to be drilled inside the dielectric material. This precise drilling may be subjected to human/parallax error. Though so, this method offers high radiation efficiency due to maximum coupling between probe fed inside the DRA. However, probe feed has also been used in the mode matching technique where a precise mode needs to be excited within the DRA. For example, as stated before, an offset probe feed excites the TE mode in the HDRA whereas a center probe feed excites TM mode in the HDRA. The impedance bandwidth in a probe feed is affected by the position and the length of the probe.
2. Microstrip feed – For practical circuits which are MIC/MMIC based and fabricated on PCBs, microstrip feed is an efficient method for exciting the DRA. The length of the microstrip can be extended over the surface of the DRA to achieve conformal feeding. This method of conformal feed has also been used for generating orthogonal modes leading to Circular Polarization. Also, the conformal strip integrated with a patch can lead to efficient coupling with the DRA and suitably excite the desired modes. The conformal strip can be easily placed by using copper tapes. However, the length of the microstrip line effects the phase and so for efficient coupling in terms of phase, the length needs to be prefixed. Since microstrip lines are band-limited resonators, for achieving wideband, impedance transformers can be used. Also, it can be used for exciting linear arrays and when integrated with phase shifters, can be used for phased array antenna applications also. While placing the DRA on a microstrip line, a small undesired air gap is introduced which reduces the effective permittivity of the DRA material.
3. Co-planar Waveguide (CPW) feed – The CPW feed has been used for both narrowband and broadband applications. CPW feed can be modeled as both inductive slot and capacitive slot, as shown in Figure 6(a) and (b) respectively, [68] for a circular loop feed to a DRA. This is a popular choice for application in millimeter waves for system on chip as the ground plane isolates the DRA and lossy silicon substrate. This leads to improved efficiency.
4. Aperture Coupled feed – Slot feed or aperture coupled feed can be used for maximizing the excitation of a pure mode in the DRA. The aperture feed suppresses the interaction of any spurious EM wave of the feed line or probes to the DRA. The slot length is generally of $\lambda/2$ length. Asymmetric cross-slot configuration has been used for generating orthogonal modes in the DRA achieving circular polarization as well. Aperture feeds are relatively easy to integrate with the DRA on the same substrate.
5. Other feeding techniques – The Dielectric Image Guide (DIG) has been used to successfully excite the Dolph-Chebyschev distribution in a linear DRA array [69]. A very high gain and extremely low cross-polarization levels are observed. Further, waveguide

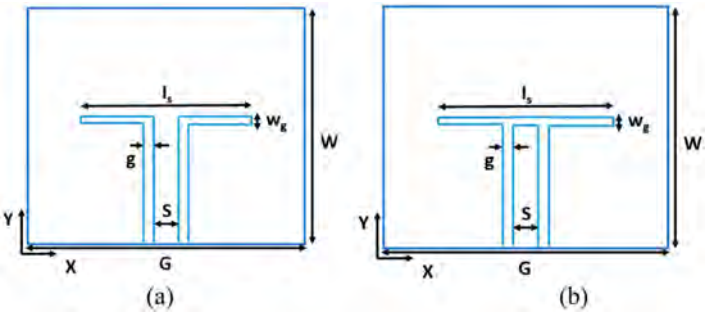

Figure 6. The various CPW feed techniques. (a) Inductive slot of CPW. (b) Capacitive Slot of CPW.

feed for high power applications has also been used. The figures of these various feeding techniques and the various features have been discussed in the next sections along with an articulation in the tables of comparison.

3. Review of the RDRA geometry

This section shall provide a detailed review of the RDRA and its modified geometries. This section has been divided into the subsections namely wideband RDRA, Low profile and compact RDRAs, Circularly Polarized RDRAs, RDRAs array and MIMO & Diversity RDRAs.

3.1. Wideband RDRAs

The emerging wireless applications require wideband or broadband antennas to achieve high data rate and multitasking. However, limited bandwidth is achieved from single antenna because of their resonant nature. Therefore, several techniques are proposed for bandwidth enhancement of DRAs. The bandwidth enhancement techniques of microstrip antennas are suitable for DRAs as well because both act as cavity resonators. The conventional RDRAs with dielectric constant, $\varepsilon_r \sim 10$ offer 10-dB impedance bandwidth of $\sim 10\%$ but bandwidth enhancement methods can improve bandwidth up to 120% or more. These methods are mainly based on; lowering of quality factor, external matching network, and stacking of two or more dielectric resonators [1].

Numerous RDRAs based on lowering of quality factor are achieved by reduction of dielectric constant because of inverse relationship. It improves bandwidth significantly but lowered dielectric constant results in increase of resonant frequency. This is undesired for applications where low profile or compact RDRAs are required particularly at lower resonant frequencies. Nevertheless RDRAs based on aforementioned methods are investigated for bandwidth enhancement.

The proposed RDRAs based on the technique of perforations are discussed first. In [66], an array of RDRA is designed based on perforations. Interestingly, the array is designed from a single sheet of dielectric material to avoid placement of single radiator individually. Therefore, it provides ease of fabrication. The gain is controlled through two perforation parameters, size of holes, and distance between two consecutive holes. The effective dielectric constant of the perforated dielectric sheet can be calculated based on the volume

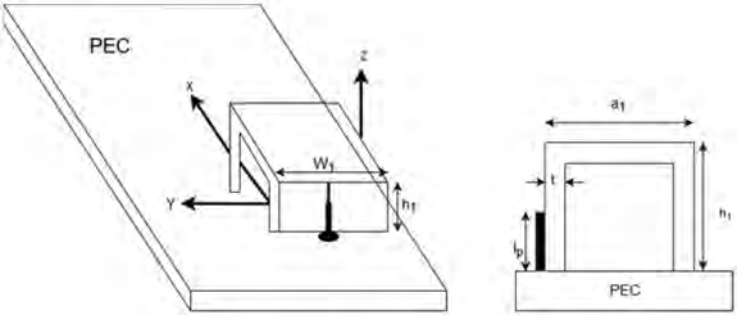

Figure 7. Dual-mode bridge-shaped dielectric resonator antennas [72].

average method. Another configuration where an array of size 8×8 is designed at 25 GHz and compared with microstrip counterpart [70]. Both the arrays are designed using the same corporate feed network. The DRA array offered high gain and wider bandwidth.

In [71], air gap is provided between dielectric resonator and ground plane in the compact edge grounded RDRA. Subsequently, bandwidth improves upto 34% in comparison to other narrowband edge grounded RDRAs. Next, bridge shaped DRA is derived from RDRA [72] and shown in Figure 7. The fundamental TE_{111} mode is preserved with dual-mode impedance responses at 3.5 and 5.5 GHz offering bandwidth of 9.6% and 8.2% respectively. The idea is to use empty space in the bridge shaped DRA for placement of other radiators or RF front end components.

Stacking of two or more dielectric resonators is another technique for enhancement of bandwidth. Each dielectric resonator has a different resonant frequency which merges in the bandwidth of operation and results in improvement of bandwidth. The drawback is increased real state and bulky structure. Therefore, this method is not suitable for designing array of RDRAs. In [73,74], design guidelines for stacking of two or more dielectric resonators are established. The effective dielectric constant is calculated with simple static capacitance model. Different resonators behave like impedance transformer and match DRA impedance with the feed. Therefore bandwidth can be enhanced up to 20% by stacking two or more dielectric resonators at resonant frequency of 14.7 GHz. In [75], analytical solution is derived to find the optimum value of lower dielectric insert which improves bandwidth up to 30%, the design is as shown in Figure 8. A similar concept has been explored in [76] where instead of stacking; two elements placed along each other are excited by conformal strip for UWB applications.

Another method to improve bandwidth is by merging two or more resonant modes within the bandwidth of operation. It involves proper selection of aspect ratio and understanding of electric field distribution within the DRA. Generally, the modes which have similar radiation patterns are merged and hence radiation properties remain unaffected. Subsequently, RDRAs and cylindrical DRAs are studied to observe the correlation between the two in [77] and shown in Figure 9. The aspect ratios, i.e. radius to height ratio for cylindrical DRA case, length to width and length to height ratio for RDRA case, are varied to improve bandwidth. It is observed that bandwidth improves up to certain value and then start degrading. In [78], an RDRA with dual resonances is proposed based on optimum aspect ratio. If suitable aspect ratio is selected then two resonant modes, fundamental

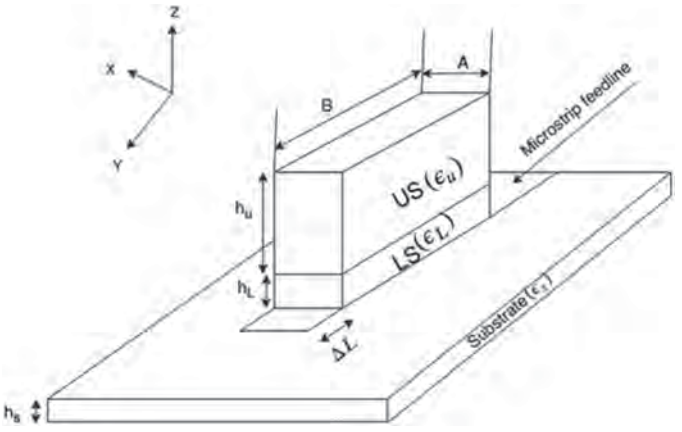

Figure 8. Investigations on two segment dielectric resonator antennas [75].

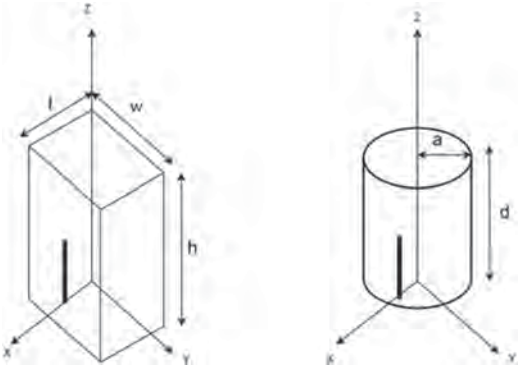

Figure 9. Wideband cylindrical DRAs and RDRAs [77].

TE_{111} mode and higher order mode TE_{113}, can be excited simultaneously which improves bandwidth up to 16%.

The slight variation of stacking method is hybrid RDRA in which either feed simultaneously act as radiator or two radiators are used [79,80]. It results in improvement of the bandwidth by merging of resonances of radiators and or feed in the bandwidth of operation. Thus, significant improvement in the bandwidth is achieved. Two different radiators, RDRA and slot antenna are excited in the bandwidth of operation in [79]. If both radiators radiate similar to horizontal magnetic dipole then radiation characteristics are not affected. Also, the bandwidth improves up to 25% by merging of two resonances in the bandwidth of operation. Both radiators are excited with the microstrip feed line method. In [80], two resonant modes RDRA and feeding CPW inductive slot as shown in Figure 10, are merged in the bandwidth of operation. The bandwidth achieved is 28.9% (4.71–6.3 GHz). It is observed that both have different radiation pattern which is undesired. By loading of DRA on CPW inductive slot, the radiation pattern modifies and desired broadside radiation pattern is obtained.

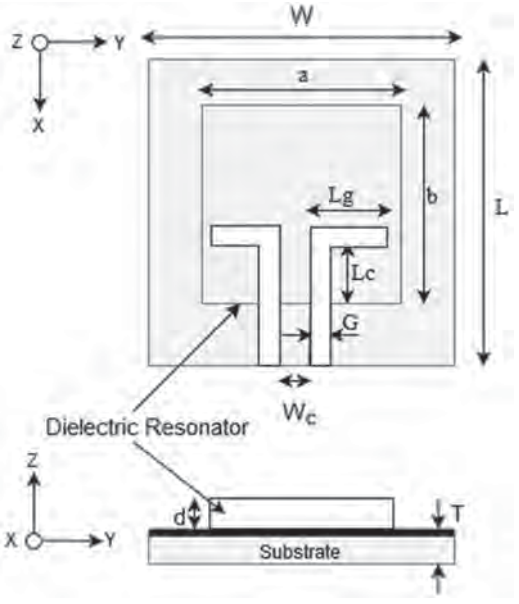

Figure 10. A compact wideband hybrid dielectric resonator antenna [80].

Matching network such as quarter wave transformers or matching stubs are also suitable for improvement of bandwidth. It alters input impedance of the RDRA to improve coupling with feed. These matching networks can be external or incorporated within the DRA. Such external networks degrade radiation efficiency because of increased insertion losses and hence less preferred. Similarly, a microstrip feed loaded with a conformal patch to facilitate wide impedance matching with a modified RDRA is explored in [81]. An asymmetric RDRA with slots for UWB applications is excited by the conformal patch. The patch does not contribute to any radiation and is used for impedance matching.

3.2. Low profile and compact RDRAs

Low profile refers to the condition when height of the RDRA is significantly smaller than the other two dimensions [1]. However, there is a limitation on the minimum height which can be achieved for a given resonant frequency and is independent of shape of the DRA [2]. The reason being when height is reduced significantly the field distribution becomes more dependent on the coupling apertures and feed. Then DWM fails and results in inaccurate calculation of resonant frequencies for low dielectric constant materials. Thus, designing of low profile RDRA is a challenge. The simplest method to design compact RDRA is selection of high dielectric constant material. But it has high-quality factor and thus bandwidth reduces. So, there is a tradeoff between size and bandwidth achieved from RDRA.

Other method to achieve compactness is to load the RDRA or incorporate a metal sheet. This method reduces the resonant frequency and bandwidth drastically. It also affects the symmetric pattern of radiation by distorting the pattern and/or increasing the cross polar component. Numerous low profile and compact RDRA designs are proposed based on edge grounding, metallization, and high dielectric constant material [57,82–97]. In [82], a low

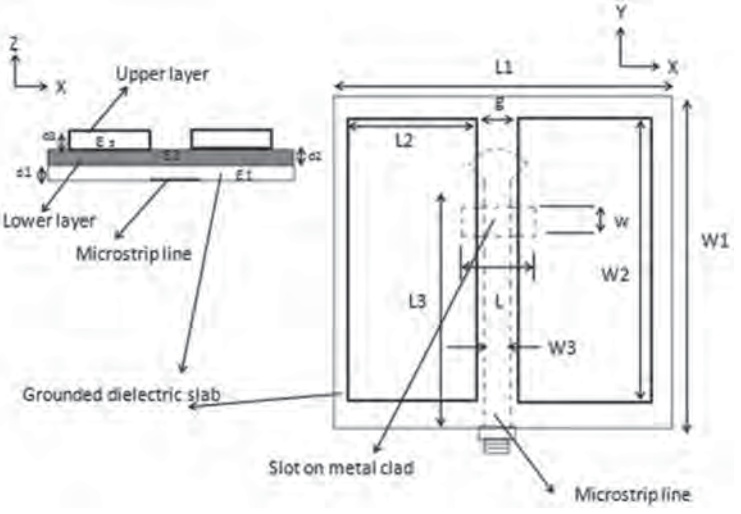

Figure 11. A low-profile and high-permittivity DRAs with enhanced bandwidth [82].

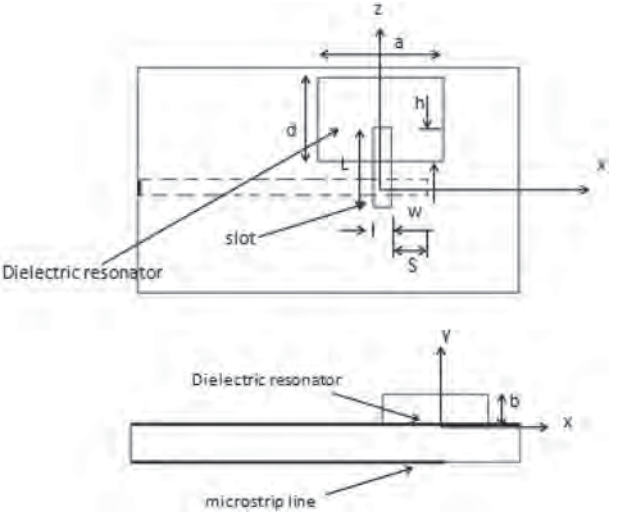

Figure 12. Low profile DRAs using a high permittivity material [83].

profile RDRA is designed with the high dielectric constant material, $\varepsilon_r = 93$ as shown in Figure 11. The strategic arrangement of different layers improved bandwidth to 10.49%.

Another design [83] shown in Figure 12, is proposed with the high dielectric constant material where the relationship of height of RDRA with free space wavelength and dielectric constant is established. The widest bandwidth of 3.2% is achieved from square base RDRA.

The substrate integrated waveguide (SIW) based low profile RDRA is proposed in [84] at 35 GHz with 11% bandwidth. The SIW used for excitation supports dominant TE_{10} mode. The dielectric constant of the DRA is $\varepsilon_r = 10.2$. Next, low profile square base RDRA design [85] is proposed with high dielectric constant material. The coupling between CPW feed and

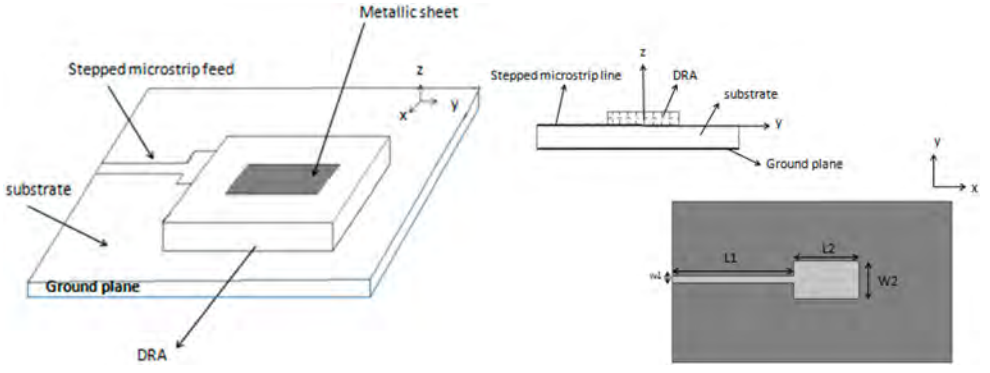

Figure 13. Microstrip fed low profile and compact DRAs [86].

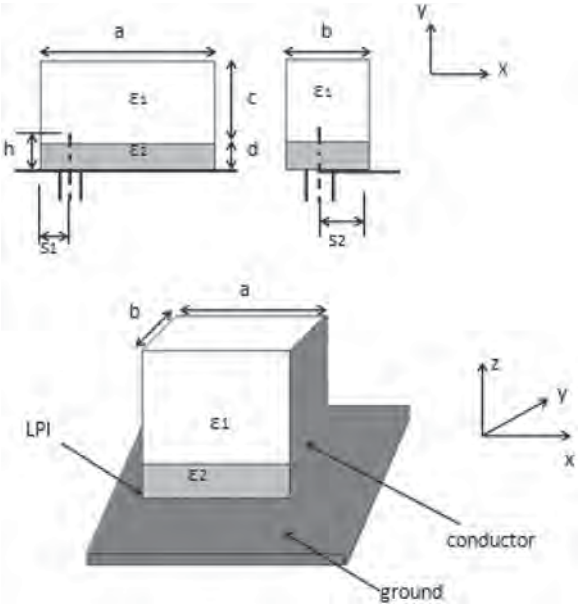

Figure 14. Compact DRAs with Ultrawide 60%–110% bandwidth [89].

RDRA is achieved through a slot. The dielectric constant is $\varepsilon_r = 79$ which offers bandwidth of 2.4% and excites fundamental mode.

In [86], modified stepped microstrip line feed excites the RDRA as shown in Figure 13. The modified feed ensures smooth impedance transition between the feed and DRA. Subsequently, compactness is achieved through placement of patch on the top of DRA. The improvement in the bandwidth is up to 17%. Two cases are considered when patch covers the DRA fully and partly. The compactness is directly related with the size of the patch but inversely related to bandwidth. A similar concept with edge grounding and perforations has been explored in [87,88], where half of the material has been removed using Van Bladel approximation and compactness is achieved by edge grounding. Figure 14 shows a compact wideband RDRA with bandwidth of 110% (3.1–10.6 GHz) [89]. The compactness

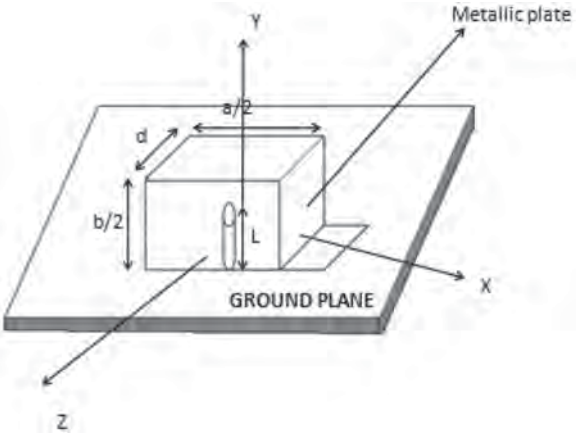

Figure 15. Characteristics of half-volume DRAs with different permittivities [57].

is achieved by edge grounding while bandwidth is improved by a low dielectric constant insert between dielectric resonator and ground plane.

The authors in [90] studied of half RDRA and cylindrical DRA and used FDTD method for simulations. They incorporated edge grounding method for size reduction and observed a shift in the resonant frequency from 1.1 GHz to 0.9 GHz with the reduction in bandwidth from 11.5% to 3.8% for the RDRA case. Another variation is proposed in [57] as shown in Figure 15, where half RDRAs with different dielectric constants are studied. It is observed that radiation efficiency decreases with the increase in dielectric constant. Edge grounded compact rectangular and cylindrical DRAs are proposed [91] where volume is reduced by half. The radiation efficiency and bandwidth decreases significantly through incorporation of metal plate.

In [92], new resonant mode, $TE_{\delta 01}$ is studied and it is observed that modified RDRA improves radiation efficiency with stable boresight radiation pattern. A compact wideband RDRA is proposed in [93]. The bandwidth is improved by a modified patch (bevel shape) between the DRA and coaxial probe, along the vertical plane. Also, air gap is provided between the dielectric resonator and ground plane. Additional metal plate for short circuit is incorporated to improve radiation characteristics such as radiation pattern. The improvement in the bandwidth is up to 96% (2.13–6.08 GHz). The cylindrical DRAs and RDRAs are designed using additional metal plate at the top for compactness [94]. It is concluded that the wave number in the direction, where metal plate is placed, reduces to zero. It makes the antenna geometry independent of the dimension along the side covered with the metal plate. Similarly, the perfect electric conductor and perfect magnetic conductor are used to achieve compactness for rectangular and cylindrical DRAs [95]. The perfect magnetic conductor condition is achieved by high dielectric constant interface. A quarter RDRA with the bandwidth of 26% and size reduction of 75% is achieved. Also, U-shaped DRA inspired from RDRA is proposed which offers bandwidth of 35% and size reduction by 50%. Hook shaped co-axial probe is used for the excitation. Next, compact RDRA is designed based on the placement of metal plate on the top side of the RDRA [96]. The resonant frequency lowers from 6.1 GHz to 2.37 GHz which is 61% while reduction in the bandwidth is from

13.3% to 2.74% which is around 92%. A modified RDRA is divided into half and at the center, metal plate is attached [97]. The resonant frequency of the two segments is adjusted through optimum aspect ratio of the two segment DRAs. Merging of two resonant modes improves bandwidth up to 76.8% (3.32–7.46 GHz). In addition to wide bandwidth a reduction in volume by 41.5% is achieved. Loading of metamaterial for improving the peak gain of the RDRA has also been explored in [98,99]. This has been explored by placing the metamaterial in both nearfield and far-field of the RDRA to facilitate the directionality along the normal direction to the RDRA.

3.3. Circularly polarized RDRAs

The circularly polarized antennas are preferred over linearly polarized due to misalignment between transmitter and receiver side of antenna. In addition to it, they suppress multipath problem such as reflection from buildings, ground, etc. The circularly polarized antennas are required in modern wireless communication systems, satellite communication, and radar systems. Therefore, various RDRAs are investigated to achieve circular polarization. The circular polarization can be achieved by dual or single feed. The stringent conditions are: excitation of two orthogonal modes with the same amplitude and quadrature in phase. Dual fed circularly polarized RDRAs offer wider axial ratio bandwidth in comparison to single fed. However, dual feed method requires more space to accommodate additional feed because feeds are designed externally. Numerous circularly polarized antennas are proposed based on aforementioned two methods [100–114]. The circularly polarized square microstrip antenna and cylindrical DRA is designed with the single feed in [100] as shown in Figure 16. The circular polarization is achieved by adjusting two arms of the cross slot coupling and cylindrical DRA, offers 3-dB axial ratio bandwidth of 3.91%. In another technique, circularly polarized cylindrical DRA is designed based on the comb-shaped slots carved [101] as shown in Figure 17. The circular polarization depends on the number of such slots carved and offers 3-dB axial ratio bandwidth of 4% when five such slots are carved.

Authors reported in [102], a cross-slot coupled dual-band circularly polarized RDRA as shown in Figure 18. The high aspect ratio of 3.2:1 of RDRA and cross slot with unequal arms results in simultaneous excitation of three orthogonal degenerate modes: TE_{111}, TE_{121}, and TE_{131}. The lower resonance is due to TE_{111} and TE_{121} modes while higher resonance is because of TE_{131} mode. The impedance bandwidth of 24.3% and 6.2% in conjuncture with 3-dB axial ratio bandwidth of 19.8% and 9.7% is achieved at lower and higher band respectively. The additional parasitic patch on RDRA in [103] is used for circular polarization. Subsequently, impedance bandwidth achieved is 11.94% with a 3-dB axial ratio bandwidth of 3%. This is as shown in Figure 19.

In [104], a compact hollow RDRA is designed for circular polarization with an under laid quadrature coupler as shown in Figure 20. Two types of loads are used: external 50 Ω load and metal strip loading. It offers impedance bandwidth of 24.95% with 3-dB axial ratio bandwidth of 33.8%. A compact wideband circularly polarized RDRA is designed in [105]. The circular polarization is achieved through two parasitic metal strips. Also, the central portion of the RDRA is removed which makes it rectangular ring DRA. Two additional metal strips create new current paths and results in wide 3-dB axial ratio bandwidth of 51% (3.4–5.75 GHz) with an impedance bandwidth of 54% (3.4–5.95 GHz).

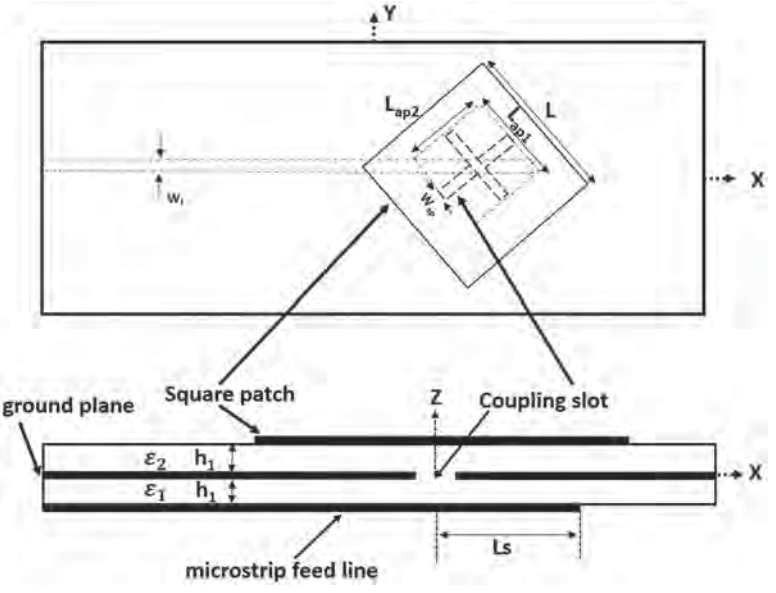

Figure 16. Cross-slot-coupled microstrip antenna and DRA for circular polarization [100].

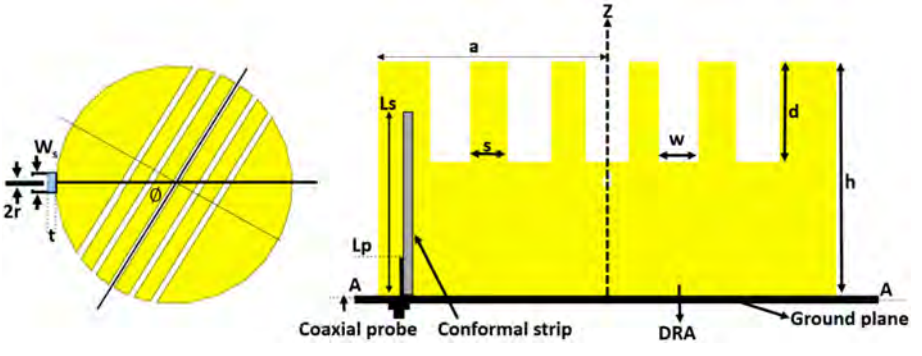

Figure 17. Comb-shaped circularly polarized DRA [101].

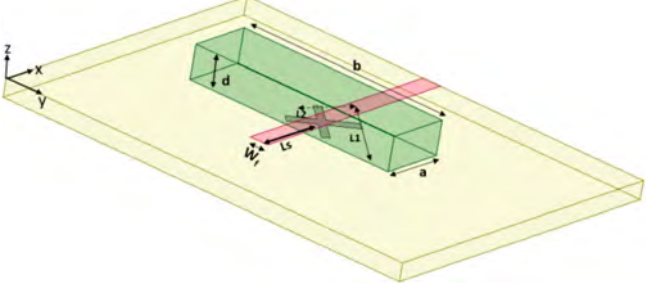

Figure 18. Cross-slot-coupled wide dual-band circularly polarized RDRA [102].

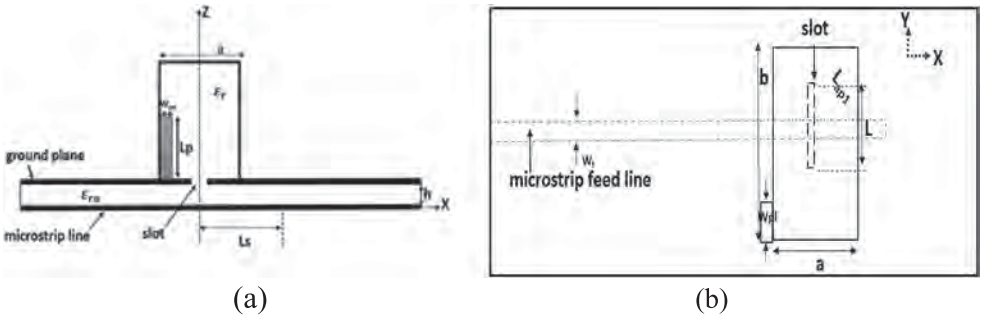

Figure 19. A circularly polarized RDRA with a parasitic patch [103].

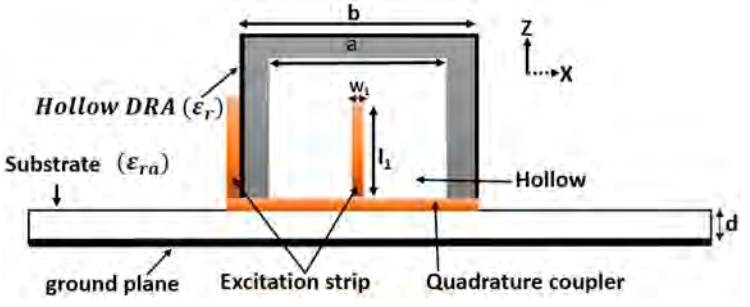

Figure 20. Compact circularly-polarized hollow RDRA with an underlaid quadrature coupler [104].

A microstrip line fed notch RDRA is proposed for circular polarization where inclined slot offers impedance bandwidth of 20% with 3-dB axial ratio bandwidth of 5% [106]. A low profile circularly polarized RDRA is proposed in [107] where circular polarization is achieved through a rectangular aperture carved onto the ground plane. The excitation technique is microstrip feed line and a 3-dB axial ratio bandwidth of 3% is achieved. In [108], circularly polarized stair shaped DRA is designed for wide circular polarization where different resonant frequencies are obtained with orthogonal modes. For excitation, an inverted trapezoidal probe is used which offers impedance bandwidth of 37% in conjuncture with the 3-dB axial ratio bandwidth of 22%. Authors proposed in [109] that a hollow RDRA can give both, linear and circular polarization. The linear polarization is achieved with a metal strip placed at center while circular polarization is obtained when strip is at an offset. The co-axial probe feed is used for excitation and offers impedance bandwidth of 32.5% (2.06–2.86 GHz) in conjuncture with the 3-dB axial ratio bandwidth of 12.4% (2.26–2.56 GHz). Single fed dual-band circularly polarized RDRA is designed in [110] which excites two resonant modes, TE_{111} and TE_{113}. The truncation of two opposite edges generates circular polarization and a groove along the diagonal tunes the upper band axial ratio. The impedance bandwidth of 25.3% (1.45–1.87 GHz) and 35.3% (2.1–3.0 GHz) in conjuncture with the 3-dB axial ratio bandwidth of 6.3% (1.53–1.63 GHz) and 3.68% (2.4–2.49 GHz) respectively is achieved for lower and upper bands. Idea of concentric open half loops is discussed in [111] to obtain circular polarization in RDRA. It is achieved by attaching end of the outer half loop with co-axial probe. The guided current distribution along the open half-loop strips generates circular polarization and offers impedance bandwidth of 21%

in conjuncture with 3-dB axial ratio bandwidth of 14%. In [112], quadrature fed RDRA is designed for circular polarization where two resonant modes, fundamental TE_{111} mode and higher order TE_{113} mode are excited. The additional metal strips generate circular polarization by exciting orthogonal pair modes of TE_{111} and TE_{113}. The proposed design offers impedance bandwidth of 32.8% (2.7–3.76 GHz) and 4-dB axial ratio bandwidth from 2.6–3.78 GHz. Modified C-shaped DRA gives circular polarization in [113] when CPW is used for excitation with an additional grounded metal strip. It results in impedance bandwidth of 58% (3.45–6.26 GHz) and 3-dB axial ratio bandwidth from 3.59–5.98 GHz. In [114], square-shaped slots on an RDRA placed along the diagonal position of the cross section generate CP in the RDRA. The slots also aid in improving the impedance bandwidth of operation.

3.4. RDRAs array

DRAs can be arrayed to achieve higher gain or shaped radiation pattern similar to other low gain antennas. In [115], a new type of planar antenna subarray consisting of RDRAs which are excited using a passive corporate microstrip feed and apertures is proposed. A four element subarray is proposed where individual elements are arranged in a rectangular fashion with half wavelength spacing between them. This design offered 10-dB impedance bandwidth of 18% (6.56–7.84 GHz) with the maximum achieved gain of 11.3 dB in the boresight direction. The cross-polar level was within the limit of −20 dB. A series fed linear RDRA array fed by slots in the ground plane of dielectric image guide is proposed in [116]. The array size is seven-elements and fifteen-elements arranged in a linear manner. The design offered gain of 10.07 and 13.9 dBi respectively at 10 GHz. The dielectric image guide is covered with metallic reflectors in order to suppress back radiation. Subsequently, front to back lobe radiation improved upto 20 dB for both the array sizes. In [4], simple high gain aperture coupled RDRA array with parasitic elements is investigated. The RDRAs are arranged in seven-element linear array manner and five-elements in cross-shaped array, resonant frequency is 3.2 and 2.98 GHz respectively. The gain achieved is 10.1 dB at 3.2 GHz and 11.14 dB at 2.98 GHz. Thus placement of parasitic elements very close to active/driven element can improve boresight gain with boresight and fan beam radiation patterns. The RDRA array is proposed for microwave energy harvesting and far-filed wireless power transfer [5] as shown in Figure 21. The array size is 1×3 and 5×5 with the resonant frequency $\sim$5.5 GHz. In [6], RDRA array of order 1×4 is proposed with wide bandwidth of 17% (6.2–7.35 GHz) and circular polarization bandwidth of 10% (6.2–6.85 GHz).

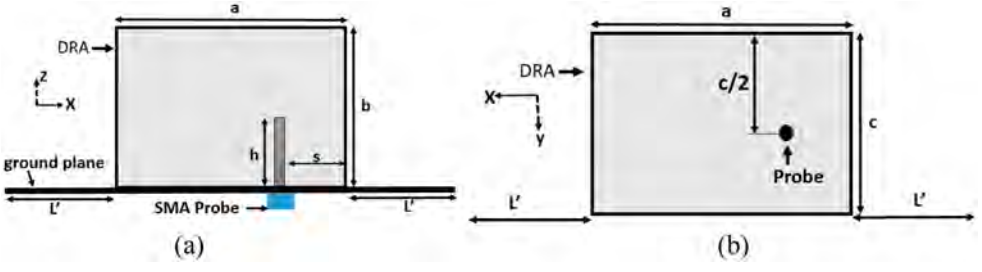

Figure 21. DRA arrays for microwave energy harvesting and far-field wireless power transfer [5].

The targeted application is microwave image sensing. The proposed design offered maximum gain of 13.6 dBi with peak gain variation from 12.1–13.6 dBi over the complete circular polarization bandwidth. An array of size 2×2 by exciting higher order modes is proposed for THz imaging at 340 GHz using 180 nm CMOS technology [7]. The gain improvement of 7 dB compare to conventional on-chip patch is obtained which can improve performance of the THz system. In [8], a SIW series fed 4 element array is proposed to operate in the frequency range 36–39 GHz. The gain is improved upto 12 dBi by suitably placing parasitic DRA elements.

3.5. Multiple-input multiple-output (MIMO)and diversity RDRAs

MIMO technology is based on multiple antennas at transmitter and receiver side to improve channel capacity in order to meet demands of high-speed modern communication systems. However multiple antennas increase the overall size of such system while close spacing among antennas increase the mutual coupling, which is undesirable. Since mutual coupling is the energy absorbed by a proximate antenna when another antenna is radiating which can severely affect the performance parameters such as radiation pattern, reflection coefficient and input impedance of MIMO antennas.

In view of this, in [9], a simple RDRA is proposed for polarization diversity by exciting two orthogonal modes, i.e. TE^{x}_{111} and TE^{y}_{111} which can be selected with a manual switch. The operating frequency is 2.36 GHz and dielectric material has $\varepsilon_r = 37$. The design provides good isolation but manual switching is a problem. In [10], a compact six-port DRA array based on spatial, polarization and angle diversities is investigated. Two RDRAs each with three ports, constituted array which resonates at 2.65 GHz, uses a dielectric material with $\varepsilon_r = 19.6$ for WLAN application. The design is robust and offered good performance when measured in indoor office scenarios for four 6×6 multiple antenna systems with isolation upto 12 dB. However, the outage capacity limited to 1.5 bits/s/Hz because of DRA array's lower channel gain. A MIMO RDRA is proposed to meet requirement for 2.6 GHz Long Term Evolution (LTE) applications in [11]. Two different excitation schemes, co-axial feed and coplanar waveguide feed are used to excite two orthogonal modes. The design offered 10-dB impedance bandwidth of 25% (2.4–3.09 GHz) at coaxial port and 47% (2.09–3.38 GHz) at coplanar waveguide port with correlation coefficient $\sim$0.03 and nearly 10 dB diversity gain at the resonant frequency of 2.6 GHz. However, size of the antenna is bulky which can be reduced by selecting high dielectric constant material. In [12], a compact dual-band MIMO RDRA is proposed to meet the requirements of entire WiMAX and WLAN bands simultaneously. To achieve compactness a high dielectric constant material is placed above low dielectric constant material. The envelope correlation coefficient (ECC) is within $\sim$0.1309 and $\sim$0.0024 at both the bands while measured diversity gain is $\sim$10 dB. The isolation is improved by introducing defected ground structure on the ground plane. Two elements MIMO RDRA design is proposed in [13] where upper side of substrate contains an RDRA and bottom side another RDRA as shown in Figure 22. The proposed design is compact with isolation of 15 dB between all the four ports achieved by exciting orthogonal modes and pattern diversity due to unique arrangement of RDRAs. The ECC is below 0.25 and suitable for WLAN (5.15–5.35 GHz) applications. An extensive theoretical review work on the different mutual coupling reduction techniques available is presented in [14]. Dual-port RDRA with orthogonal feeding structure is proposed for improvement of isolation [15].

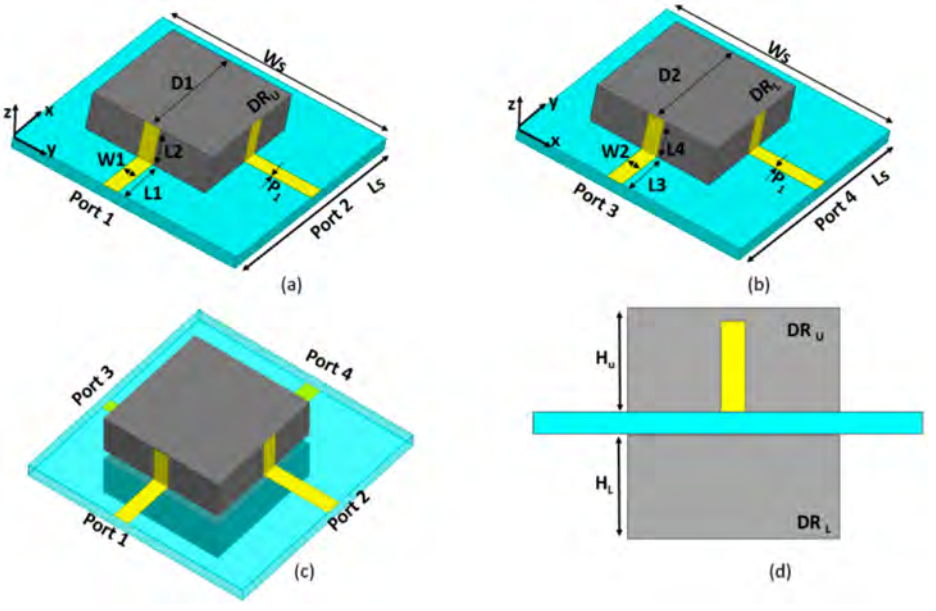

Figure 22. Pattern diversity based double sided DRA for MIMO applications [10].

The design is simple and compact targeting at operating frequency of 1.8 GHz which is suitable for LTE application. The decoupled orthogonal modes are excited to improve isolation. In [16], two ports excite the same mode in the RDRA. The isolation is improved by incorporating double slit in the ground plane but the fabrication complexities exist due to housing of dielectric resonator in the substrate. In [17] a wideband MIMO RDRA is proposed which improves isolation by orthogonally placing mushroom-shaped dielectric resonator. However, structure may require efficient fabrication tools to fabricate mushroom-shaped DRA. Three port MIMO RDRA is proposed by exciting three decoupled modes [18]. The design can be used as three-port MIMO or two-port MIMO. In [19] two-element tree-shaped DRA array is proposed for UWB (3.95–10.4 GHz) based on periodic C-shaped DGS. The isolation achieved is within 15 dB over the entire band but structure is complex. Dual port MIMO is proposed by combining L-shaped DRA and CDRA in [20]. The design is made compact and wide band by using parallel metal strips and slits on the ground plane. Further in [21], a circularly polarized MIMO design is proposed. The design uses truncation along the two corners of DRA to improve the axial ratio bandwidth. The electromagnetic band gap or EBG structure on the ground plane improves isolation up-to 26 dB. In [22], another CP MIMO design is proposed which offers improved isolation about 28 dB. The targeted application is Wi-Max and design uses parasitic patch to achieve CP. Interestingly in [23,24] decoupling structures are proposed to improve the isolation in MIMO antennas. Total four metal-vias are strategically placed within the DRAs in [23] which improve isolation up-to 30 dB. In [24], metal strips are used which have no significant effect on radiation characteristics because strips are placed in weak electric field region of dielectric resonator. Both the designs are suitable for 5G millimeter wave application. Since the increase in mutual coupling can degrade the performance of MIMO systems. The simple and effective available techniques are orthogonal modes [11,13,15], DGS [12,19], parasitic or slot element

[16,21,22], and decoupling networks [23,24] are proposed for designing RDRA MIMO based systems.

4. Review of the CDRA geometry

This section shall provide a comprehensive review of the CDRA and its associated geometries. This section has been divided into various sub-sections to emphasize on the major contribution. Finally, a detailed table of comparison with the most promising contributions of the CDRA geometries is tabulated in various Tables based on applications.

4.1. Wideband and multiband CDRA geometries

In [25], authors propose to use Sea water and distilled water as dielectric materials. A broadband hybrid water antenna operating at very high frequency (VHF) band is presented, in which a simple seawater monopole is loaded with two distilled water cylinders working as dielectric resonators (DRs). By employing the loading technique; multiple close resonances are introduced to broaden the impedance bandwidth of the seawater antenna. A wide bandwidth from 69 to 171 MHz for $|S_{11}| < -10$ dB is achieved and the radiation patterns are stable in the desired band. The proposed structure is shown in Figure 23(a) and the S parameter response is depicted in Figure 23(b).

A popular way of improving the bandwidth is by stacking of different dielectric substrates. This effectively reduces Q factor and thus improves the bandwidth. This concept has been rigorously investigated in [26], where the authors use multilayered stacked dielectric materials on a half-split CDRA and achieve a bandwidth from 5.55 to 12.08 GHz. The similar stacking concept has also been explored in [27], where impedance bandwidths up to 68.1% compared to 21.0% for a homogeneous DRA with the same size and resonant frequency is achieved. In [28], the authors use stacking method to enhance the 3 dB axial ratio and impedance bandwidth of the circularly polarized cylindrical dielectric resonator antennas excited by an external tape helix. A dielectric cylinder with lower permittivity than the basement cylindrical dielectric resonator is placed concentrically on top of the basement cylinder. The new configuration offers an axial ratio bandwidth up to 11% and impedance

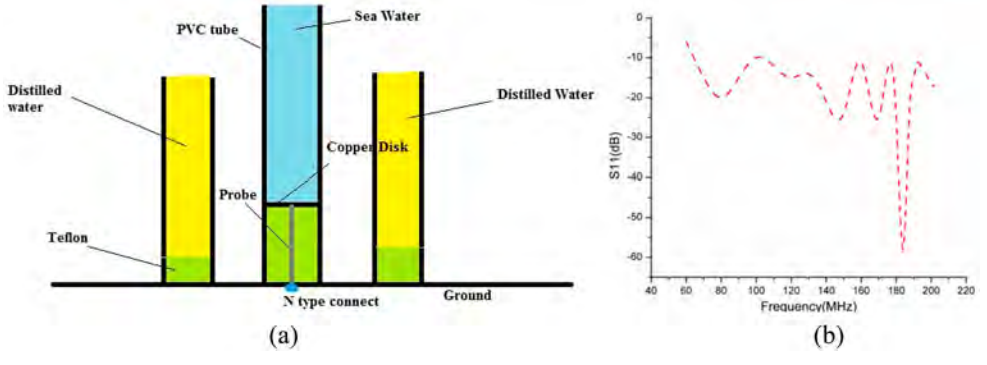

Figure 23. Figures in tandem with reference [25]. (a) Proposed structure (b) S parameter response.

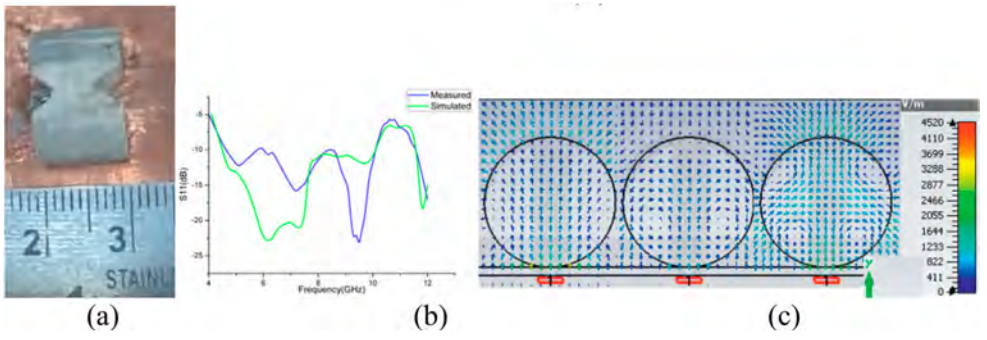

Figure 24. Figures from reference [29]. (a) Fabricated prototype. (b) The $|S_{11}|$ plot. (c) The three identified modes at 5.12, 7.28 GHz and9.48 GHz respectively.

bandwidth of 31%. The authors calculate the effective permittivity as follows:

$$\varepsilon_{eff} = \frac{h_1\varepsilon_{r1} + h_2\varepsilon_{r2}}{h_1 + h_2} \tag{33}$$

where $h_1, h_2, \varepsilon_{r1}$ and ε_{r2} are height of substrate 1, height of substrate 2, permittivity of substrate 1 and permittivity of substrate 2 respectively. Authors in [29] use an interesting concept by minimizing the contact area between DRA and the ground plane. As a consequence, more current is coupled in the DRA which is subjected to high change in permittivity at the dielectric air interface, resulting in lowering of Q factor and improved bandwidth. The proposed DRA offers a bandwidth from 4.5 GHz to 10.1 GHz. The fabricated prototype of the proposed laterally placed CDRA is as shown in Figure 24(a). Figure 24(b) shows the S-parameter response and Figure 24(c) shows the three modes inspected. The vector electric field distributions are shown at the three resonant frequencies 5.12, 7.28 GHz and9.48 GHz. For the first resonant point, the mode is similar to the $HE_{11\delta}$ mode, the second resonant point resembles to $HE_{12\delta}$ mode and at 9.48 GHz the field distribution resembles the mode $HE_{21\delta}$ of CDRA. This is in conjecture with the discussion of modes of CDRA in Section 2 (B).

Using the similar formula of Equation (33) and a modified ψ shaped feed line, the authors in [30] have achieved triple-band response exciting $HE_{11\delta}$, $HE_{12\delta}$ and $TM_{01\delta}$. The triple band response includes 2.5–3.02 GHz, 3.76–3.86 GHz and 4.38–4.72 GHz. The frequency response of the three proposed prototypes with different feed configuration is shown in Figure 25.

Another important concept of improving the bandwidth of the DRA is by using multi-element approach. Different permittivity based DRAs or same permittivity materials can be placed as parasitic element to the primary DRA or be equally excited by a common probe/feed, to achieve wideband response. However, unlike arrays where each element is excited individually, multi-element approach generally confines to single feed or shared feed technique.

In [31], a compact dielectric resonator antenna for ultra-wideband vehicular communication applications is proposed. Two cylindrical dielectric resonators are asymmetrically located with respect to the center of an offset rectangular coupling aperture, through which they are fed. Optimizing the design parameters results in an impedance bandwidth of 21% (5.9–7.32 GHz) in the lower band and a 53% relative bandwidth (8.72–15 GHz) in the upper

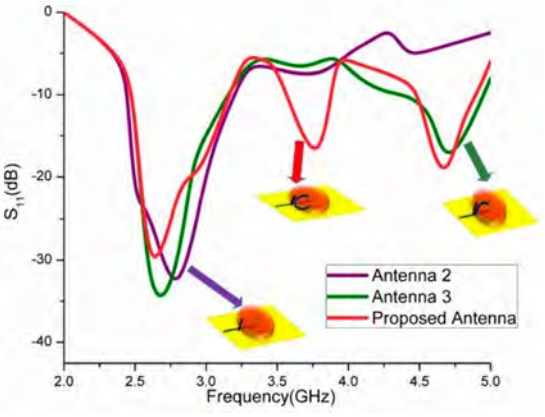

Figure 25. The proposed feed configurations and Return Loss plot as re-simulated from reference [30].

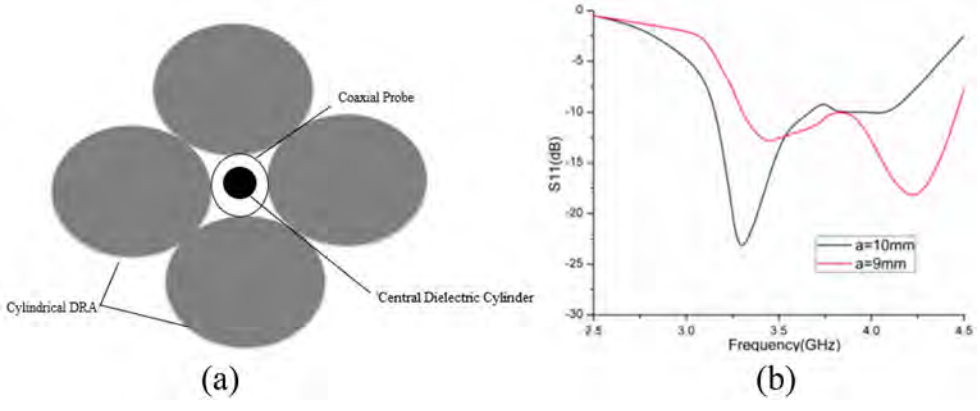

Figure 26. The proposed four element CDRA. (a) Fabricated prototype. (b) S-parameter simulated response from [32].

band. The maximum achieved gain is 12 dBi. Similarly in [32], a new four-element cylindrical dielectric resonator (CDR) array is proposed as a wideband low profile monopole-like antenna which employs the dominant $HEM_{11\delta}$ mode in each CDR. A 29% impedance bandwidth with 4 dBi gain offering a compact size of 0.6 λ_0 by 0.1 λ_0 approximately is explored. Figure 26(a) shows the top view of the simulated structure and the simulated $|S_{11}|$ plot is shown in Figure 26(b).

The concept of multi-element DRAs is further explored in [33], where two cylindrical dielectric resonators that are asymmetrically located with respect to the center of a rectangular coupling aperture are fed through this aperture. The proposed configuration covers an impedance bandwidth of about 29% (9.62–12.9 GHz) and offers a gain of 8 dBi.

An interesting way of improving bandwidth is also by introducing slots in DRA. This reduces the effective permittivity and thus lowering down the Q factor and improving bandwidth. This concept has been explored in [34,35]. In [34], stepped radius DRA is explored for ultra-wideband response. The new hybrid antenna can easily offer a fractional bandwidth up to 110%. In [35], annular column of CDRA is proposed. The prototype

comprises of two components namely inner cylindrical dielectric and a loaded concentric column dielectric. The proposed antenna is centrally fed by a coaxial probe, and has a low profile of 0.175 λ_0 (λ_0 is the wavelength of the center frequency). Four conical radiation pattern modes ($TM_{01\delta}$, $TM_{02\delta}$, $TM_{03\delta}$, and $TM_{04\delta}$ modes) are excited and merged, providing an impedance bandwidth of 56% (3.14–5.56 GHz). The modes excited due to central feeding are in analogous to Section 2(B) discussion. A recent class of pattern reconfigurable CDRAs have been proposed in [36]. The DRA is composed of two zones: the inner zone is a solid cylinder fabricated by K9 glass ($\varepsilon_r = 6.85$) and the outer zone is filled with a dielectric liquid – ethyl acetate ($\varepsilon_r = 7.1$). The inner glass DRA is excited in its broadside $HEM_{11\delta}$ mode when the ethyl acetate is pumped out, while the conical $TM_{01\delta}$ mode is excited in the reconstituted cylindrical DRA when the ethyl acetate is pumped in. Consequently, a mechanical reconfiguration of broadside and conical radiation patterns can be achieved over a wide impedance bandwidth of 35.5% from 3.75 to 5.37 GHz. Similarly, segmented CDRA with stacked and angular rotation has been explore for wideband applications [37].

4.2. Compact and high gain CDRA geometries

Compact DRAs are those which apart from being electrically miniaturized can be contained in metallic cases or have metal elements aiding in miniaturization. The researchers in [38] employ stacking of two dielectric material technique to enhance the bandwidth of the antenna, and the metallic patch is used as a reflector for improving the gain and enforce compactness. The DRA is excited by the central coaxial probe feed with $TM_{21\delta}$ mode being observed at 6.7 GHz resonant frequency. The proposed antenna is fabricated, and a close agreement is found between simulated and measured results. The proposed structure offers wide impedance bandwidth of 7.5 GHz from 5.7 to 13.2 GHz. A peak gain of 6.8 dBi is measured over the desired frequency band. The proposed DRA finds prospective applications in Wireless Sensor Networks and sensor node application. The authors use Equation (33) by substituting the height *h* by the volume *V*.

Similarly in [117], a Bi-Cone geometry is formed by joining two conical sections from base to base. This aids to increase the surface area to volume ratio (S/V). Thus the impedance bandwidth of DRA is increased. The Q factor of any DRA is estimated as follows [118]:

$$Q = 2\omega_0 \frac{stored\ energy}{radiated\ power} \propto 2\omega_0 (\varepsilon_r)^p \left(\frac{volume}{surface\ area} \right)^s, \ where\ p > s \geq 1 \tag{34}$$

Thus, as the Q factor decreases, the bandwidth of operation increases.

To further miniaturize the Bi-Cone DRA, triangular notches and edge grounding is incorporated. The proposed DRA prototype is fabricated and measured. The measured results show an impedance bandwidth range from 2.8 to 7.38 GHz (93.1%) for ($S_{11} < -10$ dB). Moreover, the miniaturized Bi-Cone DRA has a volume of 7.58 cm^3, which is 74% less than the volume of the base structure. The figure of the shorted edge of Bi-cone DRA so achieved is given in Figure 27. Also shown in the figure is the S-parameter response of the proposed structure.

However, because of perturbation in the DRA, predicting the precise modes of the DRA becomes challenging. It can only be compared with a mode in the regular DRA by drawing equivalence in near filed orientation and far-field plots.

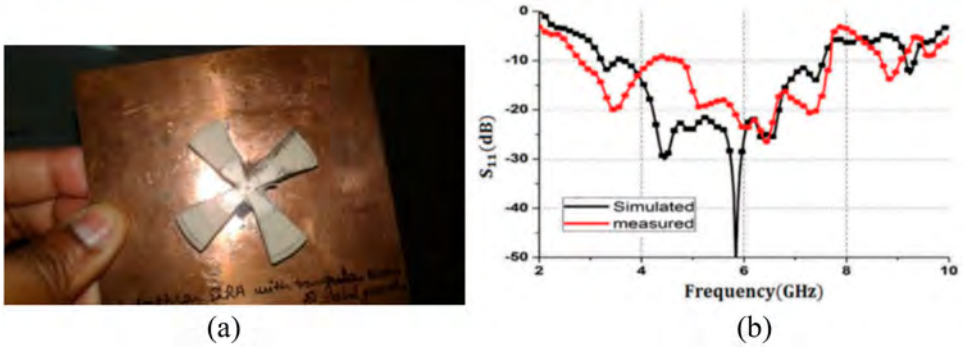

Figure 27. The figures as referred from reference [117]. (a) The fabricated prototype. (b) The S-parameter response of the proposed CDRA Bi-cone design.

Researchers in [119] proposed a CDRA with a double-annular patch and a metallic cylinder to obtain a large bandwidth and a high gain. The CDRA is excited for $HEM_{11\delta}$ and TM_{12} mode is excited on the patch. Together the patch and the cavity formed by the metallic cylinder provide a further higher gain and a larger bandwidth. Similarly in [120], a cylindrical dielectric resonator, an intermediate layer and a metallic cylinder are used to obtain a large bandwidth and a high gain. The intermediate layer structure can suppress surface wave propagation, which results in a gain improvement, and the cavity formed by the metallic cylinder provides a further improved gain. The measured results demonstrate that the proposed DRA achieves a large bandwidth of 23% from 5.4 to 6.8 GHz with a voltage standing wave ratio of < 2 and a high gain of around 11 dBi.

A novel pattern re-configurability with eight PIN diodes is explored in [121]. The CDRA is excited for higher order HEM_{212} mode at 5.71 GHz. The same mode, when diodes are turned ON preserves the $HEM_{21(1+\delta)}$ mode. For each direction, the antenna exhibits high gain (7.27 dBi), high efficiency (86.1%), low cross-polarization level, and similar radiation pattern. In [122], a single element circular slot aperture coupled Cylindrical Dielectric Resonator Antenna (CDRA) with a parabolic reflector is simulated and presented. The measured bandwidth of the single element CDRA is about 1.8% (5.32–5.52) while the simulated bandwidth is 1.11% (5.32–5.44 GHz). A detailed parametric study has been conducted to realize the effects of reflector parameters to increase the directivity of the designed antenna. The simulation of the antenna loaded with the parabolic reflector offers a gain of about240% as compared to the single element CDRA without reflector. In another investigation, researchers in [123], propose a novel Cylindrical Electromagnetic Band Gap (EBG) loaded structure on CDRA, to improve the peak gain. The EBG cancels on longitudinal fields, thus improving the gain in the transverse plane. The cylindrical electromagnetic bandgap structure is composed of two distinctive periodic structures. The first structure is made of metallic rings, while the second is formed of grounding vias, which are placed radially and circularly. The proposed structure is shown in Figure 28(a). The proposed structure resonates at 2.29 GHz (experimental) and offers a gain improvement of approximately 2 dBi. The improvement in gain as simulated can be seen from Figure 28(b).

A simple yet novel way to improve bandwidth is using the concept of merging of modes. The DRA can be properly tuned such that the nearby modes can be merged to offer wide

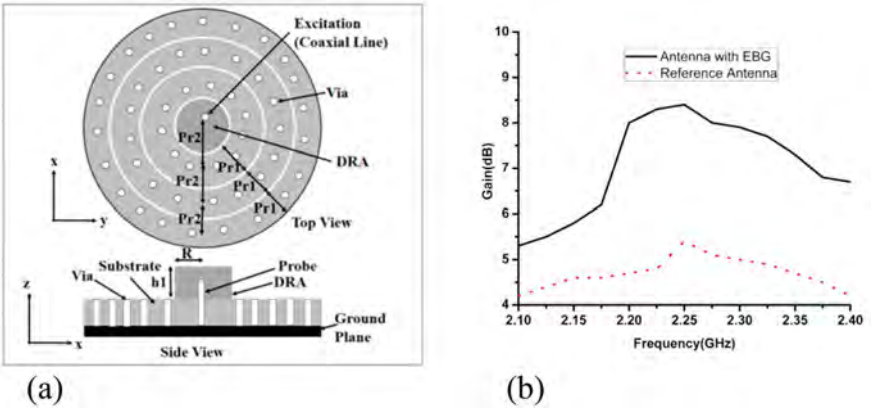

Figure 28. The figures of ref. [123] re-simulated. (a) The proposed geometry (b) Simulated Gain with and without the EBG structures.

bandwidth of operation. This concept has been implemented in [124]. The two higher order modes namely HE_{133} and HE_{123} are merged to offer wide bandwidth of operation by exciting the DRA using aperture coupling. By optimizing the dimensions of the aperture, a gain of 11.6 dBi is also achieved. The central frequency of the proposed DRA is 5.8 GHz with a 2.6% impedance bandwidth. The permittivity of 6.15 (Arlon) is used for simulations and measurements. As claimed in [125], aperture coupling is chosen so as to avoid excitation of unwanted lower order modes in the DRA. Similarly, a segmented CDRA integrated with conical horn demonstrated the capability of high gain in [126].

4.3. Circularly polarized CDRA geometries

Circular Polarization (CP) is generated when two orthogonal fields combine, thus offering orientation independence of operation. Such antennas can be classified as left handed circularly polarized (LHCP) or right handed circularly polarized (RHCP) depending on which of the two is dominant compared to the other by observing their respective radiation patterns.

In DRAs, the CP can be achieved from either providing a differential feed, modification in the single feed itself so that orthogonal fields are generated, by providing orthogonal slots to facilitate such fields or by providing necessary perturbation in the dielectric material so that orthogonal fields are generated.

The concept of feed line to excite quadrature fields is explored from [127–133]. In [127], conformal microstrip line feeding is used on a half split CDRA surface. The single microstrip line feed is split into two sections which by virtue of difference in their lengths provide a $\pi/4$ phase shift. The fundamental mode $HE_{11\delta}$ is excited which radiates in broadside direction. The proposed structure offers an input impedance bandwidth of 24.17% in the frequency range of 2.8–3.57 GHz (center frequency of 3.18 GHz). The axial ratio below 3 dB obtained is 7.7% in the frequency range of 3.11–3.36 GHz (at center frequency of 3.23 GHz). Similarly, the same mode can be excited by using a Helix feed using the Hansen-Woodyard condition further enhancing the axial ratio bandwidth deployed on a hollow CDRA. This has been explored in [128]. In [129], U-shaped slot feed is used to obtain CP on CDRA. The proposed

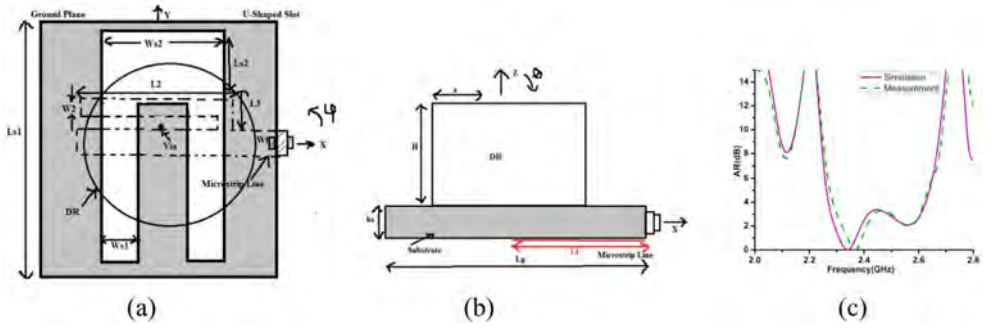

Figure 29. The figures with reference to [129]. (a) The U-shaped slot details. (b) The CDRA placed on the slot feed. (c) The simulated AR (dB) plot against frequency.

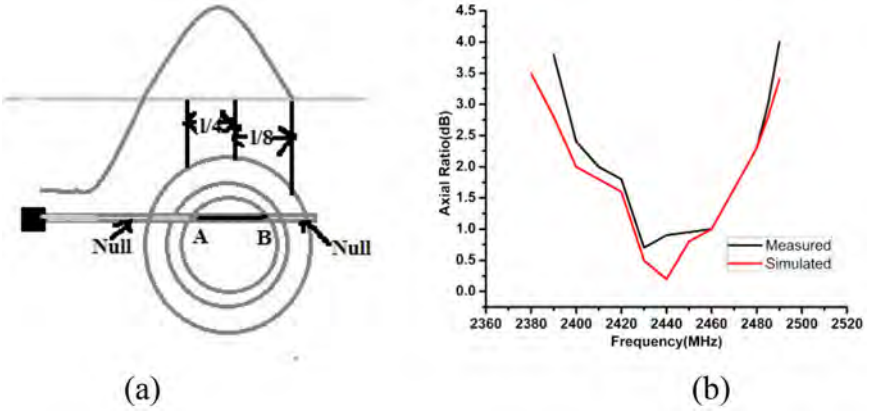

Figure 30. The figures as referred from [130]. (a) The proposed configuration. (b) 3 dB-AR bandwidth simulated plot.

structure is shown in Figure 29(a) and (b). The simulated axial ratio in dB (AR dB) is depicted in Figure 29(c).

The simulated bandwidth in [129] is from 2 to 2.61 GHz for $|S_{11}| \leq -10$ dB, whereas the 3 dB-AR bandwidth is from 2.31 to 2.61 GHz. This falls in the ISM band of 2.4 GHz of operation. For the same operating frequency, an offset from the microstrip feed line is also able to excite orthogonal modes. This is discussed in [130]. The CDRA is placed at an offset from the microstrip line with an extension of a stub length of $\lambda/8$ which generates orthogonal modes thus generating CP in the CDRA. The proposed configuration and the 3 dB-AR bandwidth plot areas shown in Figure 30(a) and (b) respectively.

A half split CDRA with an offset probe feed has been investigated in [31] to excite CP waves in the DRA. The design in [131] utilizes the radius to height ratio and feed position of the circular sector DRA to excite two resonant modes that are spatially orthogonal in polarization and in phase quadrature. Also, authors in [132], employ a Wilkinson power divider to provide a balanced power division. A phase shifter providing phase quadrature between the fields responsible for the generation of CP, is connected to the Wilkinson power divider. The 3 dB AR bandwidth is from 4.95 GHz to 7.65 GHz. In [133], researchers propose a partial

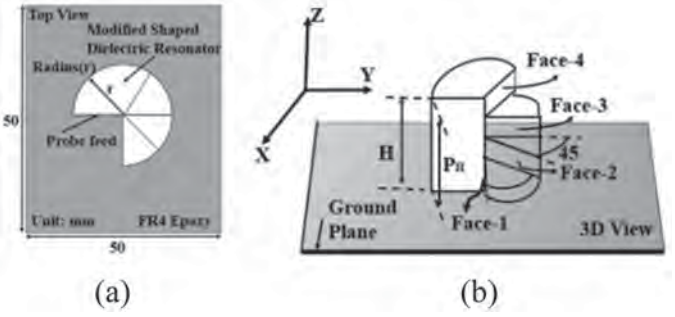

Figure 31. The geometry of the proposed structure as referred from [134]. (a) Top view of the structure. (b) The perspective view of the proposed structure.

ground plane and a modified annular-shaped microstrip line feed loaded with ring resonators to provide necessary conditions for generating CP. The proposed structure also supports compact and low profile CDRA requirements. This structure also offers triple-band response from 2.35–2.55 GHz, 3.35–3.65 GHz and 5.1–5.52 GHz. The average measured gain is 4.71 dBi for the antenna structure.

The perturbation theory explains the electromagnetic concepts with reference to shift in the resonant frequency due to the re-distribution of the Electric and Magnetic fields. While a slot in a DRA, lowers down the Q factor, thus improving the bandwidth of operation, it can also be used for providing quadrature phase shift between the linear fields leading to circular polarization. Introducing a slot also supports the perturbation theory. This concept for CP CDRA has been investigated in [134–136]. In [134], authors propose a stair case shaped perturbation which is deformed periodically with the same angular factor ("β" $= 45°$) along the azimuthal direction. In such an arrangement, assuming magnetic boundary conditions at the air-dielectric interface, the tangential electric fields are decomposed orthogonally in such a way that circularly polarized wave could be generated. This proposed structure offers an impedance bandwidth from 3.37 to 5.69 GHz and a 3 dB-AR bandwidth from 4.2 to 4.55 GHz. The geometry of the proposed structure is as shown in Figure 31.

In similar lines, authors in [135], use stair shaped slots leading to tuning and merging of the orthogonal mode pairs. This leads to wider 3 dB-AR bandwidth from 4.21 to 6.79 GHz and impedance bandwidth from 4.1 to 6.81 GHz. In [136], notches are created in the CDRA so as to excite CP. Researchers in [136] create notches at 45° and 225° on the CDRA which is excited by a microstrip line. This CP-CDRA operates on dual band from 4.57 to 5.79 GHz and 8.05 to 9.2 GHz exciting the $HE_{11\delta}$ mode. The axial ratio bandwidths in the dual bands are 4.74–5.5 GHz and 8.55–9.18 GHz respectively. The peak gains observed in the two bands are 4.3 dBi at 5.5 GHz and 5.8 dBi at 9 GHz respectively.

4.4. Novel techniques in CDRA

In this section, some novel variations on the conventional CDRA or new methods to excite or for prospective applications is explored. In [137], the authors employ the concept of stacking the CDRAs. The lower CDRA can be used as a novel feeding method to another DRA placed on top of it. The dielectric materials used is the same for both the elements stacked.

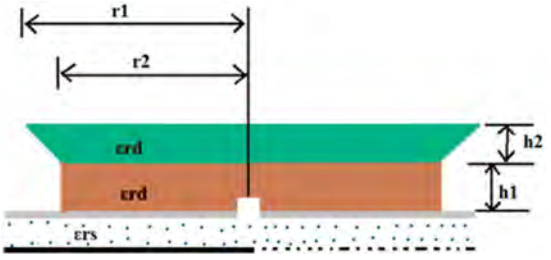

Figure 32. The proposed structure referred in [137]. The figure shows a conical DRA placed on the CDRA.

The lower element is excited by an aperture created on the ground plane and the upper element is excited by the lower CDRA. The upper element generates higher order mode ($HEM_{12\delta}$), whereas the lower mode ($HEM_{11\delta}$) resonates in the entire composite mass especially the lower CDRA. The best results for such a method are obtained when the upper element is replaced by a conical section DRA. A 8.3% and 13% matching bandwidth is obtained using the proposed structure. The proposed geometry is as shown in Figure 32.

In [138], K9 glass with $\varepsilon_r = 6.85$ is used for design of dual-band CDRA excited by aperture feed. The proposed designs make use of the fundamental mode HE_{111} and HE_{113} higher-order mode of the CDRA. The strip and slot fed excitation methods are used on the two ports of the antennas. A dual-band dual-polarized CDRA for DCS (1.71–1.88 GHz) and WLAN (2.4–2.48 GHz) bands and a wideband that covers the 2.4-GHz WLAN band are proposed and experimentally verified. In [139], a single-element CDRA with air intrusion is examined to design a new wideband antenna. This antenna is excited by a conformal strip offering 66% impedance bandwidth, thus accommodating four wireless bands (DCS, PCS, UMTS, WLAN) with 7.25–8.61 dBi peak gain. The air intrusion in the fabricated structure is introduced by placing foam beneath the CDRA slot to provide mechanical stability. Similarly, differential feed employed using coaxial cables and a 180° phase shifter is used to excite the CDRA in [140]. This arrangement apart from broadside radiation patterns, also offers very low cross-polarization levels. The prototype is fabricated and is experimentally verified.

In [141], CDRA with eight slots is inspected. The CDRA geometry is symmetrical and excites the fundamental $TM_{01\delta}$ mode. The eight slots are placed at equal angle spacing to preserve the symmetricity of the structure. The introduction of slots shifts the resonant frequency to higher side, i.e. 11.28 GHz with an impedance bandwidth of 56.56% ranging from 6.96 GHz to 12.45 GHz. Researchers in [142], have identified the $HE_{21\delta}$ mode responsible for generation of cross polar components in radiation patterns. The experimental proof is verified by perturbing the ground plane and then placing the CDRA on top of it which generates the $HE_{11\delta}$ and the $HE_{21\delta}$ mode. The two modes are depicted in Figure 33. The modes are in conjecture with the discussion in Section 2.2. Members of the same research group explore the detailed design guideline of exciting a CDRA for $HE_{12\delta}$ mode in [143,144]. It is established that the radiation pattern of $HE_{12\delta}$ mode is quite similar to the fundamental $HE_{11\delta}$ mode however, offering a higher gain.

Authors in [145], propose the use of CDRA for MIMO applications. The antenna operates in a frequency range from 3.7 to 7.25 GHz and offers isolation ($|S_{12}|$) of −17 dB between the ports. For improved impedance matching, partial ground plane with loaded novel circular shaped defected ground resonators are used. Similarly in [146], researchers explore a

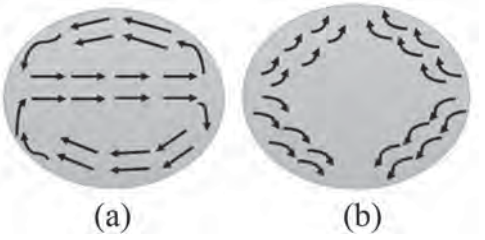

Figure 33. The modes identified in a CDRA as referred in [142]. (a) $HE_{11\delta}$ mode excited in the CDRA. (b) $HE_{21\delta}$ mode excited in the CDRA.

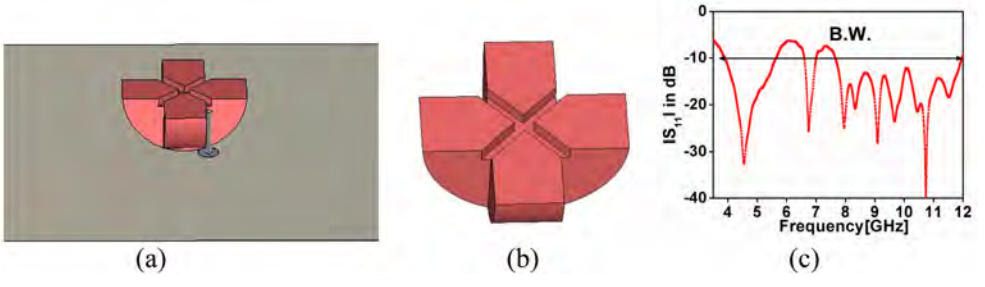

Figure 34. The proposed configuration as referred in [147]. (a) The Front view of the proposed geometry. (b) The top view showcasing the corrugations. (c) $|S_{11}|$ plot against frequency.

novel loop coupled with the CDRA to excite the $TM_{01\delta}$ mode. This method doesn't require any drilling in the CDRA. The experimentally verified resonant frequency for the mode is 5.31 GHz with an impedance bandwidth of 3.4%. The main finding is that the magnetic field induced because of the current loop excites the radiator by means of electromagnetic coupling.

In [147], a corrugated plus shaped inverted half cylindrical dielectric resonator (CDRA) antenna is analyzed for wireless multiband applications. The proposed DRA targets IEEE 802.11p standard wireless access in vehicular communication. Less contact base area to ground plane for inverted half cylindrical DRA & deployed corrugation plays an essential role for enhancement of the bandwidth and gain. In proposed antenna $HE_{11\delta}$, $HE_{12\delta}$, HE_{123} & HE_{142} hybrid modes are investigated. The presence of higher order modes contributes to enhancement of the gain. A low loss dielectric material, Rogers TMM10 ($\varepsilon r = 10.2$) is used to construct the antenna. This antenna covers the bands at 4.5 GHz (4–5.5 GHz), 6.75 GHz (6.6–6.9 GHz), 7.9 GHz & 11.5 GHz (7.7–11.8 GHz) resonant frequency respectively. The proposed geometry is shown in Figure 34(a) and (b) whereas the $|S_{11}|$ plot against frequency is shown in Figure 34(c).

In [148], a low profile stacked modified CDRA is proposed for wireless applications. A low profile antenna is one whose height is much smaller than other physical dimensions. Also, the field distribution is more dependent on secondary parameters like feed and coupling aperture, etc. The first proposed circular stair-step low profile DRA offers maximum gain of 8.57 dBi. The antenna offers a super-ultra-wideband of 15.2 GHz (i.e. 122.5% from 4.8 GHz to 20 GHz), which is achieved through semi-cylinder-shaped perturbations and stairstep fractal structure formed by the systematic stepped rotation of the structure, and, thus,

Figure 35. The first proposed configuration of the reference [148].

increasing the S/V ratio and decreasing the effective dielectric constant and lowering the Q-factor of the structure. The second proposed structure extends minimum volume and compact structure with a maximum gain and efficiency of 15.65 dBi and 94.89%, respectively. Figure 35 shows the fabricated prototype of the stair-stepped low profile DRA. The structures are highly perturbed and so predicting the exact mode of operation for such perturbed geometries is not possible.

A novel variation in the primary CDRA is by changing the radius along the azimuth plane. This traces an ellipse. Elliptical DRA has been explored in [149]. The radiator comprises of a semi-eccentric annular dielectric resonator, which is a semi-elliptical DR with a hollow elliptical cylinder. A vertical coaxial probe is located adjacent to a cutting surface of the DR to excite the proposed structure. The two main design parameters are the aspect ratio of the elliptical Dielectric resonator and the feed position. This DRA is designed for X band applications. The experimental results show a reflection coefficient bandwidth from 9.41–12.62 GHz and a 3-dB axial-ratio bandwidth of 5.71% (10.37–10.98 GHz). The measured peak gain varies from 4.17 to 4.78 dBic. The proposed geometry is shown in Figure 36.

Similarly, a Fibonacci series can be used to propose a variation in CDRA which resembles the elliptical DRA. This Fibonacci series based DRA is explored in [150]. An impedance bandwidth ($|S11| < -10$ dB) and 3-dB axial ratio bandwidth achieved are 106.5% (6.1–12.6 GHz) and18.9% (10.6–12.6 GHz), respectively. Fundamental $HE_{11\delta}$ and $HE_{12\delta}$ modes are excited at 9.1 and 10.8 GHz resonant frequency respectively and maximum gain attained is 7.6 dBi at 8.7 GHz. The fabricated proposed structure and its axial ratio& $|S_{11}|$ plots are shown in Figure 37(a) and (b) respectively.

4.5. Multiple-input multiple-output (MIMO) and diversity CDRAs

Many MIMO and diversity CDRAs are proposed to meet the requirements of 5G millimeter wave applications and other communication systems [39–47]. In view of this, a two-port

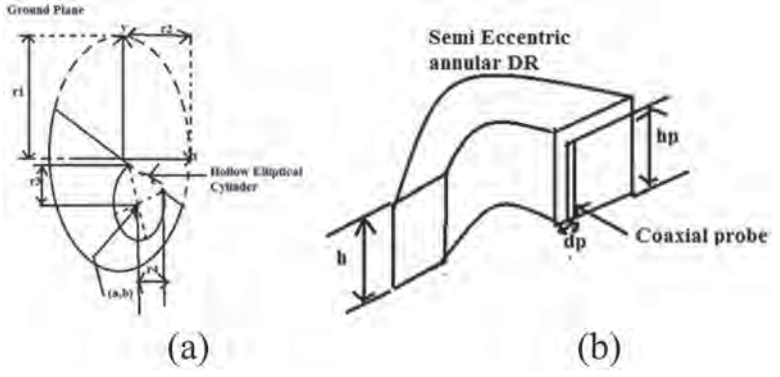

Figure 36. The proposed structure from reference [149]. (a) Two dimensional projection of the proposed geometry. (b) The perspective view of the geometry.

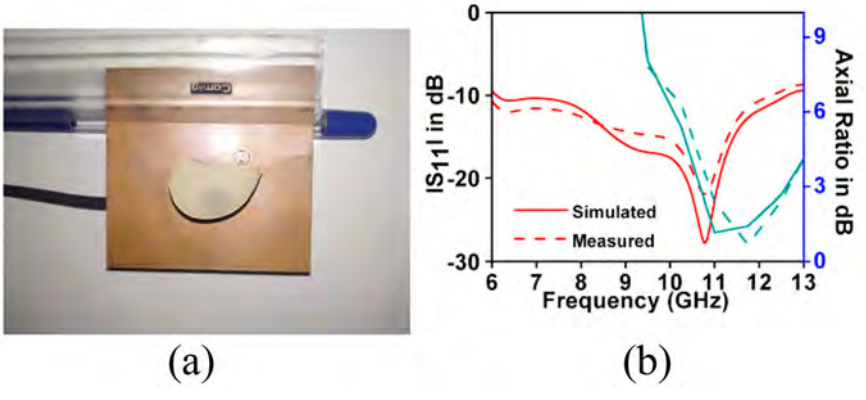

Figure 37. The configuration and results of reference [150]. (a) The fabricated prototype. (b) The axial ratio & $|S_{11}|$ plots against frequency.

dual-polarized omnidirectional design is proposed in [39] by exciting electric and magnetic dipole modes. The design uses single annular CDRA and two groups of four radially placed microstrip feed lines with different lengths to improve bandwidth of magnetic dipole mode which additionally suppresses higher order modes. Applications such as drone and aircraft prefer dual-polarized antennas with omnidirectional radiation patterns to avoid polarization mismatch at different flight altitudes. In [40], a new wideband compact EBG at 60 GHz is proposed to reduce the mutual coupling between CDRA elements. The targeted applications are compact antenna arrays, imaging radar systems and MIMO systems. A triple-band hybrid MIMO CDRA is presented in [41] at operating frequency of 6.4 GHz. Folded microstrip line excites the desired resonant mode with isolation of 10 dB. Further improvement in isolation upto 15 dB with an additional frequency band (2.6–2.78 GHz) is attained by etching two inverted L-shaped metallic strips in the ground plane. The potential applications are LTE2500, WLAN and WiMAX. In [42] a novel Frequency Selective Surface (FSS) based MIMO CDRA is proposed. The FSS structure has a Jerusalem cross, and an FAN structure. The isolation is improved upto 30 dB by combining both, FSS structure and slots on the ground plane. It should be noted that FSS is placed between DRAs to suppress surface

waves. The design is suitable for millimeter-wave MIMO systems in the frequency band, 57–63 GHz. Another MIMO CDRA design is presented in [43]. It is based on two linear arrays where each array is constructed by four CDRAs operating at 30 GHz. Passive microstrip feed network excites the proposed design. However, each array radiates in tilted fixed beam direction for low field correlation and isolation achieved is 25 dB. The application can be 5G communications or other short-range high-speed data links for handheld devices. In [44] a metamaterial polarization-rotator (MPR) wall improves the mutual coupling on average by more than 16 dB between two closely spaced CDRAs in the presented MIMO system. The other parameters such as radiation pattern, input impedance is unaltered after using MPR wall which is composed of 1×7 unit cells. The design is suitable for millimeter-wave applications in the frequency band 57–64 GHz. Similarly, in [45] by incorporating a metasurface consisting of 1×7 array of SRR unit cells between two CDRAs. It improves isolation upto 28 dB without significantly affecting antenna performance. The design is suitable for millimeter-wave applications in the frequency band 56.6–64.8 GHz. In [46], a two-element, four-port CDRA MIMO design is presented. The CDRAs are arranged back-to-back on a substrate in a unique manner which provides bi-directional diversity. The isolation is improved upto 18 dB by exciting orthogonal modes in opposite directions in each CDRA. The targeted applications are WLAN devices and terminals operating in the frequency band, 5.4–6 GHz. A dual-port two-element annular CDRA is proposed in [47]. U-shaped printed line is used for exciting the fundamental mode in CDRA and also, act as a radiator. This is the hybrid technique used for improving bandwidth. The isolation is improved upto 18 dB by using two L-shaped DGS and a rectangular-shaped DGS. The design operates in the frequency band, 3–7 GHz which makes it suitable for WiMAX (3.3–3.6 GHz) and WLAN (5.2–5.8 GHz) applications.

5. Review of the HDRA geometry

This section provides the details of various advances made in the hemispherical geometry of the HDRA. As has been stated that compared to the other conventional geometries, the HDRA offers a simpler transition to be solved numerically at the dielectric air interface. Yet, the HDRA fabrication, in comparison to the other conventional geometries is a bit challenging. A great amount of work in this direction has been done by the research group at City University of Hong Kong under K W Leung. The various sections have been organized to discuss the review of the research work carried out so far.

5.1. Wideband and circularly polarized HDRA geometries

The modal theory of the HDRA geometry has already been discussed in detail in Section 2.3. Further, the zero degree of freedom, offers a limitation on the capability to alter any dimension of the HDRA. This section discusses the different ways of improving the bandwidth of operation for an HDRA.

The analysis of the HDRA geometry has been deliberated using Green's function synthesis. This, as discussed, depends on the particular and the homogeneous solution. The detail of the Green's function formulation is discussed in [61–63,151–153]. Researchers in [154,155], propose the analytical solution for multilayered HDRA excited by aperture coupling. Based on the modes to be excited, the HDRA bandwidth can be improved by either

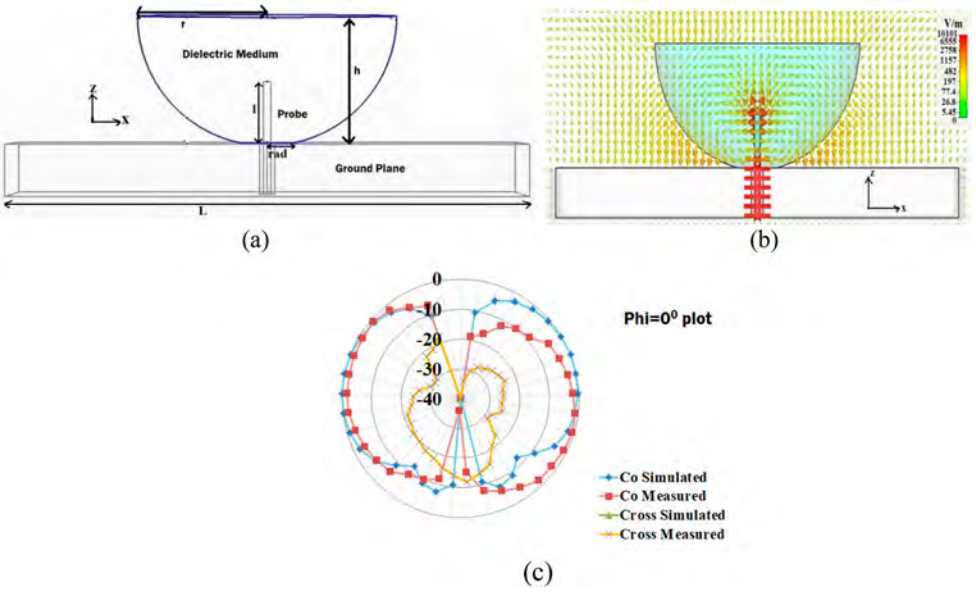

Figure 38. The geometry and its results from reference [64]. (a) The proposed geometry. (b) The electric field distribution for the TM_{101} like mode at 2.7 GHz. (c) The radiation pattern at 3.7 GHz for phi $= 0°$ plane.

mode-matching technique or impedance matching technique. In [64], the mode matching technique is used to achieve a wide bandwidth of frequency. The probe feed is used to excite the fundamental TM_{101} mode in the inverted HDRA. The TM_{101} mode has a null along the broadside direction of the far-field pattern and radiates like a short electric monopole antenna. The rationale to reduce the base area lies in the fact that as the base area reduces, the current which gets flushed away by the contact on ground plane reduces and more current gets coupled in the DRA. This leads to a high discontinuity at the dielectric air interface which reduces the Q factor, thus improving the bandwidth of operation. The proposed HDRA offers a bandwidth from 1.8 to 3.7 GHz. The peak gain is 4.5 dBi at 2.3 GHz. The proposed geometry is shown in Figure 38(a). The TM_{101} mode at 2.7 GHz is shown in Figure 38(b) using the plot of the vector electric field distribution and the radiation pattern for $\varphi = 0°$ at 3.5 GHz is shown in Figure 38(c).

In [156,157], the authors propose a new variation of quarter and half segmented HDRA for wideband applications. In segmented HDRA where four quarter sections are consolidated, two nearby modes are merged to offer a wider band width of operation. In this case [157], the $HEM_{11\delta}$-like mode and the TM_{101}-like modes are merged to offer bandwidth up to 30%. It is concluded that the quarter HDRA is much more compact than the conventional monopole antenna having its one-third impedance. The concept of merging the nearby modes can also be explained by the fact that for an HDRA, the input impedance is given as

$$\boldsymbol{Z_{in}} = \frac{-1}{\boldsymbol{I^2}} \iint_{\boldsymbol{S}} \boldsymbol{E_Z(r')J_Z(z)dS} \tag{35}$$

where E_z is the z directed electric field component due to the probe current J_z. The z-directed probe current J_z is the surface current flowing on the probe surface S. Also, $I_Z =$

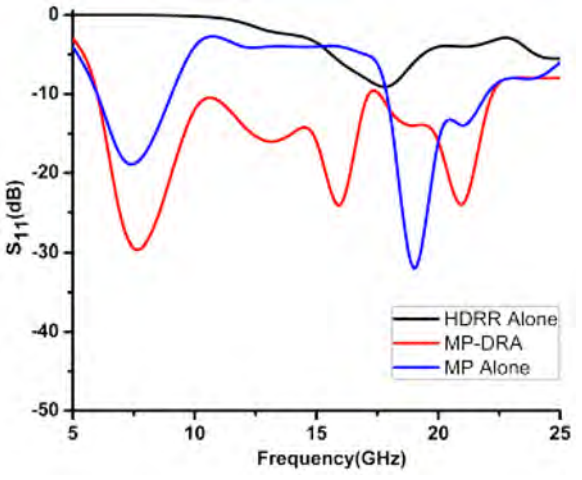

Figure 39. The proposed geometry as referred from [159]. The simulation results of the various cases of the reflection coefficients.

$2\pi r J_Z(z)$, where r is the radius of the HDRA. Thus, as the surface area decreases at the base area ground plane contact for the HDRA, input impedance decreases, which groups the closer modes, leading to wider bandwidth of operation.

In [158], a novel stacked HDRA made of acrylic and glass is investigated. The two-layered transparent HDRA supports the TM_{101} mode of operation which has omnidirectional characteristics. The outer layer has an average $\varepsilon_{r1} = 6.85$ of Glass and the inner acrylic layer has an average $\varepsilon_{r2} = 2.5$ for the frequency range of operation. The measured impedance bandwidth for such a structure is 14.2% (3.47–4 GHz). The complete characteristic equations are solved and the design details are presented to realize the proposed HDRA. In [159], a monopole loaded with HDRA structure is investigated for ultra-wideband (UWB) applications. The prototype is fabricated with $\varepsilon_r = 10$ material and the effect of a monopole, HDRA with center probe feed and an extended monopole is investigated. It is interesting to observe that a bandwidth of 126% is achieved with pattern stability of a monopole type radiation pattern and gain from 2 to 4 dBi is also observed. The simulated reflection coefficient is as shown in Figure 39. The figure clearly shows the comparison of the three proposed structures.

Researchers in [160] have proposed a detailed investigation on removing slots or sections from the HDRA and observed its effects on the bandwidth improvement. The most optimized geometry is observed for top slashed geometry. The rationale of the wide bandwidth observed is explained using Equation (35). As a part of the removal of the section of the HDRA, the net surface area increases, this decreases the input impedance as the current density operates on the increased surface area. This effect reduces the Q factor, thus improving the bandwidth of operation from 11.4% of the basic HDRA to 16.4% for the improved design. The proposed geometry investigated is as shown in Figure 40. The TE_{111} mode of operation is preserved during all investigations as the HDRA is excited by an offset coaxial probe feed. The resonant frequency of the proposed structure is approximately 2 GHz.

Another way inspected by researchers for improving the bandwidth is by creating Defected Ground Structure (DGS) on the ground plane. This has been proposed in [65,161].

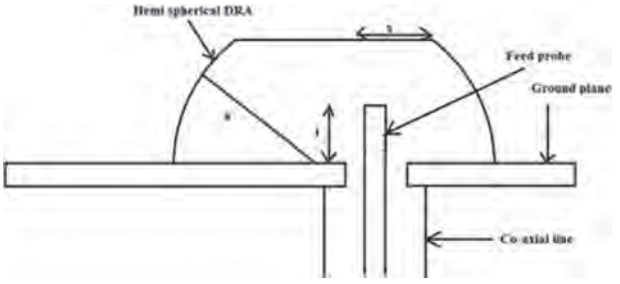

Figure 40. The proposed geometry as referred from [160].

In [161], three rectangular DGS are etched on the ground plane. The central DGS protrudes as a slot in the HDRA structure which reduces the effective permittivity of the material thus aiding in improving bandwidth. The rectangular DGS are spaced at a distance of d = 3.75 cm which is λ/4 distance at 2 GHz. The λ/4 distance modifies the current distribution by increasing the path length and also leads to effective current cancelation around the slot, reducing the cross-polar levels of the radiation pattern. This geometry offers a bandwidth of 23% at 2 GHz resonant frequency and a cross polar levels are 35 dB lower than the co-polar levels. As an extension, for effective cancelation of the currents in the ground plane, Complimentary Split Ring resonator (CSRR) is etched on the ground and the same is extended as a slot in the HDRA. The design procedure of the CSRR slots is explained in [65]. The CSRR induces currents in the opposite orientation around the slots and thus, leads to very efficient current cancelation, lowering the cross-polar levels to around 40 dB than the co-polar levels of the radiation pattern. The CSRR shaped slots protrudes through the HDRA thus, lowering down the effective permittivity and the Q factor. This leads to improved bandwidth. The dielectric material used for fabrication is Rogers TMM 10 with $\varepsilon_r = 9.2$. A bandwidth of 30% centered at 1.9 GHz is measured from the fabricated prototype. The proposed geometry offers a peak gain of 6 dBi.

The concept of slots is further extended in [162] for improving the bandwidth. A novel cheeseholes type HDRA is proposed where holes are drilled along all the three planes, i.e. *x-y*, *x-z* and the *y-z* planes. The holes are drilled at a distance of a fraction of λ/2 in order to achieve minimum Q factor because it ensures best cancelation of the EM waves inside the dielectric material. The resonant frequency is shifted to 2.53 GHz for the proposed structure due to lowering the effective permittivity of the material and the structure offers 25% impedance bandwidth. The peak gain observed is 6.2 dBi. Interestingly the TE_{111} mode of the HDRA remains preserved while the holes are drilled. The proposed structure and its simulated reflection coefficient are as shown in Figure 41(a) and (b) respectively.

On similar notes, CP has also been investigated on HDRAs. In [163], two conformal strips with 90° phase difference is used to excite the HDRA. This leads to generation of CP waves in the HDRA. Through this simple procedure more than 20% of the 3-dB axial ratio bandwidth is obtained. As an extension, authors in [164], propose a novel grounded microstrip patch to an aperture coupled HDRA. The parasitic patch generates an orthogonal field which when combines with the aperture coupled field generates CP waves. The CP frequency and axial ratio (AR) can easily be controlled by the patch location and patch size, respectively, with the impedance matched by varying the slot length and microstrip stub length. The

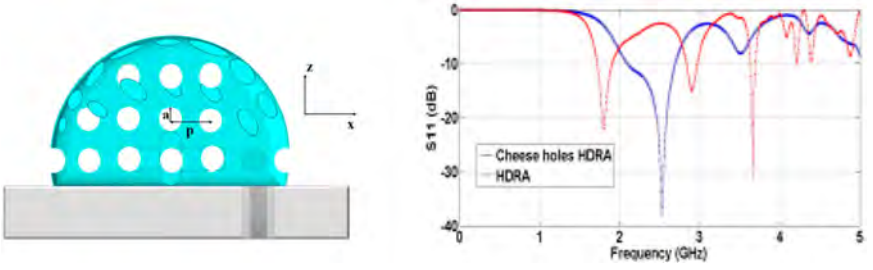

(a) (b)

Figure 41. The figures as referred from [162]. (a) The proposed structure. (b) The simulated reflection coefficient.

detailed analytical solution for the problem is also formulated and presented. The parasitic patch also acts as a frequency tuning element for the HDRA. A 3.4% 3-dB AR bandwidth is observed for the proposed structure.

5.2. Compact and high gain HDRA geometries

In the quest to find advancement for novel compact HDRA geometries, [165,166] propose wideband and compactness with a modified HDRA structure. In [165], a novel half HDRA with array of slots loaded with a monopole is proposed. The half HDRA offers a bandwidth of 0.96 GHz with a resonant frequency of 5.3 GHz. The peak gain offered is 7.2 dBi at 6.02 GHz. The array of slots is responsible to lower down the effective permittivity and the Q factor, thus increasing the bandwidth range. On the proposed HDRA structure, a circular metallic patch is loaded [166]. This metallic patch serves three important purposes. First, it acts as a reflector which improves the peak gain of the operating structure; second, the radius of the patch governs the frequency tuning capabilities of the proposed structure. Third, it aids in making the proposed structure compact. The patch is found to excite TM_{11}mode at 4.55 GHz and TM_{21} mode at 5.05 GHz. The proposed modified HDRA excites the TM_{101} mode of the HDRA. Because of the presence of the metallic patch, the peak gain observed is 8.5 dBi at 5.05 GHz. The proposed structure and the excited TM_{101}-like mode is as shown in Figure 42(a) and (b) respectively. From Figure 27(b), the role of the reflector from the metallic patch can be clearly seen.

In [167], a novel metallic capped inhomogeneous hybrid HDRA is investigated for ultra-wideband (UWB) applications. The proposed structure offers 170% bandwidth with an operational bandwidth ranging from 4.7 to 60 GHz. The presence of the metallic cap makes the structure compact. Similarly in [168], concept of sectored sections with successive fixed ratio of angle of sector and radius of the sector is proposed to achieve a compact and wideband HDRA response. The generation procedure of the proposed HDRA is as shown in Figure 43(a). It can be clearly seen that with each iteration, the sector angle and the radius of the sector follows a fixed ratio, thus, the volume of the sector constantly reduces. The fabricated prototype can be seen in Figure 43(b). The perturbation because of the staggered sectoring leads to a wide bandwidth response of 2.65 GHz. The resonant frequency is 4.16 GHz. The asymmetrical nature of the proposed structure also leads to generation of CP waves and it is found to be LHCP dominant. LHCP is observed from 4.2 to 5.3 GHz. The

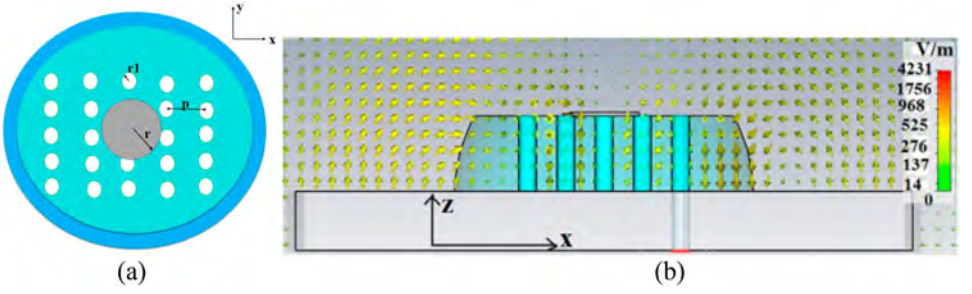

Figure 42. The proposed structure details as referred from [166]. (a) The proposed geometry. (b) The TM_{101}-like mode of the HDRA.

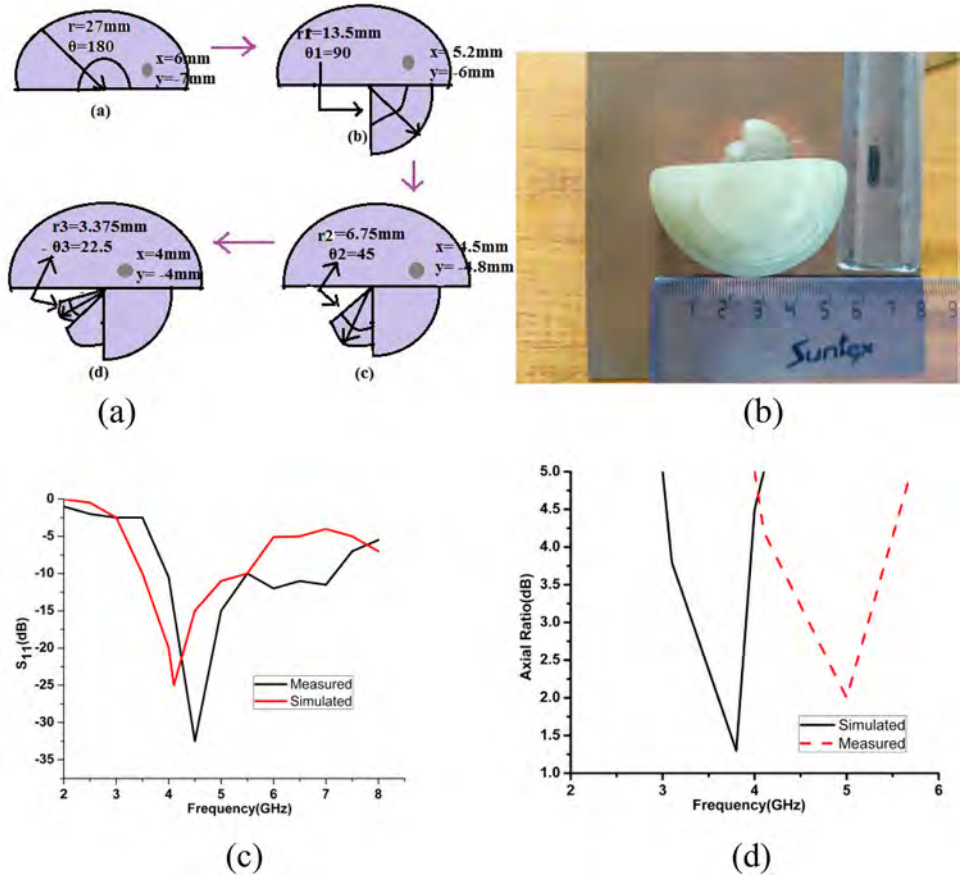

Figure 43. The figures as referred from [168]. (a) The generation procedure. (b) The fabricated prototype. (c) Reflection coefficient response. (d) 3-dB AR bandwidth response.

reflection coefficient response and the 3-dB AR bandwidth can be seen from Figure 43(c) and (d) respectively.

Further in [169], a monopole is loaded in adjacent by an HDRA. The detailed Green's function synthesis is carried out and the effect of the HDRA loaded on the monopole is

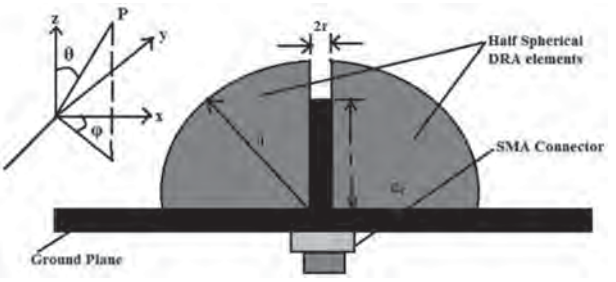

Figure 44. The proposed structure as referred from [170].

studied. The radiation pattern is found to be asymmetric in one plane and symmetric on the other. Also, the RADAR cross section (RCS) of the proposed structure is found to be quite small.

For improving the gain of the structure, two sections of the HDRA equally split, i.e. half HDRA are excited by a common probe which leads to a monopole type radiation pattern and a high gain. The proposed structure in [170] can be clearly seen from Figure 44.

A recent technique to improve the Peak gain of the DRAs is by loading an Electromagnetic Band Gap Structure (EBG) or metamaterial-based structures. This loading can be done in two ways either in the near field of the DRA or in the far field region of the DRA. The far-field of the antenna is characterized by a distance more than $2D^2/\lambda$, where D is the broadest dimension the DRA, and λ is the operating wavelength. If the EBG structure is loaded in the near-field region of the HDRA, it leads to increase in the effective aperture area of the HDRA and thus improves the Gain. While at the far-field region, the normal component of the radiated waves are coupled to increase directivity in free space, whereas the tangential fields induced on the EBG are canceled due to the presence of a band gap. This concept has been exploited in [171–174].

In [171], a hexagonal lattice hole type EBG material for the TE mode of operation is designed. For this a dielectric material of $\varepsilon_r = 2.81$ is chosen. The holes are drilled at an approximate distance of $\lambda/4$ so as to facilitate the maximum cancelation of the EM waves. As a consequence of loading the EBG on the HDRA, the TE_{111} mode of the HDRA is suppressed and the TM_{101} mode gets excited. The EBG has a bandgap from 1.75 to 2.25 GHz and the HDRA is resonant at 2 GHz. As a part of embedding the HDRA in the center of the EBG lattice, the bandwidth increases from 11.25% to 30% and the gain improves from 6.13 dBi to 9 dBi. The effect of the partial removal of dielectric material from the EBG and placement of the HDRA in that area, aids in increasing the discontinuity in the field lines, thereby reducing the overall Q factor of the antenna and thus, increasing the bandwidth. Further, a square lattice EBG is designed and loaded at a small height from the HDRA, however in the near field region to improve both Gain and impedance bandwidth. This is explored in [172]. The square lattice EBG is designed for TM modes and thus, the fundamental TE_{111} mode the HDRA remains unaltered. The effect of the EBG in the nearfield loading improves the bandwidth from 10.4% to 38% at 1.78 GHz and the peak gain from 6 dBi to 8.05 dBi at 1.95 GHz. The unit lattice of the EBG with its radius and the periodicity marked is as shown in Figure 45(a). The proposed structure is as shown in Figure 45(b) and the simulated reflection coefficient results are shown in Figure 45(c).

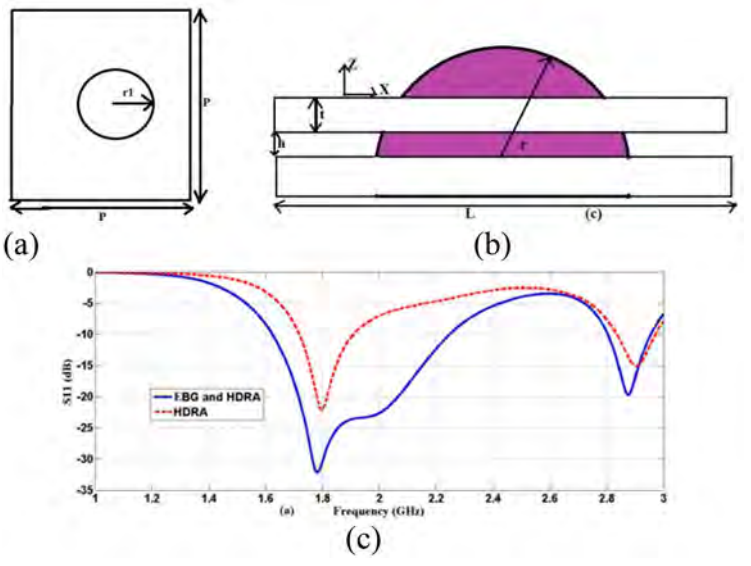

Figure 45. The proposed geometry and results as referred from [172]. (a) The unit cell of EBG proposed. (b) The proposed HDRA loaded with EBG. (c) Simulated Reflection coefficient results.

In order to improve the band gap response of the EBG, authors propose Sierpinski Carpet Fractal geometry for the arrangement of the holes. This novel EBG is placed on the HDRA and its investigation is carried out in [173,174]. Following a similar procedure, in [173], the HDRA is embedded in the novel fractal EBG. This improves the bandwidth from 10.4% of the HDRA to 21% with resonant frequency at 1.82 GHz. In [174], the height of the novel fractal EBG is raised. This increases the effective aperture and also lowers the Q factor. Interesting, the effect of raising the height improves the bandwidth from 10.4% to 63% at 1.42 GHz and also the peak gain improves from 6 dBi to 10 dBi at 2.05 GHz. A prototype is fabricated and the simulation results are experimentally verified.

For all EBGs it is well noted that the size of the EBG needs to be large enough to cancel the axial components of the fields. For smaller lattice size of the EBG, the cancelation of the EM waves is insufficient thus, lowering the gain of the antenna.

5.3. Novel techniques in HDRA

As has been mentioned in Section 2 (C), the transition of the dielectric air interface is smooth; researchers have found Green's function synthesis for various cases and geometries of the HDRA. The Green's function can be extended to calculate the farfield pattern of the HDRA as well. Researchers in [67,175–178] propose a Green's function for the coaxial probe fed HDRA under different configurations. In [175], the cross-polarization level of the radiation pattern is predicted using the mode-matching technique. Further, the detailed electric field component E_{cross} is also found. It is calculated by employing the fact that for a $\hat{z}$ directed current, the E_{cross} is given as follows:

$$E_{cross} = E_{\theta} sin\emptyset + E_{\emptyset} cos\emptyset \tag{36}$$

where θ and Φ represent the elevation and the azimuthal plane components.

In [67], the theoretical description of the coaxial probe fed HDRA is predicted. In this case, the TE and the TM modes excitation is clearly studied. The experimental verification of the proposed Green's function is also validated. As an extension, the center feed of HDRA which excites the TM_{101} mode is studied in [176]. Similarly, the axial feed HDRA is studied in [177]. After calculating the Green's function, the self and the mutual impedances of the cylindrical dipoles formed in the free space are also calculated. In [178], the input impedance of the coaxial probe excited HDRA is predicted. The experimental verification for an offset probe feed is also calculated.

In [179], the mutual impedance between two closely spaced HDRAs is calculated using Green's function. Since the probes excite the HDRA and so are not resonant themselves. This feature is exploited in the single mode excitation theory where the direct coupling between the probes is neglected as a consequence of it. In [180,181], the Green's function of the HDRA with an air gap and concentric conductor is calculated. This lays the foundation of analysis of any multilayer or stacked HDRAs which are rigorously investigated for wideband operation. Multiple layers lower down the effective permittivity and the Q factor which improves bandwidth of operation.

In [182,183], the aperture coupled HDRA is analyzed. While the aperture coupling is studied in [183], the reference [182] strictly confers to the understanding of the TE_{221} mode which has an end-fire radiation pattern. It is found that when the slot is aligned along the diameter of the HDRA, all TM modes are suppressed and the TE_{221} mode is strongly coupled to the HDRA. As a further enhancement to the analysis, authors in [184], employ the Volume Surface Integral equation (VSIE) with the dyadic Green's function for multilayer HDRAs with conformal patch placed on it. The effect of patch placed at different angles is also analyzed. In [185], a detailed formulation of Green's function for multilayer is carried out. The results of the theoretical investigation are also validated with experimental results from fabricated prototypes.

5.4. Multiple-input multiple-output (MIMO) and diversity HDRAs

As mention in the aforementioned RDRA and CDRA MIMO sections the advantages of MIMO technology are enormous such as high data rate but mutual coupling between multiple antennas forming MIMO system is a problem. In literature, HDRA designs are still not extensively studied for MIMO system due to difficulty in fabrication and bulky size. In view of this, a single HDRA based MIMO design is proposed at 4.9 GHz for WLAN applications [48]. The design consists of four elements HDRA and improves isolation upto 25 dB by exciting antennas from opposite side and providing offset to the feed.

6. Review of fractal investigation on DRAs

Fractal means a self-similar repetitive pattern. If a base element is repeated over a complete area, the geometry arising is termed as fractal. The fractal geometry on DRA extends a systematic, yet regular perturbation on the DRA which maximizes the surface area to volume ratio and thus reduces the Q factor, leading to improvement in bandwidth of operation. This stands in concurrence to Equation (34). In this section, a detailed survey on various fractal geometry investigations on the DRA structures is carried out.

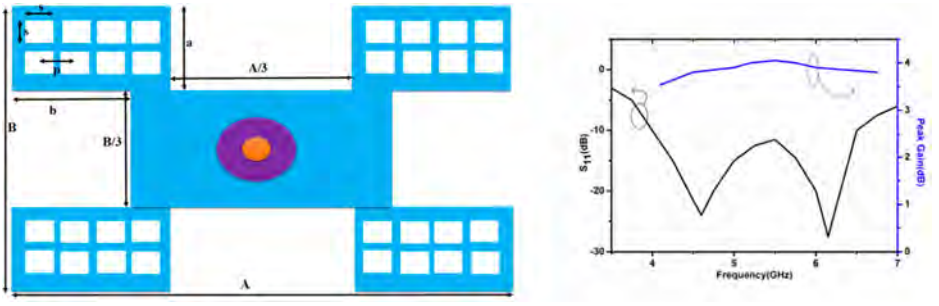

(a) (b)

Figure 46. The proposed perforated Minkowski geometry as referred from [188]. (a) The proposed structure. (b) The reflection coefficient simulation results.

6.1. Fractal geometry on RDRA structures

A popular method of Minkowski fractal is investigated in [186–190], for the RDRA geometries. In [186], experimental verification of Minkowski fractal on RDRA with co-planar waveguide slot feed is done. In the research, it is also found that compared to Sierpinski and Koch curves, minkowski on RDRA generates maximum bandwidth. The proposed antenna offers a fractional bandwidth of 64% (5.52 –10.72 GHz) and a broadside radiation pattern. At 6.96 GHz a peak gain of 4.9 dBi is observed. The permittivity of the material used for the DRA is $\varepsilon_r = 10$. The self-similar property of the fractal generates higher order modes in the proposed DRA. As an extension of the work, the authors in [187], propose a cross-slot coupling as a feed to the Minkowski fractal RDRA which generates the phase quadrature resulting in Circular Polarization. The structure yields a measured impedance bandwidth of 53% (4.71–8.10 GHz). The proposed structure is Left Hand Circularly Polarized (LHCP) dominant with a gain of 4.21 dB. In [188], the concept of perforations on the Minkowski fractal RDRA geometry is further extended to lower down the effective permittivity and thus the Q factor to increase the bandwidth. The antenna is excited by a probe fed at its center. This operates in quasi $TM_{01\delta}$ mode which is similar to the $TM_{01\delta}$ mode of CDRA. An impedance bandwidth of 2.48 GHz is obtained and the peak gain varies from 3.6 to 4.05 dBi in the matching band with maximum at 5.5 GHz. The proposed structure and its reflection coefficient results are as shown in Figure 46(a) and (b) respectively. The radiation pattern observed is omnidirectional in nature.

A similar modified fractal RDRA is also proposed in [189]. The proposed Fractal Rectangular Curve (FRC) with an offset probe feed and a central hole generates $TE^{y}_{1\delta1}$ mode of RDRA. As a consequence, for a material with $\varepsilon_r = 8$, an 18.44% bandwidth from 3.4056 to 4.831 GHz is obtained for a resonant frequency of 3.674 GHz. Further, a peak directivity of 6.009 dBi is also obtained. In [190], a novel Minkowski Half-hexagon Notched DRA (MHNDRA) is proposed to increase the surface area to volume ratio, bandwidth and operate at high-order modes to achieve higher gain. The proposed fractal RDRA offers a wide impedance bandwidth of 2.57 GHz at a resonant frequency of 4.8 GHz. Two modes have also been investigated which show the presence of both $TE^{z}_{21\delta}$ like and $TE^{z}_{22\delta}$ like modes. The peak gain of proposed antenna is 7.45dBi at 6.37 GHz. The proposed structure and its $|S_{11}|$ plot is as shown in Figure 47(a) and (b) respectively.

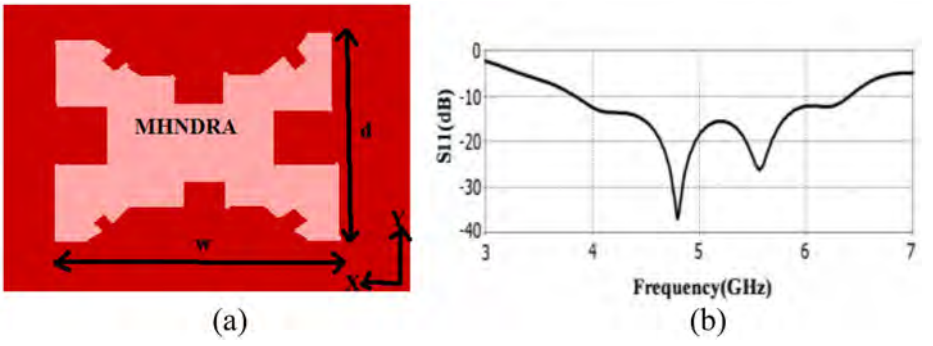

Figure 47. The MHNDRA as proposed in [190]. (a) The proposed geometry. (b) The Reflection coefficient plot.

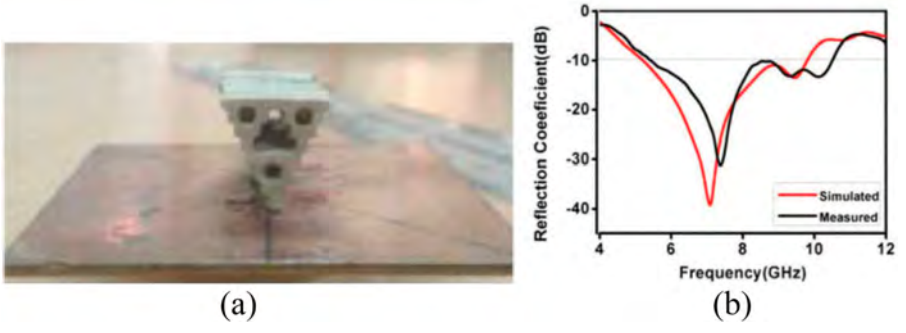

Figure 48. The Sierpinski fractal DRA as proposed in [192]. (a) The fabricated prototype. (b) The reflection coefficient plot.

In [191], slots in RDRA following the pattern of Sierpinski Carpet Fractal Geometry are proposed. Both rectangular and circular shaped holes are simulated. However, the circular-shaped slots based fractal DRA structure is fabricated and experimentally validated. The DRA material used is Teflon. The bandwidth offered is from 9 to 11.5 GHz and a peak gain of 7.5 dBi is also observed. In [192], Sierpinski fractal on RDRA is investigated. The inverted pyramid-shaped Sierpinski fractal DRA is found to be the best configuration amongst other proposed in the paper, in terms of bandwidth of operation and operating Gain. The structure offers 5.2 GHz bandwidth ranging from 5.3 to 10.5 GHz. The peak gain is 6.56 dBi at 10.1 GHz. The inverted geometry minimizes the base contact area of the dielectric material with the ground plane and so it offers the maximum bandwidth. The fabricated prototype and its reflection coefficient plot is shown in Figure 48(a) and (b) respectively.

In [193], Sierpinski fractal is employed with rotation to achieve CP. The proposed antenna consists of four rectangular dielectric layers; each one is rotated by an angle of 30° relative to its adjacent layers. Utilizing this type of approach produced a circular polarization over a bandwidth of 6.38% ranging from 9.67 to 10.3 GHz. The proposed fractal DRA has impedance bandwidth of 25.32% over the frequency range of X-band.

Interestingly in [53], dual fractal is implemented on a double segmented RDRA. Using Van Bladel approximation, where the field lines are symmetric about the plane, half of

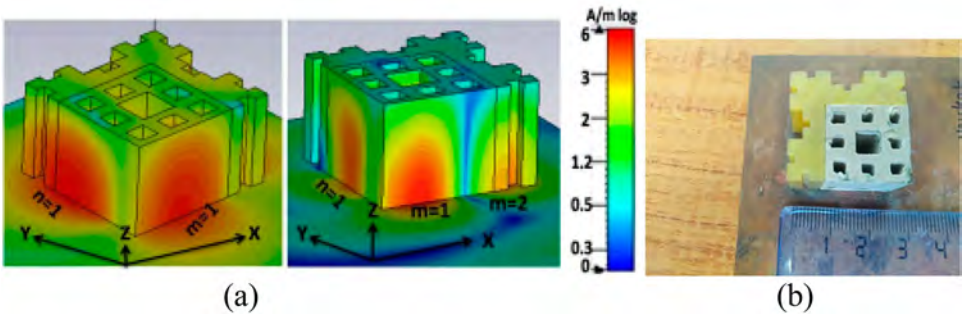

Figure 49. The dual fractal applied to RDRA from [53]. (a) The two modes identified using Scalar Magnetic Field distribution. (b) The fabricated prototype.

the material can be removed. Thus, a quarter of RDRA is obtained. This is subjected to Minkowski fractal for the outer material and the inner material is subjected to Sierpinski fractal. The bandwidth offered is 3.5–7.02 GHz (measured) and the peak gain is 6.74 dBi at 6.25 GHz. Two modes are also identified on the unperturbed surface of the fractal RDRA namely $TE^{z}_{11\delta}$ at 3.9 GHz and $TE^{z}_{21\delta}$ at 6.82 GHz. This is as shown in Figure 49(a). The fabricated prototype is as shown in Figure 49(b).

6.2. Fractal geometry on CDRA structures

In [194], Koch snowflake fractal geometry on a CDRA is designed and assessed up to two iterations. The proposed fractal DRA gives a wide impedance bandwidth of 56.5% at the fundamental resonant frequency of 3.6 GHz. Excitation of higher order $HE_{12\delta}$ like mode in the fractal geometry causes the radiation pattern to be broadside in nature. On applying fractal the peak gain improves from 5.3 to 6.9 dBi. Further extending and using the Van Bladel approximation, a compact Koch fractal ring CDRA is proposed in [195]. The proposed antenna offers a wide impedance bandwidth of 90% ranging from 4.7 GHz–12.4 GHz. The effect of the fractal geometry enhances the gain of DRA. The proposed antenna achieves radiation efficiency more than 78%, throughout the bandwidth. Interestingly, the proposed configuration reduces the DRA volume by 76.63% with reduced volume of 7.91 cm^3. The fabricated prototype and its reflection coefficient result are as shown in Figure 50(a) and (b) respectively. The shift in the resonant frequency of the fractal compared to the base CDRA is explained using the perturbation theory in electromagnetics.

In [196], novel fractal on CDRA is proposed for UWB applications. The proposed fractal CDRA is made by 30°, 60°, 120° angular portion of cylinder with radius ratio (1:2:3). This fractal geometry offers 9.2 GHz operating bandwidth which spans from 3.6 GHz–12.8 GHz. The proposed structure achieves peak gain of 9.45 dBi with more than 89% radiation efficiency. Hybrid Electromagnetic $HE_{11\delta}$, $HE_{12\delta}$ modes are identified at 4.43 GHz & 8.31 GHz resonant frequencies respectively.

In [197], half split CDRA based fractal structure is investigated. This novel fractal is termed as 'Tree-shaped fractal'. The first iteration provides bandwidth of 20% and the second iteration offers a bandwidth of 27% at 13 GHz. A constant gain of 5 dB is observed over entire range of frequency. The DRA is fabricated out of FR4 epoxy and is low cost. The proposed structure is shown in Figure 51.

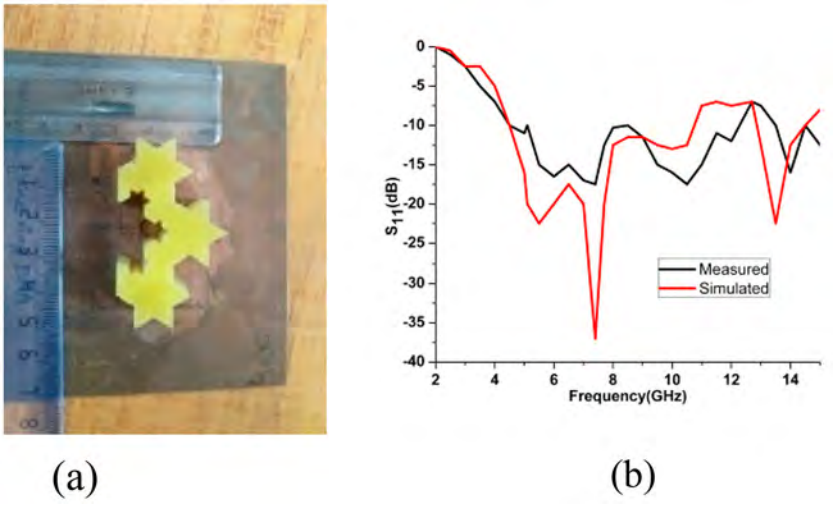

Figure 50. Compact Koch Snowflake Fractal CDRA from [195]. (a) The fabricated prototype. (b) The reflection coefficient results.

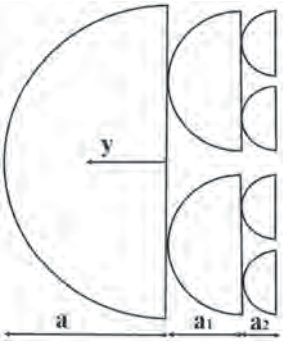

Figure 51. The proposed tree-shaped fractal as referred from [197].

In [198], Sierpinski Carpet fractal-based slots are created in CDRA to propose novel fractal geometry. The impedance bandwidth improves to 50% and the peak gain varies from 5.25 to 6.25 dBi. The proposed structure covers the X-band of application.

6.3. Fractal geometry on HDRA structures

Since HDRA offers zero degree of freedom compared to RDRA and CDRA, the radius of the Hemisphere is fixed corresponding to the resonant frequency. This lays a limitation in introducing a fractal concept on the HDRA. One method is to divide the radius into smaller sections such that the total radius of the base hemisphere remains constant. This concept has been executed by deploying Apollonian Gasket of circles on the HDRA which has been inspected in [199]. The apollonian gasket begins with three circles which are tangent to each other. Now, there are exactly two circles which are perfectly tangent to all the three circles designed in the initial step. One in the interior and second in the exterior. If any set of

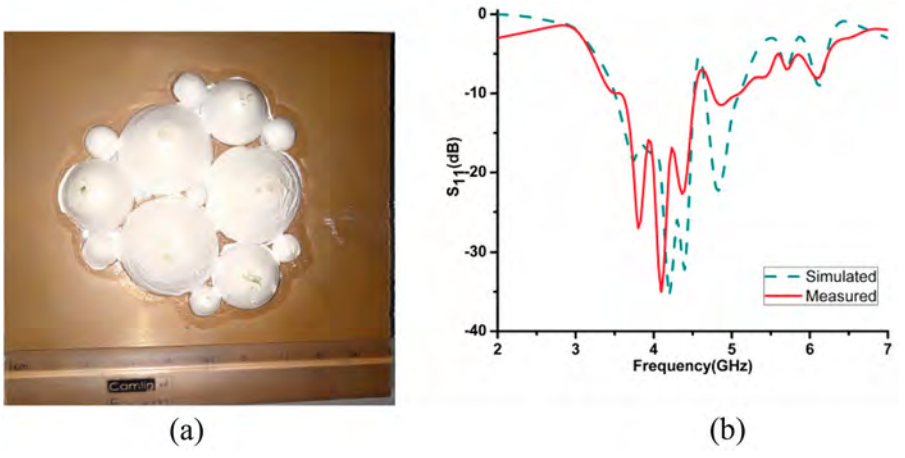

Figure 52. The proposed HDRA fractal of apollonian gasket as referred from [199]. (a) The fabricated third iteration fractal on HDRA. (b) The simulated and measured refection coefficient plots for third iteration.

three circles are chosen, a second iteration of new tangent circles can be drawn. Based on this concept, up to three iterations are experimentally validated on the HDRA. The third iteration fabricated proposed fractal structure is as shown Figure 52(a). The fractal geometry offers a wide impedance bandwidth of 1.68 GHz (47%) at a resonant frequency of 3.6 GHz. At the lower frequency band, TM_{101}-like mode is identified and so a null along the broadside direction is observed at 3.6 GHz. At the higher side of the frequency band, TE_{111}-like mode is identified and so a broadside radiation pattern is observed at 4.5 GHz. A peak gain of 8.7 dBi at 4.75 GHz is obtained in experimental measurements. The increase in resonant frequency is attributed to the fact that on applying the fractal, the dielectric material is distributed with every iteration, thus reducing effective dimensions of the antenna and increasing the resonant frequency of operation. Interestingly, the surface area and the volume calculation for infinite iteration of the fractal forms a convergent infinite series. The simulated and measured refection coefficient plot for the third iteration is shown in Figure 52(b).

In [200], quasi fractal geometry on HDRA is proposed. For a central HDRA, parasitic HDRAs are placed adjacent to it. The interaction of the DRAs of non-Euclidean geometry with radio waves is difficult to be described; hence further research to improve the geometry is ongoing. In [201], fractal is applied on a half HDRA structure. The combination of Minkowski fractal with a Geometric Progression is proposed. The simulated impedance bandwidth of the final iteration in Minkowski Fractal is 52.5%, i.e. 5.3 GHz to 9.1 GHz. In [202], Descarte's Circle Theorem is deployed on the HDRA to propose a novel fractal geometry. The proposed fractal is analyzed up to the second iteration. The fractal geometry offers a wide impedance bandwidth of 2 GHz, i.e. 41% at a resonant frequency of 3.6 GHz. The proposed antenna offers 80% efficiency with 8.6 dBi gain. Fundamental TE_{111}-like mode is observed at 4.3 GHz.

6.4. Novel fractal geometries based DRAs

One of the earliest investigations of Fractal on DRAs was studied in [203]. A detailed simulation study of various fractals like Koch, inverted Koch, etc. is done. It is observed that

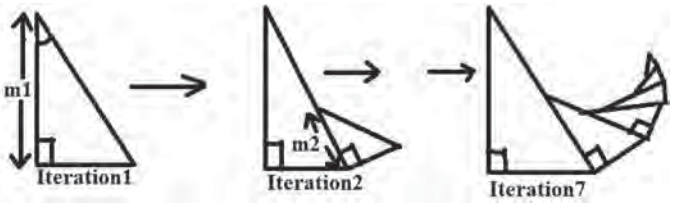

Figure 53. Spidron fractal DRA iterations as referred from [204].

for the third-order inverted Koch fractal DRA offers a bandwidth from 7.1 to 9.26 GHz. An interesting observation of the research is that in Koch Island fractal DRA a shift in resonant frequenciestoward longer wavelengths is observed when iteration order increases while in inverted Koch DRA, this effect is reversed.

In [204], a circularly polarized Spidron fractal DRA is presented. The spidron is created initially by a right-angled triangle, with an adjacent side of length$m_1$and angle $\alpha$is created, where α is the angle between the adjacent side and the hypotenuse of the triangle. The down scaling factor δ is given by Equation (37).

$$\delta = \frac{m_{n+1}}{m_n} = \tan(\alpha), \textit{where a varies from } 0^0 < \alpha < 45^0 \tag{37}$$

This spidron is excited by a *C* shaped slot responsible for generating CP. The experimental results prove that the proposed antenna has a bandwidth from 4.32 to 6.30 GHz and a 3-dB AR bandwidth of 11.57% (5.13–5.76 GHz). The measured gain of the antenna ranges 2.20 to 3.16 dBic within the AR bandwidth. The proposed fractal geometry is as shown in Figure 53.

Similarly in [205], a stacked fractal tetrahedron DRA is proposed. Triangular shaped slots are introduced in the tetrahedron DRA for UWB applications. 116.7% bandwidth covering frequency range from 3.5 to 13.3 GHz (entire C- and X-band) is achieved by simulations. A further extension of Sierpisnki fractal on Triangular DRA is investigated in [206]. This antenna has dual wide band over (6.39–7.60) GHz and (9.06–12.16) GHz which fall within C and X band of microwave frequency spectrum. Gain of the DRA is from 7 to 12 dB throughout the bands. A modification is proposed in [207], for dual broadband operations. Experimental results show a bandwidth from 2.25 to 2.60 GHz (14.46%) and 3.10–4.10 GHz (27.78%). Stable radiation patterns and gains of around 5.0dBi and 3.8dBi at 2.4 and 3.5 GHz respectively is observed.

In [208], a novel wideband Tree Shaped Fractal is proposed. Trapezoidal shaped conformal strip feed is used as feeding mechanism. Implementation of fractal geometry on DRA has been utilized to reduce Q-factor and subsequently achieve wide bandwidth. Tetrahedron shaped notches are created as fractal iterations to improve bandwidth. Impedance bandwidth of 86.32%, with frequency range from 4 to 10.1 GHz is achieved. Average gain of about 6 dBi over the entire band of interest is achieved.

A detailed comparison of the various applications of DRAs is tabulated in the following tables. Table 1 is a comparison of the various wideband applications based DRAs. The various techniques employed to improve the bandwidth is also mentioned in the table. Table 2 shows the comparison of various DRAs offering Circular Polarization. The method to obtain CP and the type of CP observed is also mentioned in the table. Table 3 compiles the various low profile and compact DRAs and the techniques to achieve them. Table 4

Table 1. Comparison of various wideband DRAs.

Ref	Basic geometry	ε_r	f_r	BW (GHz)	Feed type	Techniques and method	Gain	Mode	Polarization	Eff.
73	RDRA	10	14.7	∼ 15–17	Microstrip line	Multiple resonators	NM	NM	NM	NM
78	RDRA	25	6.9	∼ 6.7–8	Microstrip line	High aspect ratio	∼ 5	TE^{X}_{111}, TE^{X}_{112}, TE^{X}_{113}	NM	NM
79	RDRA	12	2.17	1.9–2.9	Microstrip slot	Two resonators	3–4	N.M.	N.M.	N.M.
80	RDRA	10.2	5	4.71–6.30	CPW	Two resonators	3.8	TE_{111}	NM	NM
25	CDRA	2.1	0.165	0.069–0.171	Coaxial probe	Resonator	NM	HEM_{11}	Vertical	40–74
27	CDRA	15.2	∼ 2.9	2.75–3.25	Coaxial probe	Resonator	NM	NM	NM	NM
29	CDRA	9.8	5.12	4.5–10.1	Coaxial probe	Multi resonator	7	$HEM_{11\delta}$	NM	75
31	CDRA	4.5	6	5.9–7.32/ 8.72–15	Microstrip Line	Two Resonator	12	$HEM_{01\delta}$	NM	NM
32	CDRA	10	∼ 3.4	3.25–3.65	Coaxial probe	Four Resonator	4	$HEM_{11\delta}$	NM	NM
33	CDRA	9.4	10.63	9.62–12.9	Microstrip Line	Two Resonator	8	TM_{110}/ $HEM_{11\delta}$ TM_{111} / $HEM_{12\delta}$	LP	NM
34	CDRA	10	8.0 21.5	1.95–10.5 6.6–23.6	Coaxial probe	Multi resonator	NM	TM_{01}	NM	NM
35	CDRA	9.8/16	∼ 4.1	3.14–5.56	Coaxial probe	One Resonator	8.7	$TM_{01\delta}$ $TM_{02\delta}$ $TM_{03\delta}$ $TM_{04\delta}$	NM	82
36	CDRA	6.85	3.98 4.25	3.75–5.37	Coaxial probe	DRA	NM	$HEM_{11\delta}$ $TM_{01\delta}$	NM	80
139	CDRA	10	2.4	1.6–3.2	Coaxial probe	DRA With Air Intrusion	7.25–8.61	$HEM_{11\delta}$	NM	NM
155	HDRA	1, 4, 9	4.88, 4.4	∼ 3.6–5.4	Coaxial probe	Multi-Layer	4.4–4.7	TE_{111}, TE_{112}	NM	NM
157	HDRA	10	3.5	∼ 3.0–4.2 ∼ 2.9–4.2	Coaxial probe	MULTI Element	2–2.5	TE_{111} TM_{101}	NM	NM
158	HDRA	2.2	3.59	2.87–3.96	Coaxial probe	TWO Layer	∼ 2.5	TM_{101}	NM	99
159	HDRA	10	6.813, 16, 20	5–21	Coaxialprobe	Conical DRA	2–4	TM_{101}	NM	NM
65	HDRA	9, 2	1.93.15	∼ 1.8–2.1	Coaxial probe	SHARE CSRR	6	TE_{111} TM_{101}	NM	90

Note: ε_r – permittivity, f_r – resonant frequency in GHz, BW-Bandwidth, Gain – in dBi, Eff. – Radiation efficiency.

Table 2. Comparison of various circularly polarized DRAs.

Ref	Basic geometry	ε_r	f_r	CP bandwidth (GHz)	BW(GHz)	Feed type	Techniques and method	Gain	Mode	Polarization	Eff.
103	RDRA	9.5	3.43	∼ 3.22–3.35	3.3–3.7	Aperture coupled	Parasitic patch	4.8	TE^{Y}_{111}	CP	NM
105	RDRA	10.2	4.1	3.4–5.75	3.4–5.9	Microstrip line	Conducting loops	3.6–6.6	N.M.	CP	78%
106	RDRA	2.0	2.87	∼ 3.3–3.5	750 MHz	Microstrip line	Notch	7	$TE_{11\delta}$	CP	NM
107	RDRA	10.8	14.75	14.35 - 14.80	14.35–14.80	Microstrip line	Aperture slot	NM	NM	NM	NM
108	RDRA	10.2	5.2	5.2- 6.5GHz	4.6–4.7	Microstrip line	Stair shaped patch	5.7	TE_{111}	CP	NM
128	CDRA	11.2	4.13	∼ 4.09–4.65	3.86–4.85	Coaxial probe	Helix	4.1	$HE_{11\delta}$	CP	NM
130	CDRA	4.4	2.45	2.399–2.484	2.35–2.510	Microstrip line	One resonator	2.7	NM	RHCP	NM
134	CDRA	9.8	4.3	4.2–4.55	3.37–5.69	Coaxial probe	Stacked dRA	5	NM	CP	NM
135	CDRA	12.8	4.7	4.4–6.67	4.1–6.81	Microstrip line	Multiple orthogonal mode	5	TE^{Y}_{111}	RHCP	80
136	CDRA	2.65/9.8	4.65	4.8–5.6	4.57–5.79	Microstrip line	Fractal DRA	4.3	$HE_{11\delta(2<\delta<3)}$	CP	NM
137	CDRA	10	7.4/ 4.3	NM	7.34–7.6/ 4.2–4.7	Microstrip line	Green function	10.3/ 6.5	$HEM_{12\delta}$/ $HEM_{11\delta}$	CP	NM
149	CDRA	10	10.6	10.37–10.98	9.41–12.62	Coaxial probe	Green function	4.17–4.78	NM	RHCP	NM
168	HDRA	4.3	4.16	4.2–5.3	3.3–5.9,	Coaxial Probe	Fractal approach	6.38	NM	CP(LHCP)	93
176	HDRA	9.5	3.6	NM	3.45–3.90	Coaxial Probe	Green function	NM	NM	CP	NM

Note: ε_r – permittivity, f_r – resonant frequency in GHz, BW-Bandwidth, Gain – in dBi, Eff. – Radiation efficiency.

Table 3. Comparison of various compact and low profile DRAs.

Ref	Basic geometry	ε_r	f_r	BW (GHz)	Feed type	Techniques and method	Gain	Mode	Polarization	Eff.
82	RDRA	93	7.5	7.18–7.91	Microstrip line	Multiple resonators	6.75	N.M.	N.M.	70
83	RDRA	100	7.72	7.7–7.8	Microsrip slot	Offset placement	N.M	N.M	N.M	N.M
85	RDRA	79	2	2.11–2.16	CPW	Open circuit	N.M	TE_{111}	N.M	N.M
86	RDRA	10.2	8.3	7.8–9.8	Microstrip stepped line	Metal patch	N.M	N.M	N.M	N.M
89	RDRA	9.2	3.2	3.1 - 10.6	Coaxial probe	Stacking and metal plate	7	N.M.	N.M.	N.M.
90	RDRA	12	0.911	0.99–1.1	Coaxial probe	Metal plate	NM	$HEM_{11\delta}$, $TE_{11\delta}$, and $TE_{01\delta}$	NM	NM
91	RDRA	12	0.918	1.15–1.35	Coaxial probe	Edge grounding	NM	NM	NM	NM
138	**CDRA**	6.85	1.8/ 2.4	1.71–1.88/ 2.4–2.48	Microstrip line	Strip and slot feed technique	6.67/ 8.36	HEM_{110}, HEM_{113}	NM.	75.6/ 99.9
148	CDRA	4.3	12.1	8.6–15.4	Coaxial probe	Staking of different segment of cylinder	15.65	NM	NM	70
166	HDRA	9.2	4.55	4.3–5.11	Coaxial probe	Perforated and loading a metallic patch	5.5	TM_{101}	N.M.	90

Note: ε_r – permittivity, f_r – resonant frequency in GHz, BW-Bandwidth, Gain – in dBi, Eff. – Radiation efficiency.

Table 4. Comparison of various high gain DRAs.

Ref	Basic geometry	ε_r	f_r	BW (GHz)	Feed type	Techniques and method	Gain	Mode	Polarization	Eff.
121	CDRA	10	5.8	5.4–6.8	Microstrip feed	PIN diode for Switching	11	$HEM_{11\delta}$	NM	NM
122	CDRA	4.3	5.8	6.68–5.84	Microstrip feed	Parabolic reflector	7.27	$HE_{21(1+\delta)}$	NM	86.1
123	CDRA	35.5	2.31	∼ 2.27–2.38	Coaxial probe	Circular periodic EBG	9.5	$HEM_{11\delta}$	NM	97
124	CDRA	6.15	5.8	5.72–5.87	Microstrip feed	Hybrid higher order mode	11.6	HEM_{133}, HEM_{123}	LP	90
140	CDRA	10.2	5	4.5 –10.5	Coaxial feed	differential feed arrangement	6.7	NM	NM	NM
126	CDRA	10.2	2.3/ 3.5/ 3.9/ 7.5/ 9.2	2.1–4.8/ 7.3–7.8/ 9.9–11	Coaxial probe	Conical Horn	**14.1**	$TM_{11\delta}$, $TM_{21\delta}$, and $TM_{31\delta}$	linear	80
171	HDRA	10.2	3.5	2.9–4.1	Coaxial feed	DRA array	4–5	NM	NM	NM

Note: ε_r – permittivity, f_r – resonant frequency in GHz, BW-Bandwidth, Gain – in dBi, Eff. – Radiation efficiency.

shows the comparison of various high gain DRA geometries which includes integration of DRA with horn antenna and metamaterials/EBG. Table 5 tabulates the various references of DRA for MIMO application and the isolation is clearly identified for each case. Table 6 shows the various Array geometries investigated in DRAs compared over the parameters of gain and bandwidth. Table 7 compares the various fractal geometries investigated on different

Table 5. Comparison of various MIMO DRAs.

Ref	Basic geometry	ε_r	f_r	Techniques and method	*Design Complexity*	*M*
9	RDRA	37	2.36	orthogonal modes	Low	N.M.
15	RDRA	10	1.8	two symmetric microstrip feed lines	Low	18
16	RDRA	NM	2.6	two parallel slits on the ground plane	Medium	~ 20
17	RDRA	10.2	5.3, 6.95, 9.56	trapezoidal patch	High	> 20
18	RDRA	10.2	8.76, 9.14	orthogonal feed network	High	20
19	RDRA	9.8	5.6	C-shaped DGS	High	15
20	RDRA	NM	~ 5	parallel strips and slits on ground plane	High	15
21	RDRA	9.8	3.45	EBG	High	26
22	RDRA	10	~ 3.7	Parasitic patch and diagonally positioned	High	28
39	CDRA	10	3.87	orthogonal modes	high	15
40	CDRA	10.2	60	EBG	high	13
41	CDRA	9.8	2.3, 2.85, 6.3	Dual L-shaped strips along with reflector	high	15, 33, 35
42	CDRA	10.2	~ 59	FSS and slots on ground plane	high	30
44	CDRA	10.2	~ 60	metamaterial polarization-rotator (MPR) wall	high	16
47	CDRA	9.8	3.8	two L-shaped DGS and a rectangular shaped DGS	high	18

Note: ε_r – permittivity, f_r – resonant frequency in GHz, M – Isolation in dB.

Table 6. Comparison of various DRA arrays.

Ref	Basic geometry	ε_r	f_r	BW (GHz)	Feed type	*Array Size*	Gain
115	RDRA	10.8	7.2	6.56–7.84	Microstrip line/aperture combination	2×2	11.3
4	RDRA	35.9	2.98 3.2	2.9–3.3	Dielectric Image Guide	1×7 5 elements cross coupled	11.14 10.1
6	RDRA	20	~ 5.7	6.12–7.43	Microstrip line	1×4	13.6

ε_r – permittivity, f_r – resonant frequency in GHz, BW-Bandwidth, Gain – in dBi.

Table 7. Comparison of various fractals applied on DRA.

Ref.	Basic geometry	Types of fractal	fr (GHz)	Band Width (GHz)	Gain (dBi)	Mode	Eff (%)	Polarization
186	RDRA	Minkowski	6.96, 8.56, 9.92	5.52–10.72	47.9	NM	NM	NM
189	RDRA	Fractal rectangular curve	2.128	2.07–2.38	5.99	NM	99.7	NM
190	RDRA	Minkowski	4.8	3.83–6.41	5.35	$TE_{21\delta}$, $TE_{22\delta}$	87	NM
191	RDRA	Sierpinski	9,10,11	9–11.5	7.5	NM	NM	NM
192	RDRA	Sierpinski	7.38	5.3–10.5	6.56	$TE_{21\delta}$	81	NM
195	CDRA	Koch	6	4.7–12.4	8.76	NM	78	NM
196	CDRA	Segment section	4.43, 8.31, 1030, 11.29	3.6–12.8	9.45	$HE_{12\delta}$ $HE_{11\delta}$, $HE_{41\delta}$, $TM_{11\delta}$	89	NM
199	HDRA	Apollonian Gasket of	3.6	~ 3.4–5.1	6.5,	TM_{101},	95	NM
201	HDRA	GP-Series Fractal and Minkowski Fractal	6.6	5.3–9.1	9.65	TE_{111}	94.7	NM
203	HDRA	Koch Island and inverted Koch Island	7.75	7.1–9.26	9.4	NM	NM	NM
204	Other shaped	Spidron Circles	5.3	4.32–6.3,5.13–5.76	2.2–3.16 8.5	NM TE_{111}	NM	LHCP

Note: f_r – resonant frequency in GHz, BW-Bandwidth, Gain – in dBi, Eff. – Radiation efficiency.

Table 8. Best cases of various DRA applications.

Ref	Application	Basic geometry	Frequency (GHz)	Band Width (GHz)	Gain (dBi)	Mode	Eff (%)
34	Wideband	CDRA	8.0 21.5	1.95–10.5 6.6–23.6	NM	TM_{01}	NM
126	High gain	CDRA	2.3/ 3.5/ 3.9/ 7.5/ 9.2	2.1–4.8/ 7.3–7.8/ 9.9–11	14.1	$TM_{11\delta}$, $TM_{21\delta}$, and $TM_{31\delta}$	80
138	Compact size	CDRA	1.8/ 2.4	1.71–1.88/ 2.4–2.48	6.67/ 8.36	HEM_{110}, HEM_{113}	75.6/ 99.9
135	Axial ratio band width	CDRA	4.7	4.4–6.67	5	$TE^{Y}{}_{111}$	80

conventional DRA shapes. The type of fractal implemented is also mentioned in the table. Table 8 tabulates the best cases reported in the literature for wide bandwidth, high gain, high isolation amongst MIMO DRAs and compact/low profile geometries.

7. Conclusion

This review paper provides a detailed walk through on the advancements in the fields of Dielectric Resonator Antennas. There are three basic geometries namely Rectangular DRA, Cylindrical DRA and Hemispherical DRA. This paper addresses the progress on all the basic geometries. A study on the different modes and the mode nomenclature is also discussed. Field patterns for the different modes as shown by different researchers are also presented. A detailed section on the investigation of fractal geometries on the DRAs is also presented to understand the effect of perturbation introduced by fractal geometries. The concepts on wideband, high gain, arrays, and circular polarization have been compiled. After each section a detailed comparison table to highlight the achievements of the research in that section has been tabulated.

Acknowledgements

The authors acknowledge the support of Ms. Monika Chauhan, Mr. Anil Rajput and Mr. Daniel Akhil of IIITDM Jabalpur for their help in organizing the review paper.

Disclosure statement

No potential conflict of interest was reported by the author(s).

Notes on contributors

Biswajeet Mukherjee received the B.Tech degree in ECE from Indraprastha University, Delhi, India, and the M.Tech. degree in microwave electronics from the Department of Electronic Science, University of Delhi, New Delhi, India, where he graduated as First Rank holder in the batch and the Ph.D. degree from IIT Bombay, Mumbai, India. He received the departmental fellowship during his M.Tech Program and also the Fellowship for Training of Young Scientist from MPCST, Government of Madhya Pradesh, India,for pursuing research in the field of DRAs and EBG. He is currently an Assistant Professor with the Department of Electronics and Communication Engineering, Indian Institute of Information Technology, Jabalpur, India. He has authored or co-authored more than 80 research articles in peer-reviewed journals and conferences. His current research interests include dielectric resonators,

antenna engineering, MIC, monolithic microwave integrated circuit, and computational electromagnetics in finite-difference time domain. Dr. Mukherjee was a recipient of the Young Scientist Award at URSI GASS 2014 and the IEI Young Engineering Award for 2016 in Electronics and Telecommunication Engineering Division. He has completed five research projects funded by various organizations. He is also the Senior Member of IEEE.

Pragati Patel received her B.Tech degree in Electronics and Communication Engineering from Uttar Pradesh Technical University, Ghaziabad, U.P, in 2008 and M.Tech degree in RF and Microwave Engineering from Indraprashta University, Delhi, in 2011. She has completed her Ph.D from Department of Electrical Engineering at Indian Institute of Technology, Mumbai, India in 2016. Her research interest includes the wireless power transmission (WPT), microstrip patch antennas and dielectric resonator antennas for wireless communications. She is currently working as Assistant Professor at National Institute of Technology, Goa. She is also Member of IEEE from 2013.

Jayanta Mukherjee received the Bachelor of Engineering degree in Electrical and Electronics Engineering from Birla Institute of Technology, Pilani, where he was awarded the gold medal on the basis of the order of merit. He later completed his M.S. and Ph.D from The State Ohio University. He is currently working as Professor in the Department of Electrical Engineering, Indian Institute of Technology, Bombay. Previously, he was a Texas Instruments Fellow during his Ph.D studies from 2001-2004. He has interned at Thomson Multimedia, Princetown, New Jersey during 2002-2003. He is a Senior Member of IEEE from 2013. His research interests include Antennas, RFIC design and Bio-medical VLSI circuits. He has authored and co-authored more than 135 research papers in Peer reviewed journals and conferences. He is also the author of three books on RF oscillators and antennas and has also handled several sponsored projects from various research agencies.

References

[1] Luk KM, Leung KW. Dielectric resonator antennas. England: Research Studies Press Ltd.; 2003.
[2] Petosa A. Dielectric resonator antenna Handbook. Norwood (MA): Artech House; 2007.
[3] Petosa A, Ittipiboon A. Dielectric resonator antennas: a historical review and the current State of the Art. IEEE Antenna Propag Mag. 2010;52(5):91–116.
[4] Ranjbar Nikkhah M, Rashed-Mohassel J, Kishk AA. High-gain aperture coupled rectangular dielectric resonator antenna array using parasitic elements. IEEE Trans Antennas Propag. 2013;61(7):3905–3908.
[5] Ashoor AZ, Ramahi OM. Dielectric resonator antenna arrays for microwave energy harvesting and far-field wireless power transfer. Prog Electromagnet Res C. 2015;59:89–99.
[6] Rana B, Parui SK. Microstrip line fed wideband circularly-polarized dielectric resonator antenna array for microwave image sensing. IEEE Sensors Lett. 2017;1(3):1–4.
[7] Li C, Chiu T. Single flip-chip packaged dielectric resonator antenna for CMOS terahertz antenna array gain enhancement. IEEE Access. 2019;7:7737–7746.
[8] Abdel-Wahab WM, Abdallah M, Anderson J, et al. SIW-integrated parasitic DRA array: analysis, design, and measurement. IEEE Antennas Wirel Propag Lett. Jan. 2019;18(1):69–73.
[9] Neshati MH, Wu Z. Investigation of rectangular dielectric resonator antennas for switching polarisation diversity communication systems. International Conference on Antennas and Propagation (ICAP); 2001; Manchester, UK; p. 99–102, vol. 1.
[10] Tian R, Plicanic V, Lau BK, et al. A compact six-port dielectric resonator antenna array: MIMO channel measurements and performance analysis. IEEE Trans Antennas Propag. 2010;58(4):1369–1379.
[11] Roslan SF, Kamarudin MR, Khalily M, et al. An MIMO rectangular dielectric resonator antenna for 4G applications. IEEE Antennas Wirel Propag Lett. 2014;13:321–324.
[12] Khan AA, Jamaluddin MH, Aqeel S, et al. Dual-band MIMO dielectric resonator antenna for WiMAX/WLAN applications. IET Microwaves, Antennas Propag. 2017;11(1):113–120.
[13] Das G, Sahu NK, Gangwar RK. Pattern diversity based double sided dielectric resonator antenna for mimo applications. IEEE Indian Conference on Antennas and Propogation (InCAP); 2018; Hyderabad, India; p. 1–4.

[14] Nadeem I, Choi D. Study on mutual coupling reduction technique for MIMO antennas. IEEE Access. 2019;7:563–586.
[15] Nasir J, Jamaluddin MH, Khalily M, et al. A reduced size dual port MIMO DRA with high isolation for 4G applications. Int J RF MicrowComput Aided Eng. 2015;25:495–501.
[16] Nasir J, Jamaluddin MH, Khalily M, et al. Design of an MIMO dielectric resonator antenna for 4G applications. Wireless Pers Commun. 2016;88:525–536.
[17] Sharma A, Biswas A. Wideband multiple-input–multiple-output dielectric resonator antenna. IET Microwaves, Antennas Propag. 2017;11(4):496–502.
[18] Abdalrazik A, El-Hameed ASA, Abdel-Rahman AB. A three-port MIMO dielectric resonator antenna using decoupled modes. IEEE Antennas Wirel Propag Lett. 2017;16:3104–3107.
[19] Trivedi K, Pujara D. Mutual coupling reduction in wideband tree shaped fractal dielectric resonator antenna array using defected ground structure for MIMO applications. Microw Opt Technol Lett. Nov. 2017;59(11):2735–2742.
[20] Singhwal SS, Kanaujia BK, Singh A, et al. Dual-port MIMO dielectric resonator antenna for WLAN applications. Int J RF Microwave Comput-Aided Eng. 2020;30(4):1–11. DOI:10.1002/mmce.22108.
[21] H. N. Chen, J. Song and J. Park, A compact circularly polarized MIMO dielectric resonator antenna over electromagnetic band-Gap surface for 5G applications. IEEE Access, vol. 7, pp. 140889–140898, 2019.
[22] Iqbal J, Illahi U, Sulaiman MI, et al. Mutual coupling reduction using hybrid technique in wideband circularly polarized MIMO antenna for WiMAX applications. IEEE Access. 2019;7:40951–40958.
[23] Pan YM, Qin X, Sun YX, et al. A simple decoupling method for 5G millimeter-wave MIMO dielectric resonator antennas. IEEE Trans Antennas Propag. April 2019;67(4):2224–2234.
[24] Zhang Y, Deng J, Li M, et al. A MIMO dielectric resonator antenna with improved isolation for 5G mm-wave applications. IEEE Antennas Wirel Propag Lett. April 2019;18(4):747–751.
[25] Qian Y, Chu Q. A broadband hybrid monopole-dielectric resonator water antenna. IEEE Antennas Wirel Propag Lett. 2017;16:360–363.
[26] Chaudhary RK, Srivastava KV, Biswas A. Two-layer embedded half-split cylindrical dielectric resonator antenna for wideband applications. 42nd IEEE European Microwave Conference (EuMC); 2012; p. 815–817.
[27] Walsh AG, DeYoung CS, Long SA. An investigation of stacked and embedded cylindrical dielectric resonator antennas. IEEE Antennas Wirel Propag Lett. 2006;5:130–133.
[28] Motevasselian A. Bandwidth enhancement of helix excited cylindrical dielectric resonator antennas by means of stacking. Loughborough Antennas & Propagation Conference (LAPC); 2012; Loughborough; p. 1–3.
[29] Dileep S, Kiran V, Mukherjee B. Laterally placed CDRA with triangular notches for ultra-wideband applications. Frequenz-J RF Eng Telecommun. 2018;72(1-2):73–78.
[30] Sharma A, Das G, Ranjan P, et al. Novel feeding mechanism to stimulate triple radiating modes in cylindrical dielectric resonator antenna. IEEE Access. 2016;4:9987–9992.
[31] Zebiri C-E, Lashab M, Sayad D, et al. Offset aperture-coupled double-cylinder dielectric resonator antenna with extended wideband. IEEE Trans Antennas Propag. 2017;65(10):5617–5622.
[32] Guha D, Antar YMM. Four-element cylindrical dielectric resonator antenna for wideband monopole-like radiation. IEEE Trans Antennas Propag. 2006;54(9):2657–2662.
[33] Majeed AH, Abdullah AS, Elmegri F, et al. Aperture-coupled asymmetric dielectric resonators antenna for wideband applications. IEEE Antennas Wirel Propag Lett. 2014;13:927–930.
[34] Ozzaim C. Monopole antenna loaded by a stepped-radius dielectric ring resonator for ultrawide bandwidth. IEEE Antennas Wirel Propag Lett. 2011;10:843–845.
[35] He Y, Lin Y, Deng C, et al. Annular column loaded cylindrical dielectric resonator antenna for wideband conical radiation. IEEE Trans Antennas Propag. 2015;63(12):5874–5878.
[36] Chen Z, Wong H. Wideband glass and liquid cylindrical dielectric resonator antenna for pattern reconfigurable design. IEEE Trans Antennas Propag. 2017;65(5):2157–2164.

[37] Chauhan M, Mukherjee B. Wideband circular polarized cylindrical segmented dielectric resonator antenna for ISM band applications. Int J RF and Microwave Comput-Aided Eng. 2020;30(4):1–10.
[38] Chauhan M, Pandey AK, Mukherjee B. A novel compact cylindrical dielectric resonator antenna for wireless sensor network application. IEEE Sensors Lett. 2018;2(2):1–4.
[39] Zou L, Abbott D, Fumeaux C. Omnidirectional cylindrical dielectric resonator antenna with dual polarization. IEEE Antennas Wirel Propag Lett. 2012;11:515–518.
[40] Al-Hasan MJ, Denidni TA, Sebak AR. Millimeter-wave compact EBG structure for mutual coupling reduction applications. IEEE Trans Antennas Propag. Feb. 2015;63(2):823–828.
[41] Sharma A, Das G, Gangwar RK. Dual polarized triple band hybrid MIMO cylindrical dielectric resonator antenna for LTE2500/WLAN/WiMAX applications. Int J RF MicrowComput-Aided Eng. 2016;26:763–772.
[42] Karimian R, Kesavan A, Nedil M, et al. Low-mutual-coupling 60-GHz MIMO antenna system with frequency selective surface wall. IEEE Antennas Wirel Propag Lett. 2017;16:373–376.
[43] Sharawi MS, Podilchak SK, Hussain MT, et al. Dielectric resonator based MIMO antenna system enabling millimetre-wave mobile devices. IET Microwaves, Antennas Propag. 2017;11(2): 287–293.
[44] Farahani M, Pourahmadazar J, Akbari M, et al. Mutual coupling reduction in millimeter-wave MIMO antenna array using a metamaterial polarization-rotator wall. IEEE Antennas Wirel Propag Lett. 2017;16:2324–2327.
[45] Dadgarpour A, Zarghooni B, Virdee BS, et al. Mutual coupling reduction in dielectric resonator antennas using metasurface Shield for 60-GHz MIMO systems. IEEE Antennas Wireless Propag Lett. 2017;16:477–480.
[46] Das G, Sharma A, Gangwar RK, et al. Compact back-to-back DRA-based four-port MIMO antenna system with bi-directional diversity. Electron Lett. 2018;54(14):884–886.
[47] Kumari T, Das G, Sharma A, et al. Design approach for dual element hybrid MIMO antenna arrangement for wideband applications. Int J RF Microw Comput-Aided Eng. 2019;29(1):1–10.
[48] Sarkar GA, Ballav S, Chatterje A, et al. Four element MIMO DRA with high isolation for WLAN applications. Prog Electromagnet Res Lett. 2019;84:99–106.
[49] Mongia RK, Ittipiboon A. Theoretical and experimental investigation rectangular dielectric resonator antennas. IEEE Trans Antennas Propag. 1997;45(9):1348–1356.
[50] Van Bladel J. On the resonances of a dielectric resonator of very high permittivity. IEEE Trans Microw Theory Tech. Feb. 1975;MTT-23:199–208.
[51] Okaya AK, Barash LF. The dielectric microwave resonator. Proceedings of IRE. 1962;50: 2081–2092.
[52] Zou M, Pan J. Investigation of resonant modes in wideband hybrid omni directional rectangular dielectric resonator antenna. IEEE Trans Antennas Propag. 2015;63(7):3272–3275.
[53] Kiran V, Dileep S, Mukherjee B. Compact embedded dual-element rectangular dielectric resonator antenna combining Sierpinski and Minkowski fractals. IEEE Trans Compon, Packag Manuf Technol. 2017;7(5):786–791.
[54] Sethares JC, Nauman J. Design of microwave dielectric resonators. IEEE Trans Microwave Theory & Tech. 1966;14(1):2–7.
[55] Verplanken M, Van Bladel J. The magnetic-dipole resonance of ring resonators of very high permittivity. IEEE Trans Microwave Theory & Tech. 1979;27(4):328–332.
[56] Kafez D, Guillon P. (eds.), Dielectric resonators. Dedham (MA): Artech House; 1986.
[57] Lehmus O, Ollikainen J, Vainikainen P. Characteristics of half-volume DRAs with different permittivities. IEEE Antennas Propag Soc Int Symp. 1999;1:22–25.
[58] Kajfez D, Glisson AW, James J. Computed modal field distributions for isolated dielectric resonators. IEEE Trans Microw Theory Tech. 1984;32(12):1609–1616.
[59] Guha D, Banerjee A, Kumar C, et al. Higher order mode excitation for high-gain broadside radiation from cylindrical dielectric resonator antennas. IEEE Trans Antennas Propag. 2012;60(1):71–77.

[60] Gajera H, Guha D, Kumar C. New technique of dielectric perturbation in dielectric resonator antenna to control the higher mode leading to reduced cross-polar radiations. IEEE Antenna Wireless Propag Lett. 2017;16:445–448.
[61] Kakade AB, Ghosh B. Efficient technique for the analysis of microstrip slot coupled hemispherical dielectric resonator antenna. IEEE Antennas Wirel Propag Lett. 2008;7:332–336.
[62] Kakade AB, Ghosh B. Mode excitation in the coaxial probe coupled three-layer hemispherical dielectric resonator antenna. IEEE Trans Antennas Propag. 2011;59:4463–4469.
[63] Bhattacharya D, Ghosh B, Goswami PK, et al. Evaluation of efficient Green's functions for spherically stratified media. IEEE Trans Antennas Propag. 2018;66:1613–1618.
[64] Mukherjee B, Patel P, Mukherjee J. A novel cup-shaped inverted hemispherical dielectric resonator antenna for wideband applications. IEEE Antenna Wireless Propag Lett. 2013;12:1240–1243.
[65] Mukherjee B, Patel P, Mukherjee J. A novel hemispherical dielectric resonator antenna with complimentary split rings shaped slots and resonator for wideband and low cross-polar applications. IEEE Antenna Propag Mag. 2015;57(1):120–128.
[66] Petosa A, Ittipiboon A, Thirakoune S. Perforated dielectric resonator antennas. IET Electron Lett. November 2002;38(24):1493–1495.
[67] Leung KW, Luk KM, Lai KYA, et al. Theory and experiment of a coaxial probe fed hemispherical dielectric resonator antenna. IEEE Trans Antennas Propag. 1993;41(10):1390–1398.
[68] Ghosh B, Ghosh K, Panda CS. Coplanar waveguide feedto the hemispherical DRA. IEEE Trans Antennas Propag. 2009;57(5):1566–1570.
[69] Wyville MW, Petosa A, Wight JS. DIG feed for DRA arrays. IEEE Antenna Propag Soc Int Symp (Digest). 2005;2A:176–179.
[70] Petosa A, Thirakounc A, Zuliani MS, et al. Comparison between planar arrays of perforated DRAs and microstrip patches. IEEE Antennas Propag Soc Int Symp. July 2005;2A:168–175.
[71] Cooper M, Petosa A, Ittipiboon A, et al. Investigation of dielectric resonator antennas for L-band communications. Symposium on Antenna Technology and Applied Electromagnetic Symposium, ANTEM 1996; 1996 August; Ottawa, Canada; p. 167–170.
[72] Almpanis G, Fumeaux C, Vahldieck R. Dual-mode bridge-shaped dielectric resonator antennas. IEEE Antennas Wirel Propag Lett. 2010;9:103–106.
[73] Petosa A, Simons N, Siushansian R, et al. Design and analysis of multisegment dielectric resonator antennas. IEEE Trans Antennas Propag. May 2000;48(5):738–742.
[74] Chauhan M, Mukherjee B. Investigation of T-shaped compact dielectric resonator antenna for wide band application. Radioelectron Commun Syst. 2019;62(11):594–603.
[75] Rashidian A, Forooraghi K, Aligodarz MT. Investigations on two segment dielectric resonator antennas. Microwave Opt Technol Lett. June 2005;45(6):533–537.
[76] Kshirsagar P, Gupta S, Mukherjee B. A two segment rectangular dielectric resonator antenna for ultra-wideband application. Electromagnetics. 2018;38(1):20–33.
[77] Young CSD, Long SA. Wideband cylindrical and rectangular dielectric resonator antennas. IEEE Antennas Wirel Propag Lett. 2006;5(1):426–429.
[78] Rashidian A, Klymyshyn DM. Microstrip fed high aspect ratio dielectric resonator antenna with dual resonance broadband characteristics. IETElectron Lett. 2009;45(2):94–95.
[79] Buerkle A, Sarabandi K, Mosallaei H. Compact slot and dielectric resonator antenna with dual-resonance, broadband characteristics. IEEE Trans Antennas Propag. 2005;53(3):1020–1027.
[80] Gao Y, Ooi BL, Ewe WB, et al. A compact wideband hybrid dielectric resonator antenna. IEEE Microwave Wireless Compon Lett. 2006;16(4):227–229.
[81] Kshirsagar P, Gupta S, Mukherjee B. Novel design of conformal-strip excited asymmetrical rectangular dielectric resonator antenna for ultra-wide band application. J Microwave Power Electromagn Energy. 2018;52(2):128–141.
[82] Liu Y, Liu H, Wei M, et al. A low-profile and high-permittivity dielectric resonator antenna with enhanced bandwidth. IEEE Antennas Wirel Propag Lett. 2015;14:791–794.
[83] Mongia RK, Cuhaci M. Low profile dielectric resonator antennas using a very high permittivity material. IETElectron Lett. 1994;30(17):1362–1363.

[84] Gong K, Hu XH. Low-profile substrate integrated dielectric resonator antenna implemented with PCB process. IEEE Antennas Wirel Propag Lett. 2014;13:1023–1026.
[85] Wu JY, Huang CY, Wong KL. Low profile very high permittivity dielectric resonator antenna excited by a coplanar waveguide. Microwave Opt Technol Lett. 1999;22(2):96–97.
[86] Saed M, Yadla R. Microstrip fed low profile and compact dielectric resonator antennas. Prog Electromagnet Res. 2006;56:151–162.
[87] Patel P, Mukherjee B, Mukherjee J. A compact wideband rectangular dielectric resonator antenna using perforations and edge grounding. IEEE Antenna Wireless Propag Lett. 2015;14:490–493.
[88] Patel P, Mukherjee B, Mukherjee J. New wideband quadrature rectangular dielectric resonator antenna. 45th IEEE European Microwave Conference (EuMC 2015); 2015; Paris, France.
[89] Ge Y, Esselle KP, Bird TS. Compact dielectric resonator antennas with ultrawide 60%–110% bandwidth. IEEE Trans Antennas Propag. 2011;59(9):3445–3448.
[90] O'Keefe SG, Kingsley SP, Saario S. FDTD simulation of radiation characteristics of half-volume HEM and TE-mode dielectric resonator antennas. IEEE Trans Antennas Propag. 2002;50(2):175–179.
[91] Tam MTK, Murch RD. Half volume dielectric resonator antenna designs. IETElectron Lett. 1997;33(23):1914–1916.
[92] Gao Y, Feng Z. Experimental investigation of new radiating mode in rectangular hybrid dielectric resonator antenna. IEEE Antennas Wirel Propag Lett. 2011;10:91–94.
[93] Khalily M, Rahim MKA, Kishk AA. Bandwidth enhancement and radiation characteristics improvement of rectangular dielectric resonator antenna. IEEE Antennas Wirel Propag Lett. 2011;10:393–395.
[94] Mongia RK. Reduced size metallized dielectric resonator antennas. IEEE Antennas Propag Soc Int Symp. 1997;4:2202–2205.
[95] Kishk AA, Huang W. Size-Reduction method for dielectric-resonator antennas. IEEE Antennas Propag Mag. 2011;53(2):26–38.
[96] Makwana GD, Vinoy KJ. Design of a compact rectangular dielectric resonator antenna at 2.4 GHz. Prog Electromagnet Res C. 2009;11:69–79.
[97] Rezaei P, Hakkak M, Forooraghi K. Design of wideband dielectric resonator antenna with a two segment structure. Prog Electromagnet Res. 2006;66:111–124.
[98] Sinha M, Killamsetty V, Mukherjee B. Near field analysis of RDRA loaded with split ring resonators Superstrate. Microwave Opt Technol Lett. 2018;60(2):472–478.
[99] Pandey AK, Chauhan M, Killamsetty V, et al. High gain compact rectangular dielectric resonator antenna using metamaterial as Superstrate. Int J RF Microwave Comput-Aided Eng. 2019;29(12):1–10. DOI:10.1002/mmce.21968.
[100] Huang CY, Wu JY, Wong KL. Cross-slot-coupled microstrip antenna and dielectric resonator antenna for circular polarization. IEEE Trans Antennas Propag. 1999;47(4):605–609.
[101] Chu LCY, Guha D, Antar YMM. Comb-shaped circularly polarized dielectric resonator antenna. IETElectron Lett. 2006;42(14):785–787.
[102] Zhang M, Li B, Lv X. Cross-slot-coupled wide dual-band circularly polarized rectangular dielectric resonator antenna. IEEE Antennas Wirel Propag Lett. 2014;13:532–535.
[103] Li B, Ng HK, Leung KW. A circularly polarized rectangular dielectric resonator antenna with a parasitic patch. IEEE Antennas Propag Soc Int Symp. 2004;1:1094–1097.
[104] Lim EH, Leung KW, Fang XS. The compact circularly-polarized hollow rectangular dielectric resonator antenna With an under laid quadrature coupler. IEEE Trans Antennas Propag. 2011;59(1):288–293.
[105] Khalily M, Rahim MKA, Kishk AA. Planar wideband circularly polarized antenna design with rectangular ring dielectric resonator and parasitic printed loops. IEEE Antennas Wirel Propag Lett. 2012;11:905–908.
[106] Deng SM, Tsai CL. A broadband slot-coupled circularly polarized rectangular notch dielectric resonator antenna fed by a microstrip line. IEEE Antennas Propag Soc Int Symp. 2005;4B:246–249.

[107] Esselle KP. Circularly polarized higher-order rectangular dielectric-resonator antenna. IET Electron Lett. 1996;32(3):150–151.
[108] Fakhte S, Oraizi H, Karimian R, et al. A new wideband circularly polarized stair-shaped dielectric resonator antenna. IEEE Trans Antennas Propag. 2015;63(4):1828–1832.
[109] Lu K, Leung KW, Pan YM. Theory and experiment of the hollow rectangular dielectric resonator antenna. IEEE Antennas Wirel Propag Lett. 2011;10:631–634.
[110] Fang X, Leung KW, Lim EH. Singly-fed dual-band circularly polarized dielectric resonator antenna. IEEE Antennas Wirel Propag Lett. 2014;13:995–998.
[111] Sulaiman MI, Khamas SK. A singly fed wideband circularly polarized dielectric resonator antenna using concentric open half-loops. IEEE Antennas Wirel Propag Lett. 2011;10:1305–1308.
[112] Li B, Hao C-X, Sheng X-Q. A dual-mode quadrature-fed wideband circularly polarized dielectric resonator antenna. IEEE Antennas Wirel Propag Lett. 2009;8:1036–1038.
[113] Khalily M, Kamarudin MR, Mokayef M, et al. A new wideband circularly polarized dielectric resonator antenna. Radioengineering. 2014;23(1):175–180.
[114] Patel P, Mukherjee B, Mukherjee J. Wideband circularly polarized rectangular dielectric resonator antenna using square shaped slots. IEEE Antenna Wireless Propag Lett. 2016;15:1309–1312.
[115] Loos GD, Antar YMM. A new aperture coupled rectangular dielectric resonator antenna array. Microwave Opt Technol Lett. 1994;7(6):642–644.
[116] Al-Zoubi AS, Kishk AA, Glisson AW. Aperture coupled rectangular dielectric resonator antenna array fed by dielectric image guide. IEEE Trans Antennas Propag. 2009;57(8):2252–2259.
[117] Dileep S, Kiran V, Mukherjee B. Compact bi-cone dielectric resonator antenna for ultra-wideband applications – a novel geometry explored. Electromagnetics. 2017;37(7):471–481.
[118] Babik GB, DiNallo C, Faraone A. Multimode dielectric resonator antenna of very highpermittivity. IEEE Antennas and Propagation Society International Symposium; 2004; Monterey, CA; p. 1383–1386.
[119] Feng K, Li N, Meng Q, et al. Study on dielectric resonator antenna with annular patch for high gain and large bandwidth. Chin J Electron. 2015;24(4):869–872.
[120] Wang Y, Denidni TA, Zeng Q, et al. Design of high gain, broadband cylindrical dielectric resonator antenna. IET Electron Lett. 2013;49(24):1506–1507.
[121] Zhong L, Hong J, Zhou H. A novel pattern-reconfigurable cylindrical dielectric resonator antenna with enhanced gain. IEEE Antennas Wirel Propag Lett. 2016;15:1253–1256.
[122] Ali SM, Zakariya MA, Baharudin Z, et al. Parabolic reflector fed by cylindrical dielectric resonator antenna with high gain. 5th International Conference on Intelligent and Advanced Systems (ICIAS); 2014; Kuala Lumpur; p. 1–6.
[123] Denidni TA, Coulibaly Y, Boutayeb H. Hybrid dielectric resonator antenna With circular mushroom-like structure for gain improvement. IEEE Trans Antennas Propag. 2009;57(4):1043–1049.
[124] Mrnka M, Raida Z. Enhanced-Gain dielectric resonator antenna based on the combination of higher-order modes. IEEE Antennas Wirel Propag Lett. 2016;15:710–713.
[125] Ren J, Jiang W, Zhang K, et al. A high-gain circularly polarized Fabry–perot antenna with wideband Low-RCS property. IEEE Antennas Wirel Propag Lett. 2018;17(5):853–856.
[126] Chauhan M, Mukherjee B. High gain cylindrical dielectric resonator integrated with horn for multiband wireless applications. Int J RF Microwave Comput-Aided Eng. 2020. Early View. DOI:10.1002/mmce.22161.
[127] Chowdhury R, Muzammil Sani M, Chaudhary RK. A broadside circularly polarized semi-cylindrical dielectric resonator antenna excited with unequal pair of vertical microstrip line. Progress in Electromagnetics Research Symposium — Fall (PIERS — FALL); 2017; Singapore.
[128] Motevasselian A, Ellgardt A, Jonsson BLG. A helix excited circularly polarized hollow cylindrical dielectric resonator antenna. IEEE Antennas Wirel Propag Lett. 2013;12:535–538.
[129] Ren J, Guo L, Leung KW. Wideband circularly polarized cylindrical dielectric resonator antenna. IEEE International Symposium on Antennas and Propagation & USNC/URSI National Radio Science Meeting; 2017; San Diego, CA, p. 1531–1532.

[130] Lin C, Sun J. Circularly polarized dielectric resonator antenna fed by off-centered microstrip line for 2.4-GHz ISM band applications. IEEE Antennas Wirel Propag Lett. 2015;14:947–949.
[131] Tam MTK, Murch RD. Circularly polarized circular sector dielectric resonator antenna. IEEE Trans Antennas Propag. 2000;48(1):126–128.
[132] Sun R-Y, Chen Q-H. Quadrature feed wideband circularlypolarized cylindrical dielectric resonator antenna. J Electromagnet Waves Appl. 2014;28(8):1011–1017.
[133] Sharma A, Gangwar RK. Compact tribandcylindrical dielectric resonator antenna with circular slots for wireless application. J Electromagnet Waves Appl. 2016;33(3):331–340.
[134] Chowdhury R, Chaudhary RK. An approach to generate circular polarization in a modified cylindrical-shaped dielectric resonator antenna using PMC boundary approximation. IEEE Antennas Wirel Propag Lett. 2018;17(9):1727–1731.
[135] Varshney G, Pandey VS, Yaduvanshi RS, et al. Wide band circularly polarized dielectric resonator antenna with stair-shaped slot excitation. IEEE Trans Antennas Propag. 2017;65(3):1380–1383.
[136] Zhou Y, Jiao Y, Weng Z, et al. A novel single-fed wide dual-band circularly polarized dielectric resonator antenna. IEEE Antennas Wirel Propag Lett. 2016;15:930–933.
[137] Gupta P, Guha D, Kumar C. Dielectric resonator working as feed as well as antenna: new concept for dual-mode dual-band improved design. IEEE Trans Antennas Propag. 2016;64(4):1497–1502.
[138] Sun YX, Leung KW. Dual-Band and wideband dual-polarized cylindrical dielectric resonator antennas. IEEE Antennas Wirel Propag Lett. 2013;12:384–387.
[139] Chu LCY, Guha D, Antar YMM. Conformal strip-fed shaped cylindrical dielectric resonator: improved design of a wideband wireless antenna. IEEE Antennas Wirel Propag Lett. 2009;8:482–485.
[140] Singh A, Sharma SK. Investigations on wideband cylindrical dielectric resonator antenna with directive radiation patterns and low cross polarization. IEEE Trans Antennas Propag. 2010;58(5):1779–1783.
[141] Kshirsagar P, Gupta S, Mukherjee B. Cylindrical dielectric resonator antenna with perpendicular slots — A novel geometry explored. 11th International Conference on Industrial and Information Systems (ICIIS); 2016; Roorkee; p. 710–714.
[142] Guha D, Gajera H, Kumar C. Cross-polarized radiation in a cylindrical dielectric resonator antenna: identification of source, experimental proof, and its suppression. IEEE Trans Antennas Propag. 2015;63(4):1863–1867.
[143] Guha D, Banerjee A, Kumar C, et al. Design guidelines for the cylindrical dielectric resonator antenna using the Recently proposed HEM12d mode [antenna designer's notebook]. IEEE Antennas Propag Mag. 2014;56(4):148–158.
[144] Guha D, Banerjee A, Kumar C, et al. New technique to excite higher-order radiating mode in a cylindrical dielectric resonator antenna. IEEE Antennas Wirel Propag Lett. 2014;13:15–18.
[145] Das G, Sahu NK, Sharma A, et al. Wideband MIMO hybrid cylindrical dielectric resonator antenna with improved diversity performance. IEEE Conference on Antenna Measurements & Applications (CAMA); 2017; Tsukuba; p. 217–220.
[146] Seko MH, Correra FS. Excitation of dielectric resonator antennas by loop coupling. IEEE Antennas Wirel Propag Lett. 2019;18(4):656–658.
[147] Chauhan M, Rajput A, Mukherjee B. 2019. Multiband corrugated plus shaped inverted half cylindrical dielectric resonator antenna for numerous wireless applications. 13th IEEE European Conference on Antennas and Propagation (EuCAP); 2019; Krakow, Poland; p. 1–5.
[148] Gupta S, Kshirsagar P, Mukherjee B. Low profile multilayer cylindrical segment fractal dielectric resonator antenna for wideband applications. IEEE Antenna Propag Mag. 2019;61(4):55–63.
[149] Lee JM, Kim S-J, Kwon G, et al. Circularly polarized semi-eccentric annular dielectric resonator antenna for X-band applications. IEEE Antenna Wireless Propag Lett. 2015;14:1810–1813.
[150] Chauhan M, Pandey AK, Mukherjee B. A novel cylindrical dielectric resonator antenna based on Fibonacci series approach. Microwave Opt Technol Lett. 2019;61(10):2268–2274.
[151] Kishk AA, Zhou G, Glisson AW. Analysis of dielectric-resonator antennas with emphasis on hemispherical structures. IEEE Antennas Propag Mag. 1994;36(2):20–31.

[152] Leung KW. Analysis of aperture-coupled hemispherical dielectric resonator antenna with a perpendicular feed. IEEE Trans Antennas Propag. 2000;48(6):1005–1007.
[153] Leung KW. Complex resonance and radiation of hemispherical dielectric-resonator antenna with a concentric conductor. IEEE Trans Microw Theory Tech. 2001;49(3):524–531.
[154] Leung KW, So KK. Theory and experiment of the wideband two-layer hemispherical dielectric resonator antenna. IEEE Trans Antennas Propag. 2009;57(4):1280–1284.
[155] Ghosh B, Kakade AB. Mode excitation in the microstrip slot-coupled three-layer hemispherical dielectric resonator antenna. IET Microwaves, Antennas Propag. 2016;10(14):1534–1540.
[156] Guha D, Antar YMM. New half-hemispherical dielectric resonator antenna for broadband monopole-type radiation. IEEE Trans Antennas Propag. 2006;54(12):3621–3628.
[157] Guha D, Gupta B, Kumar C, et al. Segmented hemispherical DRA: new geometry characterized and investigated in multi-element composite forms for wideband antenna applications. IEEE Trans Antennas Propag. 2012;60(3):1605–1610.
[158] Fang XS, Leung KW. Design of wideband omnidirectional two-layer transparent hemispherical dielectric resonator antenna. IEEE Trans Antennas Propag. 2014;62(10):5353–5357.
[159] Guha D, Gupta B, Antar YMM. Hybrid monopole-DRAs using hemispherical/ conical-shaped dielectric ring resonators: improved ultrawide band designs. IEEE Trans Antennas Propag. 2012;60(1):393–398.
[160] Mukherjee B, Raj A. Investigation of a hemispherical dielectric resonator antenna for enhanced bandwidth of operation. Int J Appl Electromagnet Mech. 2013;41(4):457–466.
[161] Mukherjee B, Patel P, Mukherjee J. A novel hemispherical dielectric resonator antenna with rectangular slot and defected ground structure for low cross polar and wideband applications. 10th IEEE INDICON; 2013; Mumbai, India.
[162] Mukherjee B, Patel P, Mukherjee J. A novel cheeseholes type hemispherical dielectric resonator antenna for wireless applications. 43rd IEEE European Microwave Conference (EuMC); 2013; Nuremberg, Germany; p. 1711–1714.
[163] Ng HK, Leung KW. Circular-polarized hemispherical dielectric resonator antenna excited by dual conformal-strip. IEEE Antennas and Propagation Society International Symposium (IEEE Cat. No.02CH37313); 2002; San Antonio, TX, USA, p. 442–445.
[164] Leung KW, Ng HK. The slot-coupled hemispherical dielectric resonator antenna with a parasitic patch: applications to the circularly polarized antenna and wide-band antenna. IEEE Trans Antennas Propag. 2005;53(5):1762–1769.
[165] Mukherjee B, Patel P, Reddy GS, et al. A novel half hemispherical dielectric resonator antenna with array of slots for wideband applications. Prog Electromagnet Res C (PIER-C. 2013;36:207–221.
[166] Mukherjee B. A novel half hemispherical dielectric resonator antenna with array of slots loaded with a circular metallic patch for wireless applications. AEU – Int J Electron Commun. 2015;69:1755–1759.
[167] Arora S, Shaik LA, Saha C, et al. Metallic capped hybrid inhomogeneous hemispherical dielectric resonator antenna for enhanced operational bandwidth. IEEE Applied Electromagnetics Conference (AEMC); 2015; Guwahati; p. 1–2.
[168] Gupta S, Killamsetty V, Chauhan M, et al. Compact and circularly polarized hemispherical DRA for C-band applications. Frequenz: J RF Eng Telecommun. 2019;73(7-8):227–234.
[169] Tse KK, Leung KW, Luk KM, et al. A monopole antenna loaded by a hemispherical dielectric resonator. IEEE Trans Antennas Propag. 2003;51(3):413–420.
[170] Guha D, Antar YMM. Half hemispherical DRA array for very large bandwidth high gain and monopole-like radiation pattern. IEEE Antennas and Propagation Society International Symposium; 2005; Washington, DC; p. 462–465.
[171] Mukherjee B, Kumar D, Gupta M. A novel hemispherical dielectric resonator antenna on an electromagnetic band Gap substrate for broadband and high gain systems. AEU – Int J Electron Commun. 2014;68:1185–1190.
[172] Mukherjee B, Patel P, Mukherjee J. Hemispherical dielectric resonator antenna loaded with a photonic band gap structure for wideband and high gain applications. 31st URSI General Assembly and Scientific Symposium URSI-GASS; 2014; Beijing, China.

[173] Mukherjee B, Patel P, Mukherjee J. Hemispherical dielectric resonator antenna embedded in a novel Sierpinski carpet fractal based photonic band gap structure for wideband systems. 3rd IEEE Asia Pacific Conference on Antennas and Propagation (APCAP); 2014; Harbin, China; p. 147–150.
[174] Mukherjee B, Patel P, Mukherjee J. hemispherical dielectric resonator antenna loaded with a novel Sierpinski carpet fractal based photonic band gap structure for wireless applications. 26th IEEE Asia Pacific Microwave Conference (APMC); 2014; Sendai, Japan; p. 1279–1281.
[175] Leung KW, Tse KK, Luk KM, et al. Cross-polarization characteristics of a probe-fed hemispherical dielectric resonator antenna. IEEE Trans Antennas Propag. 1999;47(7):1228–1230.
[176] Leung KW, Ng KW, Luk KM, et al. Simple formula for analyzing the centre-fed hemispherical dielectric resonator antenna. Electron Lett. 1997;33(6):440–441.
[177] Leung KW, Ng KW, Luk KM, et al. On the efficient calculation of the axially probe-fed hemispherical dielectric resonator antenna. IEEE Antennas and Propagation Society International Symposium; 1997; Digest, Montreal, Quebec, Canada; p. 2084–2087.
[178] Zhou G, Kishk AA, Glisson AW. Input impedance of a hemispherical dielectric resonator antenna excited by a coaxial probe. Proceedings of IEEE Antennas and Propagation Society International Symposium; 1993; Ann Arbor, MI, USA; p. 1038–1041.
[179] Luk K-M, Leung W-K, Leung K-W. Mutual impedance of hemispherical dielectric resonator antennas. IEEE Trans Antennas Propag. 1994;42(12):1652–1654.
[180] Wong K, Chen N, Chen H. Analysis of a hemispherical dielectric resonator antenna with an airgap. IEEE Microwave Guided Wave Lett. 1993;3(10):355–357.
[181] Luk KM, Leung KW, Yung EKN. Hemispherical dielectric resonator antenna with a concentric conductor. IEEE Antennas and Propagation Society International Symposium; 1995; Digest, Newport Beach, CA. USA; p. 730–733.
[182] Leung KW, Lai KYA, Luk KM, et al. End-fire TE/sub 221/ mode of aperture coupled hemispherical dielectric resonator antenna. Electron Lett. 1993;29(11):981–982.
[183] Leung K-W, Luk K-M, Lai KYA, et al. Theory and experiment of an aperture-coupled hemispherical dielectric resonator antenna. IEEE Trans Antennas Propag. 1995;43(11):1192–1198.
[184] Hosseinbeig A, Kamyab M, Meiguni JS. Theory of aperture-coupled hemispherical dielectric resonator antennas with radiating elements. AEU – Int J Electronics Commun 2013;67(11): 975–980.
[185] Kakade AB, Ghosh B. Analysis of the rectangular waveguide slot coupled multilayer hemispherical dielectric resonator antenna. IET Microwaves, Antennas Propag. 2012;6(3):338–347.
[186] Dhar S, Ghatak R, Gupta B, et al. A wideband Minkowski fractal dielectric resonator antenna. IEEE Trans Antennas Propag. 2013;61(6):2895–2903.
[187] Dhar S, Ghatak R, Gupta B, et al. Circularly polarized Minkowski fractal dielectric resonator antenna. International Symposium on Electromagnetic Theory; 2013; Hiroshima, p. 470–472.
[188] Sharma A, Biswas A. Wideband omnidirectinal perforated minkowski fractal dielectric resonator antenna. IEEE Applied Electromagnetics Conference (AEMC), 2015; Guwahati; p. 1–2.
[189] Gangwar RK, Singh SP, Kumar D. A modified fractal rectangular curve dielectric resonator antenna for WiMAX application. Prog Electromagnet Res C. 2010;12:37–51.
[190] Kiran DV, Sankaranarayanan D, Mukherjee B. Compact Minkowski Half-hexagon notched dielectric resonator antenna for wideband applications. URSI Asia-Pacific Radio Science Conference (URSI AP-RASC); 2016; Seoul; p. 1787–1790.
[191] Soren D, Ghatak R, Mishra RK, et al. Sierpinski carpet patterned rectangular dielectric resonator antenna for X-band application using Teflon. Radioelectron Commun Syst. 2018;61(12):571–578.
[192] Gupta S, Kshirsagar P, Mukherjee B. Sierpinski fractal inspired inverted pyramidal DRA for wide band applications. Electromagnetics. 2018;38(2):103–112.
[193] Pattnaik S, Sahu S, Dash SKK, et al. Rotated stacked dielectric resonator antenna with sierpinski fractal for circular polarization. International Conference on Communications and Signal Processing (ICCSP); 2015; Melmaruvathur; p. 0361–0364.

[194] Dileep S, Kiran DV, Mukherjee B. Wideband Koch snowflake fractal dielectric resonator antenna. 2015 IEEE 10th International Conference on Industrial and Information Systems (ICIIS); 2015; Peradeniya; p. 205–209.
[195] Dileep S, Kiran V, Mukherjee B. A novel compact fractal ring based cylindrical dielectric resonator antenna for ultra-wideband applications. Prog Electromagnet Res C (PIER C). 2016;67:71–83.
[196] Chauhan M, Mukherjee B. High gain fractal cylindrical dielectric resonator antenna for UWB application. IEEE Radio and Antenna Days of the Indian Ocean (RADIO); 2018; Mauritius; p. 1–2.
[197] Shaikh T, Santra G. Novel tree shaped fractal dielectric resonator antenna. 3rd International Conference on Electrical, Electronics, Engineering Trends, Communication, Optimization and Sciences (EEECOS 2016); 2016; Tadepalligudem; p. 1–4.
[198] Karmakar DP, Soren D, Ghatak R, et al. A wideband Sierpinski carpet fractal cylindrical dielectric resonator antenna for X-Band application. Applied Electromagnetics Conference (AEMC); 2009; Kolkata; p. 1–3.
[199] Mukherjee B, Patel P, Mukherjee J. Hemispherical dielectric resonator antenna based on apollonian gasket of circles—a fractal approach. IEEE Trans Antennas Propag. 2014;62(1):40–47.
[200] Sliusar I, Voloshko S, Slyusar V, et al. Synthesis of quasi-fractal hemispherical dielectric resonator antennas. International Scientific-Practical Conference Problems of Infocommunications, Science and Technology (PIC S&T); 2018; Kharkiv, Ukraine; p. 313–316.
[201] Gupta S, Tandy A, Gupta S, et al. A compact half-hemispherical DRA with two combined fractal approach. 14th IEEE India Council International Conference (INDICON); 2017; Roorkee; p. 1–6.
[202] Gupta S, Chauhan M, Mukherjee B. Fractal on hemispherical DRA by Descarte's circle theorem for wideband application. Conference on Information and Communication Technology (CICT); 2018; Jabalpur, India, p. 1–6.
[203] Hajihashemi MR, Abiri H. Parametric study of novel types of dielectric resonator antennas based on fractal geometry. Int J RF Microwave Comput-Aided Eng. 2006;17(4):416–424.
[204] Altaf A, Yang Y, Lee K, et al. Circularly polarized Spidron fractal dielectric resonator antenna. IEEE Antennas Wirel Propag Lett. 2015;14:1806–1809.
[205] Trivedi K, Pujara D. Stacked fractal tetrahedron shaped dielectric resonator antenna for UWB applications. IEEE Applied Electromagnetics Conference (AEMC); 2017; Aurangabad; p. 1–2.
[206] Ghosal R, Gupta B. Design of dual wide band dielectric resonator antenna using Sierpienski fractal geometry. 18th Mediterranean Microwave Symposium (MMS); 2018; Istanbul; p. 75–78.
[207] Liu H, Liu Y, Wei M, et al. A novel dual-broadband dielectric resonator antenna based on modified Sierpinski fractal geometry. IEEE International Symposium on Antennas and Propagation & USNC/URSI National Radio Science Meeting; 2015; Vancouver, BC; p. 43–44.
[208] Trivedi K, Pujara D. Design and development of a wideband tree shaped fractal dielectric resonator antenna. IEEE Applied Electromagnetics Conference (AEMC); 2015; Guwahati; p. 1–2.